Acousto-Electromagnetic Interaction in Materials for Aerospace Composites

NIKLAS WINGREN
MASTER´S THESIS
DEPARTMENT OF ELECTRICAL AND INFORMATION TECHNOLOGY
FACULTY OF ENGINEERING | LTH | LUND UNIVERSITY

Acousto-Electromagnetic Interaction in Materials for Aerospace Composites

Niklas Wingren
`tfy13nwi@student.lu.se`

Department of Electrical and Information Technology
Lund University

Supervisor: Daniel Sjöberg

Examiner: Mats Gustafsson

February 12, 2019

Abstract

Non-destructive testing (NDT) is a vital part of aerospace manufacturing due to high demands for quality and safety. Advances in materials science have given rise to aerospace composites with highly improved properties compared to traditional materials. To ensure that materials can be used safely, NDT techniques are continuously improved to follow advances in materials. This has also spurred development of new NDT techniques. One suggestion for improving NDT techniques is based on combining several phenomena. One such combination is acoustics and electromagnetics, such as ultrasound and mm-waves. This work explores interaction between acoustic and electromagnetic waves and attempts to connect this with possibilities for novel NDT techniques. The focus is on photoelastic interaction, meaning that an acoustic wave alters dielectric properties of a medium which in turn scatters electromagnetic waves. Existing techniques such as acousto-optics and Radio Acoustic Sounding System are used as a starting point for exploring this interaction mechanism.

Analytical models for photoelastic interaction are developed from basic electromagnetism and photoelasticity theory. Two important results are a phase matching condition for maximum scattering and a frequency shift of scattered waves, both of which are also present in acousto-optics. Numerical simulations are used to verify the phase matching condition and compare scattering power with analytical models. Defects with electric or acoustic contrast are simulated to explore NDT possibilities. Both types of contrast are shown to affect the interaction, which could be an advantage over some existing NDT techniques. However, more work is required to determine the utility for NDT.

Acknowledgments

Firstly, I would like to thank my supervisor Daniel Sjöberg for guidance and support during the thesis and for introducing me to the subject. I would also like to thank Mats Gustafsson, Torleif Martin, Christer Larsson, Jakob Helander and Johan Lundgren for valuable discussions during project meetings. Finally, I would like to thank my family and friends for their support during my studies.

Contents

List of Abbreviations

- Ac. - Acoustic
- Acousto-EM - Acousto-Electromagnetic
- EM - Electromagnetic
- HMMDI - Harmonic Motion Microwave Doppler Imaging
- IRE - Institute of Radio Engineers
- LHS - Left-Hand Side
- LNA - Low-Noise Amplifier
- NDT - Non-destructive Testing
- PEC - Perfect Electric Conductor
- PML - Perfectly Matched Layer
- RASS - Radio Acoustic Sounding System
- RF - Radio Frequency
- RHS - Right-Hand Side
- SNR - Signal-to-Noise Ratio
- SPL - Sound Pressure Level
- SIL - Sound Intensity Level
- rx - Receiver
- tx - Transmitter

List of Symbols

Electromagnetics

- $\boldsymbol{E}$ - Electric field
- $\boldsymbol{H}$ - Magnetic field
- $\boldsymbol{S}$ - Poynting vector
- μ_0 - Magnetic permeability of free space
- ε - Electric permittivity
- ε_0 - Electric permittivity of free space
- ε_r - Unperturbed relative permittivity
- ε_1 - Perturbation in relative permittivity
- η_0 - Wave impedance of free space
- η - Wave impedance in material
- c - Speed of light in material
- c_0 - Speed of light in vacuum
- $\boldsymbol{k}$ - Electromagnetic wavevector
- k - Electromagnetic wavenumber
- λ - Electromagnetic wavelength
- ω - Electromagnetic angular frequency

Acoustics

- p - Acoustic pressure
- p_p - Pressure amplitude (peak) of an acoustic wave
- v - Speed of sound in medium
- $\boldsymbol{q}$ - Acoustic wavevector
- q - Acoustic wavenumber

- Λ - Acoustic wavelength
- Ω - Acoustic angular frequency
- ρ_0 - Unperturbed density of medium
- L_p - Sound pressure level (SPL)
- L_I - Sound intensity level (SIL)
- I_s - Acoustic intensity (time-average)

Continuum mechanics

- $\boldsymbol{u}$ - Displacement vector
- λ - Lamé's first parameter
- μ - Lamé's second parameter
- ϕ - Scalar potential
- $\boldsymbol{\psi}$ - Vector potential
- c_s - Wave speed for s-waves
- c_p - Wave speed for p-waves
- σ_{ab} - ab-component of the Cauchy stress tensor (Cartesian notation: $a, b = x, y, z$)
- K - Bulk modulus

Photoelasticity

- p_{ij} - ij component of the photoelastic tensor (compact notation: $i, j = 1, \ldots, 6$)
- s_j - j component of the Cauchy strain tensor (compact notation: $j = 1, \ldots, 6$)
- $\mathfrak{p}$ - scalar photoelastic constant
- $\varepsilon_{\mathrm{r}_i}$ - i component of the relative permittivity tensor (compact notation: $i = 1, \ldots, 6$)
- $\Delta\varepsilon_{\mathrm{r}_i}$ - Perturbation in i component of the relative permittivity tensor (compact notation: $i = 1, \ldots, 6$)

Introduction

1.1 Background

The aerospace industry sets high requirements on quality and reliability, and non-destructive testing (NDT) is a crucial part of the manufacturing process [1]. The International Committee for Non-Destructive Testing states that "Non-destructive testing is the branch of engineering concerned with all methods of detecting and evaluating flaws in materials" and that "The essential feature of NDT is that the test process itself produces no deleterious effects on the material or structure under test" [2]. In aircraft construction, NDT allows for inspection of the structural integrity of parts both in manufacturing and during service [1, 3].

Aircraft construction has traditionally relied heavily on aluminum alloys, but these have increasingly been replaced by composite materials [1]. The advantages of using composites are many, such as higher strength, lighter weight and resistance to corrosion to mention a few [1]. However, the possible modes of failure are different in composites than for aluminum alloys which puts other demands on NDT [1, 4]. To be able to keep reliability high, many NDT techniques have been developed for composites [4, 5]. Ultrasonic testing is one of the most established methods used for aerospace composites [3, 4], and has been used in many other fields as well [6]. Most techniques in ultrasonic testing require coupling between the transducer and sample using for example water [6]. However, in some cases the ultrasonic wave can be coupled through air, giving a contactless method [7].

One NDT technique which has become more popular relatively recently is microwave and mm-wave imaging [8, 9]. Better microwave electronics due to advances in semiconductor devices has made this field increasingly attractive [9]. One of the main benefits of mm-wave imaging is its high resolution [8, 10]. In the field of aerospace NDT, mm-wave imaging is interesting due to its ability to detect flaws in low loss dielectric composites [10], and particularly in honeycomb composites [11].

In medical imaging, the combination of multiple techniques has been proposed as a way of improving performance. One example is multimodality imaging, where two techniques are used to produce images separately to be combined in post-processing [12]. However, if two wave phenomena are utilized simultaneously a single image can be produced with combined benefits of the two [12]. There is a large overlap between NDT and medical imaging, and similar techniques are often

used in both fields [13, 14, 15]. Due to their existing usage and potential, a combination of ultrasonic testing with modern mm-wave imaging could be of interest in NDT for aerospace composites. The combination of acoustic and electromagnetic waves has been proposed for NDT before [16, 17], but no signs of practical use could be found by the author.

Interaction between acoustic and electromagnetic phenomena has been known since at least the earlier half of the 20th century in the form of acousto-optics [18]. This type of interaction has been used practically in photonic devices since the 1960s and is well-understood [18].Typical acoustic waves are then ultrasound in the MHz frequency range, and electromagnetic waves are at optical frequencies [18]. Interaction at completely different frequency ranges is used in meteorology under the name Radio Acoustic Sounding System (RASS) [19, 20, 21]. The electromagnetic waves are in this case radio waves in the MHz-GHz range, while acoustic waves are audible sound [20]. The original purpose of this system was to measure atmospheric temperatures [19], but it has also been used to measure other parameters such as wind phenomena [21]. Other mechanisms for interaction between acoustic and electromagnetic waves exist with possible applications such as land mine detection [22], breast tumor detection [23] and optical sensing in medicine [24].

1.2   Related Work

A mm-wave imaging system was developed and tested on composite panels at the Department of Electrical and Information Technology, Lund University [10]. While not directly connected, the current work is inspired by the mm-wave imaging work made at the department. Additionally, the simulations and experiments described in the paper were highly useful for understanding properties of a mm-wave NDT system and relevant test materials. For an overview of microwave and mm-wave imaging for use in NDT, [8] and [9] introduce techniques and applications while not delving too deep into specifics.

For the well established technique of ultrasonic testing, the book by Schmerr [6] is a good reference and introduction to the general topic. More specifically, modern aerospace NDT is described in [3, 4] and [7]. These papers compare various NDT techniques, of which ultrasonic testing is one.

For acousto-optics, the dedicated chapter in [25] provides a good overview of the topic. For more detailed study, the monography by Korpel [26] covers much of the topic in great detail and with different approaches.

A type of acousto-electromagnetic phenomena where the wavelengths involved are on the same order of magnitude is described in the RASS literature. Early work in [27] contains electromagnetic derivations related to the problem. Good descriptions of functional RASS systems can be found in [19] and [20], although they do not present much theoretical background. A good reference deriving basic theory for RASS performance is [28], which describes the problem with a beginning in basic electromagnetic scattering. An earlier work related to this is the book by Tatarskii [29] which is focused on turbulence and wave propagation. Much of the theory it presents regarding the effect of turbulence on electromagnetic waves is

easily transferable to the acousto-electromagnetic problem, and chapter 2 of the book was heavily used for parts of this work.

Another acousto-electromagnetic interaction mechanism is based on acoustically exciting radar targets. This was investigated as a way of detecting land mines by Scott and Martin [22]. More mathematical modeling of this problem was performed by Buerkle, Sarabandi and Lawrence in [30, 31] and [16] where the last one relates the mechanism to NDT. The thesis by Buerkle [15] provides a good summary of this interaction mechanism, possible applications and techniques.

Vibrations can also be caused inside an object through acoustic radiation pressure. This has been used in multiple medical imaging methods described in [32]. One well-known method using ultrasound to cause vibrations in tissue is vibro-acoustography, which was introduced by Fatemi and Greenleaf [13]. A method combining acoustic radiation pressure and microwave imaging, Harmonic Motion Microwave Doppler Imaging (HMMDI), was proposed by Top and Gençer as a way of to improve breast tumor detection [33]. The method was tested successfully on imaging phantoms (artificial model of human tissue) in [23] and [34].

1.3   Purpose and Goals

Three goals were set up before starting the work in the form of questions to be answered by the thesis:

1. How does acousto-electromagnetic interaction differ from acousto-optic theory with wavelengths in the same order of magnitude?

2. What properties do acoustic and electromagnetic waves have in homogeneous materials and laminated composites?

3. How can ultrasound improve mm-wave imaging of defects in composites?

The goals were not written in a very specific way due to them being decided before a thorough review of the literature. However, during the literature review process more information was obtained and the goals were appended with more specific questions and sub-goals.

1.4   Outline

There are 7 chapters and an appendix in this thesis. This chapter serves as a background to the subject and purpose of the thesis. Chapter 2 gives a background on some pieces of technology with relation to the subject. Chapter 3 describes the theory required for the rest of the thesis. Chapter 4 presents an analytical model based on the theory from chapter 3. Chapter 5 describes numerical simulations used in part to verify models from chapter 4. Chapter 6 presents results from chapters 4 and 5, discusses these and conclusions are drawn. Chapter 7 presents some possible ways of continuing this work. Appendix A presents full derivations for the models in 4.

Technology

This chapter introduces some pieces of technology which are of interest for understanding the topic and further chapters.

2.1 Aerospace Composites

Composites are manufactured materials composed of multiple distinct material components. Together, the composite material obtains characteristics not present in the individual components [35]. In aerospace, composites have been used in military aircraft for a long time but more recently commercial aircraft have also seen large-scale adoption of composites [1]. The advantages of using composites over traditional aluminum alloys are many, which is the reason for their increased adoption. The composite materials used in aerospace are often made out of the two major components fibers and matrix [1]. The fibers, or reinforcement, provide high strength and stiffness while the matrix is used to bind the fibers together [1]. A common type of composite is the polymer-matrix composite, which uses a polymer material matrix reinforced by glass- or carbon-fiber [35, 1].

Structures are often constructed by layering composites on top of each other as laminates [1]. The individual layers, or lamina, can be made of different types of composites with fibers oriented in different directions for optimal strength and stiffness [1]. An important type of laminated composite is the sandwich composite, which is composed of a lightweight panel of core material with thin sheets of stiffer material bonded to the two faces of the core [36]. This type of construction allows for a very lightweight, but still strong composite laminate which is of great interest to the aerospace industry where weight is critical [36, 1]. The sheet material is often fiber-reinforced polymer-matrix composites while cores are often constructed with a cellular structure, meaning that it contains cells of open space [36, 11]. This cellular structure is commonly achieved by using foams or honeycomb structures [36].

2.2 Acousto-EM in Established Technology

Mechanisms for interaction between acoustics and electromagnetism have been known for a long time, primarily through acousto-optics [18]. Beyond knowledge

of the phenomena there are also applications in technology which are investigated in this section. Two examples are given: acousto-optics and the Radio Acoustic Sounding System. These operate at very different frequencies (both acoustic and electromagnetic) which can be of interest when investigating the possibility of using mm-wave frequencies.

2.2.1 Acousto-Optics

Acousto-optics is a phenomenon based on the refractive index varying due to an acoustic wave [25]. If a beam of light is incident on an acoustic beam in a material, it will be diffracted by this periodic change in refractive index. There are multiple types of acousto-optic diffraction, but one of the more common types is Bragg diffraction which occurs for thick acoustic beams [26]. One characteristic of this phenomenon is that phase matching is required for strong diffraction, and this is described by the so called Bragg condition

$$\sin \theta_{\mathrm{B}} = \frac{\lambda}{2\Lambda}$$

where θ_{B} is the optical angle of incidence with reference to the acoustic beam, λ is the optical wavelength and Λ is the acoustic wavelength [25]. The angle of diffraction is also θ_{B} [25]. Acousto-optics was first investigated in the early 20th century [18], and today it is used in many photonic devices [25]. Examples of applications for acousto-optics are modulators, scanners and filters [25]. Acousto-optic modulators use the Bragg condition to amplitude-modulate light by varying the acoustic frequency [25]. Scanners also vary the acoustic frequency, but are used to change the direction θ_{B} of the diffracted beam of light [25]. Acousto-optic filters use a constant acoustic frequency, and a wide spectrum of light can be filtered by selecting a specific angle θ_{B} [25].

2.2.2 Radio Acoustic Sounding System

One application of acousto-electromagnetic interaction can be found in meteorology through the Radio Acoustic Sounding System (RASS). The purpose of the system is to utilize the interaction between radio and acoustic waves for temperature sounding of the atmosphere [20]. The Bragg condition in acousto-optics also holds here, and is in fact the main mechanism allowing for the measurement of temperature. As explained in the introduction of the thesis, the frequencies used in RASS are highly different from those used in acousto-optics. The ratio between them is also different as the two waves are parallel and their sources co-located in RASS [19]. This reduces the Bragg condition to [19]

$$\Lambda = \frac{\lambda}{2}$$

A fulfilled Bragg condition then leads to the electromagnetic wave being backscattered. The mechanism allowing for temperature measurement is that the acoustic wavelength depends on temperature, which affects the Bragg condition [19]. For given acoustic and electromagnetic frequencies, the Bragg condition therefore only

holds at a specific temperature. There are multiple ways of measuring the temperature at certain heights using this fact, using different types of acoustic excitation [20]. For example, one method is based on modulating the acoustic frequency continuously, giving different acoustic frequency at different heights. A pulsed radar system is then used to detect the altitude at where the Bragg condition is fulfilled, and since the acoustic frequency is known at every altitude the speed of sound can be determined [20].

Theory

This chapter presents some of the theory required to analytically derive a model for acousto-electromagnetic interaction. Some different interaction mechanisms between the two phenomena are presented in the beginning, but the rest of the theory is mostly related to the mechanism actually used in the analytical model.

3.1 Overview of Interaction Mechanisms

To introduce the subject, four types of interaction mechanisms between acoustic and electromagnetic waves are presented. This is by no means a complete list of possible ways of combining the phenomena. Instead, these mechanisms are those which could be found in the literature relatively easily.

3.1.1 Target Boundary Perturbation

This mechanism is based on a discrete target under acoustic resonance. The resonance of the target leads to vibration, which is seen as a time-dependent boundary perturbation [15]. An electromagnetic wave scattered against this vibrating target resembles a frequency modulated signal, where the strongest frequency components being those of the original frequency shifted by the acoustic resonance frequency [31, 37]. This is seen as a Doppler shift, which could be used for some types of NDT [16]. One issue with this mechanism is that it is based on a target being under acoustic resonance. This might be interesting in some cases, but for complex objects it could be time-consuming to find resonances which is not ideal for a production environment. The mechanism is also not very similar to ultrasonic testing, so while the interaction is based on acoustic and electromagnetic waves it is not a reasonable combination of ultrasonic testing and mm-wave imaging.

3.1.2 Localized Harmonic Motion

Interaction based on Localized Harmonic Motion is similar to the previous one based on boundary perturbation in that it uses scattering from harmonic motion. The difference is that harmonic motion is introduced in a bulk material instead of a resonating discrete target. The acoustic part of the mechanism has been utilized in various medical methods such as vibro-acoustography and harmonic

motion imaging [32]. Both techniques use amplitude modulated ultrasound to produce a time-harmonic force acting on a localized region of a sample. This generates time-harmonic displacement, or vibration. In the acoustic methods the vibrating region emits elastic waves which can be detected [13, 38]. A method using the combination of acoustics and electromagnetics is Harmonic Motion Microwave Doppler Imaging (HMMDI) which was introduced as a method for detecting breast tumors [33]. Advantages over other single-phenomenon imaging methods would be that the interaction gives the method ability to detect contrast in both dielectric and elastic properties [23].

An electromagnetic wave incident towards the vibrating region will scatter with a frequency shift which corresponds to the frequency of vibration [33]. This is very similar to the boundary perturbation mechanism described before. The frequency shifted signal is in reality the first harmonic of a phase modulated signal due to the micro-Doppler effect [15]. Weaker harmonics can often be ignored, leaving only the original frequency component and those shifted up or down by the vibration frequency [23]. The micro-Doppler effect mentioned is an addition to the regular Doppler effect which comes into play when a target undergoes micro-motion [39]. The regular Doppler effect prescribes a constant frequency shift for a target in constant motion, while the micro-motion required for the micro-Doppler effect can be vibrations or rotations of a target [39].

The localized harmonic motion mechanism is fundamentally based on generating a force locally using amplitude modulated ultrasound. This is possible due to the effect of acoustic radiation force, or acoustic radiation pressure, which is an effect of nonlinear acoustics [33, 32]. A plane wave model for the acoustic radiation force gives a linear relationship between the force in the propagation direction of the wave and acoustic intensity [32, 40]. To explain the fundamentals of acoustic radiation force many different models have been developed [41, 42], but due to their complexity they are not presented here. Nevertheless, the simple linear model is used successfully in medical applications of acoustic radiation force [13, 43, 38, 34].

Two methods of generating radiation force locally are described in the literature. The first method uses amplitude modulated focused ultrasound with its focus on the region of interest [23]. Since amplitude modulated ultrasound exists throughout the beam a force is generated in that entire region. However, the intensity is much higher in the focus so the force is stronger there. The second method instead uses two single-frequency ultrasonic beams which intersect at the region of interest. The frequencies of the two beams differ by a small amount $\Delta\Omega$ [13]. The acoustic pressure at the intersection is given by the superposition of the two beams, and amplitude modulation by $\Delta\Omega$ is obtained in the acoustic intensity [13]. For a linear model between intensity and acoustic radiation force, the resulting force varies with the frequency $\Delta\Omega$ [33].

The foundations for this mechanism have been explored primarily in medical imaging but as described in the introduction of this thesis, medical imaging and NDT share many techniques and this might be the case for this technology as well. The possible advantages in contrast presented for HMMDI are valid for NDT as well as for medical applications, so this interaction mechanism should be interesting to investigate for NDT.

3.1.3   Acousto-Optics

Acousto-optics is an interaction mechanism often explained using simple elasticity models and wave optics [25, 18]. The main idea is that there is a relation between the strain in a material and its index of refraction. Since an acoustic wave consists of periodic compression and rarefaction in a medium (which can be related to strain), a consequence is that the index of refraction varies with the same period [25]. This periodic structure of varying index of refraction acts as a Bragg reflector scattering incident light [25]. The Bragg condition determines the angle of incidence θ_B required for the light

$$\sin \theta_B = \frac{\lambda}{2\Lambda}$$

where λ is the light wavelength and Λ is the acoustic wavelength [25]. As for the previously mentioned mechanisms, the scattered wave is frequency shifted by the acoustic frequency [26].

There is nothing in the basic theory suggesting that optical frequencies are required for this interaction. At microwave frequencies permittivity is more common to use than index of refraction, but they are related and the principle is the same. An application which uses this principle and has been used for many years is the radio acoustic sounding system [15]. Additionally, though not using the exact Bragg formulation for modeling interaction, some authors have explored other ways of using similar interaction at microwave frequencies [30, 17]. It has been stated, however, that this interaction is very small and resonance is often required (giving rise to boundary perturbation) [15].

It is common to assume near-perpendicularity between the acoustic and electromagnetic wavevectors in acousto-optic theory [26]. For modeling at other angles, which makes for other wavelength ratios through the Bragg conditions, this interaction mechanism is studied further. A full electromagnetic model based on Maxwell's equations is presented in section 4.1.

3.1.4   Scatterer Displacement

This is a mechanism mostly presented in the field of ultrasound-optical tomography. The mechanism is based on dynamic multiple scattering of light, which occurs if many scatterers undergoing Brownian motion are considered [44]. If an ultrasonic beam is incident on such a sample the scatterers will move due to both Brownian motion and ultrasound, giving rise to a frequency shift in affected photons [44, 24]. In medical applications, movement of the scatterers due to acoustic waves is very straight-forward: their displacement directly follows the acoustic wave [44]. For small scatterers in fluids such as blood (which is considered in much of the literature), this movement might occur easily. However, larger scatterers in solids would require more energy to be moved in this way and this might limit relevance for NDT.

For this work, a mechanism needs to be relevant at microwave frequencies to be considered. The assumption on which the theory rests is that of dynamic multiple light scattering [44]. In the existing mm-wave imaging system there is an assumption of sparse defects being the only scatterers [10]. This is in complete

contrast to the theory of dynamic multiple light scattering, which is based on a large number of moving scatterers [44]. Since the basic assumptions of the problem and theory are in such stark contrast, it seems likely that this interaction mechanism holds little relevance to the problem at hand.

3.1.5   Main Subjects of Interest

The mechanisms presented above were the major ones found in a wide search of the literature. Of the four presented, two could be ruled out for not being applicable to the problem of interest. The localized harmonic motion and acousto-optics interaction mechanisms were considered to be relevant to the NDT problem. However, due to time constraints the acousto-optics mechanism was given the main focus. Therefore, the rest of this work is mostly dedicated to this interaction mechanism.

3.2   Ultrasonic Wave Propagation

The fundamental problem in this work is to combine acoustic and electromagnetic waves. In particular, ultrasound and micro/mm-waves are of interest and therefore ultrasonic wave propagation is presented here. In many NDT applications the ultrasonic waves are generated in some transducer, coupled into a fluid medium and then coupled further into the solid medium of the test object [6]. This requires knowledge of wave propagation in both fluid and solid media. The word acoustics is sometimes used in the literature for propagation in both types of media, and sometimes only for fluid media. When distinction between waves in the two media is required in this work, "acoustic waves" is used for fluids and "elastic waves" for solids.

3.2.1   Propagation in a Fluid Medium

In a compressible fluid ultrasound can be described by a standard acoustic model. The main variable for describing the wave motion is pressure in this case. In turn, this can be converted into other variables such as displacement or strain. The theory of acoustics originates in continuum mechanics, but a restriction to fluids and a linearization leads to the most commonly used model - linear acoustics [45]. The acoustic wave equation which lies at the heart of the model of linear acoustics can be written as [45, 6, 46]

$$\nabla^2 p - \frac{1}{v^2}\frac{\partial^2 p}{\partial t^2} = 0 \tag{3.1}$$

where p is pressure and v is the speed of sound in the fluid. In addition to linearization, this equation assumes no body forces and a homogeneous density of the medium [45]. The speed of sound can be written as $v = \sqrt{K/\rho_0}$ where K is the bulk modulus of the fluid and ρ_0 is the unperturbed density of the fluid [46].

This model is directly useful for NDT in some cases. One is in immersion testing, where a test object is immersed in water and ultrasound propagates through

the water into the object [6]. The other is in coupling ultrasound from a transducer to an object through a thin layer of coupling fluid [6]. However, this model is also useful for understanding one special case of propagation in an elastic solid, namely p-wave propagation [45]. This will be described further in the next part.

While the pressure is the main quantity describing acoustic waves in a fluid, one of the more common quantities is instead sound pressure level (SPL). This is a relative quantity measured in dB, which is defined as

$$L_\mathrm{p} = 20 \log_{10} \frac{p}{p_\mathrm{ref}}$$

where p_ref is a reference pressure which is defined as 20 μPa in air [45]. Another quantity, which was introduced earlier when discussing acoustic radiation force is acoustic intensity. This is defined as the acoustic power per unit area [45]. An instantaneous value for this is

$$\boldsymbol{I}(t) = p(t)\boldsymbol{v}_\mathrm{part}(t)$$

where $\boldsymbol{v}_\mathrm{part}(t)$ is the particle velocity [45]. However, it is more common to use the time-average value [47]. For plane waves, a relation for this can be written as

$$I_\mathrm{s} = \frac{p_\mathrm{p}^2}{2\rho_0 v}$$

where p_p is the peak pressure amplitude of the plane wave, ρ_0 is the density and v the acoustic wave speed [45]. One thing to note is that this is a scalar, and not a vector as before. The direction in this case is understood to be the same as the propagation direction of the plane wave [45]. Related to acoustic intensity is the sound intensity level (SIL), which is analogous to SPL. This is measured in dB and defined as

$$L_\mathrm{I} = 10 \log_{10} \frac{I_\mathrm{s}}{I_\mathrm{s,ref}}$$

where $I_\mathrm{s,ref}$ is a reference intensity which is defined as 10^{-12} W/m^2 in air [45].

3.2.2   Propagation in a Solid Medium

In an elastic medium the acoustic model is no longer sufficient. That model only considers pressure since one main assumption for volume elements in the fluid is that they only transmit force in the direction of the force [46]. The volume elements in an elastic solid are more strongly coupled to each other, and this assumption does not hold anymore [48]. The equations of elastic waves are instead based on solid mechanics. There is no simple wave equation as in acoustics, instead the model is described by Navier's equations

$$\mu\nabla^2\boldsymbol{u} + (\lambda+\mu)\nabla(\nabla\cdot\boldsymbol{u}) + \boldsymbol{f} = \rho_0 \frac{\partial^2\boldsymbol{u}}{\partial t^2}$$

where $\boldsymbol{u}$ is the displacement vector, λ and μ are the Lamé parameters of the material and $\boldsymbol{f}$ is the body force [6]. To obtain wave equations from this, a Helmholtz decomposition is made as

$$\boldsymbol{u} = \nabla\phi + \nabla\times\boldsymbol{\psi}$$

where ϕ is a scalar potential and $\boldsymbol{\psi}$ is a vector potential [6]. For Navier's equations to be fulfilled, the following must hold for the potentials [6]:

$$\nabla^2 \phi - \frac{1}{c_{\mathrm{p}}^2} \frac{\partial^2 \phi}{\partial t^2} = 0$$

$$\nabla^2 \boldsymbol{\psi} - \frac{1}{c_{\mathrm{s}}^2} \frac{\partial^2 \boldsymbol{\psi}}{\partial t^2} = 0$$

These are two wave equations with the wave speeds [6]

$$c_{\mathrm{p}} = \sqrt{(\lambda + 2\mu)/\rho_0}$$

$$c_{\mathrm{s}} = \sqrt{\mu/\rho_0}$$

By further investigation, the waves can be identified as p-waves with speed c_{p} and s-waves with speed c_{s} [6]. The p-waves are very similar to acoustic waves in fluids, and it can be shown that the dilatation of the solid (the sum of linear strains, $\nabla \cdot \boldsymbol{u}$) travels at c_{p} [6]. The s-waves on the other hand, do not have an analogy in acoustics. The local rotation of the solid (half the curl of the displacement vector, $(\nabla \times \boldsymbol{u})/2$) follows the s-wave equation [6]. This local rotation is always zero in acoustics due to the weak coupling between volume elements [46], so s-waves cannot propagate in fluids. When it comes to actually generating ultrasonic elastic waves, transducers are available both for generation of p-waves and s-waves [6].

One important detail when working with solid materials capable of supporting both p- and s-waves is that conversion between the two is possible [6]. Mode conversion is a phenomena where even pure p-waves will generate a combination of p- and s-waves. Whenever a p-wave is incident at an interface at oblique angles, mode conversion will take place [6].

The elastic waves described above are called bulk waves since they only fully describe waves in the bulk of an elastic solid [48]. Other wave phenomena exist such as surface waves (Rayleigh, Stoneley, Love) [48] and plate waves (SH, Lamb) [6]. These waves are not insignificant and are used in some branches of ultrasonic testing [6]. However, only bulk waves are considered here.

To be able to easily relate elastic p-waves to acoustic waves in fluids, a relation between pressure and dilatation is required. In a fluid at rest, the pressure can be related to the linear stresses in the Cauchy stress tensor as [49]

$$\begin{pmatrix} \sigma_{xx} & \sigma_{xy} & \sigma_{xz} \\ \sigma_{yx} & \sigma_{yy} & \sigma_{yz} \\ \sigma_{zx} & \sigma_{zy} & \sigma_{zz} \end{pmatrix} = \begin{pmatrix} -p & 0 & 0 \\ 0 & -p & 0 \\ 0 & 0 & -p \end{pmatrix}$$

where σ_{ab} are stress components written in Cartesian coordinates. All linear stresses are equal for that case, which does not hold in general. However, the pressure can still be related to the Cauchy stress tensor for cases where linear stresses are not equal (and even in solids) by [50]

$$p = -\frac{1}{3}(\sigma_{xx} + \sigma_{yy} + \sigma_{zz})$$

which is just the negative of the mean value of the linear stresses. For an isotropic solid, these can be written using Lamé parameters and displacements as [6]

$$\sigma_{xx} = \lambda \nabla \cdot \boldsymbol{u} + 2\mu \frac{\partial u_x}{\partial x}$$

$$\sigma_{yy} = \lambda \nabla \cdot \boldsymbol{u} + 2\mu \frac{\partial u_y}{\partial y}$$

$$\sigma_{zz} = \lambda \nabla \cdot \boldsymbol{u} + 2\mu \frac{\partial u_z}{\partial z}$$

The pressure can then be written as

$$p = -\frac{1}{3} \left(\lambda \nabla \cdot \boldsymbol{u} + 2\mu \frac{\partial u_x}{\partial x} + \lambda \nabla \cdot \boldsymbol{u} + 2\mu \frac{\partial u_y}{\partial y} + \lambda \nabla \cdot \boldsymbol{u} + 2\mu \frac{\partial u_z}{\partial z} \right)$$

$$= -\left(\lambda \nabla \cdot \boldsymbol{u} + \frac{2\mu}{3} \left(\frac{\partial u_x}{\partial x} + \frac{\partial u_y}{\partial y} + \frac{\partial u_z}{\partial z} \right) \right) = -\left(\lambda + \frac{2\mu}{3} \right) \nabla \cdot \boldsymbol{u}$$

The Lamé parameters are related to the bulk modulus by $K = \lambda + 2\mu/3$ [49] which simplifies the equation above to

$$p = -K \nabla \cdot \boldsymbol{u} \tag{3.2}$$

With this it is straight-forward to calculate the pressure for a given displacement. The dilatation follows the wave equation with the p-wave speed [6]

$$\nabla^2 (\nabla \cdot \boldsymbol{u}) - \frac{1}{c_{\mathrm{p}}^2} \frac{\partial^2 (\nabla \cdot \boldsymbol{u})}{\partial t^2} = 0$$

If equation (3.2) is inserted, and the wave equation is multiplied by $-K$, the result is

$$\nabla^2 p - \frac{1}{c_{\mathrm{p}}^2} \frac{\partial^2 p}{\partial t^2} = 0$$

This is the same as the acoustic wave equation in fluids (3.1), with the exception of the wave speeds which are $v = \sqrt{K/\rho_0} = \sqrt{(\lambda + 2\mu/3)/\rho_0}$ for acoustic waves and $c_{\mathrm{p}} = \sqrt{(\lambda + 2\mu)/\rho_0}$ for p-waves. Written using bulk modulus and shear modulus (μ is equal to the shear modulus [50]) this is then $c_{\mathrm{p}} = \sqrt{(K + 4\mu/3)/\rho_0}$

3.3 Photoelasticity

To understand how the basic interaction from acousto-optics works, the first step is to understand how an elastic wave affects electromagnetic properties. The theory of photoelasticity relates strains from linear elasticity with the relative permittivity of a material. With a starting point in solid mechanics, a tensor-based theory is somewhat inevitable. However, a simplified model is shown later which condenses the tensor relations down to a scalar relation. Since the interaction between elastic and electromagnetic waves in this case is based on photoelasticity, it will be called "photoelastic interaction" further on in the text instead of "acousto-optics" even

though the underlying physics are the same. The reason for this is that "acousto-optics" is a misnomer for non-optical frequencies.

A starting point can be found in the literature on acousto-optics in the relation [26]

$$\Delta\left(\frac{1}{n_i^2}\right) = p_{ij}s_j$$

where s_j are strains and $i, j = 1, \ldots, 6$. The double indexation of j in both p and e indicates a summation over j. The notation $\Delta\alpha$ indicates the difference between a perturbed quantity α and its unperturbed value. Since refractive index and relative permittivity are related by $\varepsilon_{r_i} = n_i^2$ in a non-magnetic material, the relation is rewritten as

$$\Delta\left(\frac{1}{\varepsilon_{r_i}}\right) = p_{ij}s_j$$

The LHS is the difference of an inverse quantity, which is cumbersome to use. To find $\Delta\varepsilon_{r_i}$ instead of $\Delta(1/\varepsilon_{r_i})$ it is assumed that the difference $\Delta\varepsilon_{r_i}$ is small when compared with the non-perturbed value ε_{r_i}. With that assumption, the difference $\Delta\varepsilon_{r_i}$ is approximated as a differential. This allows use of the chain rule as

$$\Delta\varepsilon_{r_i} \approx d\varepsilon_{r_i} = \frac{d\varepsilon_{r_i}}{d\alpha}d\alpha \approx \frac{d\varepsilon_{r_i}}{d\alpha}\Delta\alpha$$

where α is some variable with a small difference $\Delta\alpha \approx d\alpha$. If α is selected as $\alpha = 1/\varepsilon_{r_i}$ this leads to

$$\Delta\varepsilon_{r_i} \approx \frac{d\varepsilon_{r_i}}{d\alpha}\Delta\alpha = -1/\alpha\Delta\alpha = -\varepsilon_{r_i}^2 p_{ij}s_j$$

The tensor notation used above is a simplified form described by the 1949 IRE standards. The relation to full tensor notation is shown below for an arbitrary tensor a [26]

$$a_1 = a_{11}, \ a_2 = a_{22}, \ a_3 = a_{33},$$
$$a_4 = a_{23}, \ a_5 = a_{31}, \ a_6 = a_{12}$$

If the strains are considered, it is clear that indices 1-3 are tensile and 4-6 are shear. For the photoelastic tensor it can be seen that it is of rank 4, being p_{ijkl} in standard notation. One thing to note is that the 4 indices in standard notation should allow for many more components of the photoelastic tensor than those possible using this compact notation (81 instead of 36). This is due to symmetry of the photoelastic tensor in this particular model [25]. It should also be noted that this model does break down in some cases, and more advanced descriptions of the phenomena exist [51]. However, this model was considered advanced enough as a starting point for this problem, especially since it is quite heavily simplified in the end.

This model of the photoelastic tensor allows for up to 36 independent components, but for the simple case of an isotropic solid the tensor simplifies to [26]

$$p_{11} = p_{22} = p_{33}, \ p_{12} = p_{21} = p_{13} = p_{23} = p_{32}$$
$$p_{44} = p_{55} = p_{66} = \frac{1}{2}(p_{11} - p_{12}), \ p_{ij} = 0 \text{ for others}$$

The simplest material to consider would be an isotropic solid with isotropic permittivity ε_r. There is then no preferred axis and a coordinate system can be selected arbitrarily. A longitudinal elastic wave is defined using strain as

$$s_1(x_1, t) = s_\mathrm{p} \cos(\Omega t - q x_1)$$

It is propagating in the x_1 direction and is thus a strain s_1, and all other strains are assumed to be zero. The relation $\Delta \varepsilon_{\mathrm{r}_i} = -\varepsilon_{\mathrm{r}_i}^2 p_{ij} s_j$ together with the photoelastic tensor for isotropic solids then gives

$$\Delta \varepsilon_{\mathrm{r}_1} = -\varepsilon_\mathrm{r}^2 p_{11} s_\mathrm{p} \cos(\Omega t - q x_1)$$
$$\Delta \varepsilon_{\mathrm{r}_2} = \Delta \varepsilon_{\mathrm{r}_3} = -\varepsilon_\mathrm{r}^2 p_{12} s_\mathrm{p} \cos(\Omega t - q x_1)$$

It is clear that the permittivity now has an axis x_1 where it has another value than in x_2 and x_3. So even for a material which is nominally completely isotropic, a preferred axis arises for the permittivity! This type of anisotropy causes birefringence in optics, and in this case it is caused by dipoles aligning themselves parallel to the strain [26]. Practically, the effect of this is that the interaction strength of this mechanism depends on the EM polarization with respect to the elastic wave polarization. In longitudinal elastic waves the polarization and propagation direction coincide, which makes analysis easier.

For a very simplistic model, the anisotropy can be ignored if it is assumed that $p_{11} = p_{12}$. This assumption reduces the photoelastic tensor to

$$p_{11} = p_{22} = p_{33} = p_{12} = p_{21} = p_{13} = p_{23} = p_{32} = \mathfrak{p}$$
$$p_{ij} = 0 \text{ for others}$$

where $\mathfrak{p}$ was introduced as a scalar photoelastic constant. One thing to note is that since $p_{33} = p_{44} = p_{55} = 0$, shear strain does not have any effect in this simplified model. If the unperturbed permittivity is isotropic ($\varepsilon_{\mathrm{r}_1} = \varepsilon_{\mathrm{r}_2} = \varepsilon_{\mathrm{r}_3} = \varepsilon_r$, $\varepsilon_{\mathrm{r}_i} = 0$ for $i = 4, 5, 6$) a scalar relation can be written as

$$\varepsilon_1 = -\varepsilon_\mathrm{r}^2 \mathfrak{p}(s_1 + s_2 + s_3)$$

Here ε_1 was introduced as the isotropic change in relative permittivity, $\varepsilon_1 = \Delta \varepsilon_{\mathrm{r}_1} = \Delta \varepsilon_{\mathrm{r}_2} = \Delta \varepsilon_{\mathrm{r}_3}$. At this stage it is more practical to use Cartesian coordinates than index notation since much other theory uses that convention. Vector notation is also used when appropriate. Using this convention, it follows that

$$\varepsilon_1 = -\varepsilon_\mathrm{r}^2 \mathfrak{p}(s_{xx} + s_{yy} + s_{zz}) = -\varepsilon_\mathrm{r}^2 \mathfrak{p} \left(\frac{\partial u_x}{\partial x} + \frac{\partial u_y}{\partial y} + \frac{\partial u_z}{\partial z} \right) \tag{3.3}$$
$$= -\varepsilon_\mathrm{r}^2 \mathfrak{p}(\nabla \cdot \boldsymbol{u})$$

Using equation (3.2) this relation can now be expressed using pressure

$$\varepsilon_1 = \frac{\varepsilon_\mathrm{r}^2 \mathfrak{p}}{K} p \tag{3.4}$$

Scalar models such as this might seem unreasonably simplified when the starting point is a much more complicated tensor relationship. However, in acousto-optics

scalar relations similar to this are used [25, 26], and in many cases the only quantity used might be a scalar figure of merit for the interaction strength [26].

To obtain a model for calculating the scalar constant $\mathfrak{p}$, another starting point for the problem is utilized. This is the Lorentz-Lorenz relation, which can be used to obtain the following equations for photoelasticity [26]

$$\Delta n = C' S$$

$$C' = \left[\frac{(n^2 - 1)(n^2 + 2)}{6n} \right] (1 - \Lambda_0)$$

$$\Lambda_0 = -\left(\frac{\rho}{\alpha} \right) \frac{\mathrm{d}\alpha}{\mathrm{d}\rho}$$

where S is the condensation (relative change in density), ρ is the density and α is the molecular polarizability. Here the anisotropic effects are contained in the parameter Λ_0 [26]. If anisotropy should be considered, the tensor model is probably better to use, but if Λ_0 is neglected a simplified model is obtained. This type of model is usually accurate for liquids, but many solids do not have this behavior [26]. Nevertheless, the simplified relation can be written for permittivity (using $\varepsilon_\mathrm{r} = n^2$ and $\varepsilon_1 = 2n\Delta n$) as

$$\varepsilon_1 = \frac{1}{3}(\varepsilon_\mathrm{r} - 1)(\varepsilon_\mathrm{r} + 2)S$$

In a fluid model, the condensation can be related to dilatation using the relation $-\rho_\mathrm{a}/\rho_0 = \nabla \cdot \boldsymbol{u}$ where ρ_a is the change in density [46]. Since the condensation can be written as $S = \rho_\mathrm{a}/\rho_0$ [26] the relation is rewritten as

$$\varepsilon_1 = -\frac{1}{3}(\varepsilon_\mathrm{r} - 1)(\varepsilon_\mathrm{r} + 2)(\nabla \cdot \boldsymbol{u})$$

This can be compared with equation (3.3) to obtain an equivalent photoelasticity

$$\mathfrak{p} = \frac{(\varepsilon_\mathrm{r} - 1)(\varepsilon_\mathrm{r} + 2)}{3\varepsilon_\mathrm{r}^2} \tag{3.5}$$

A plot of $\mathfrak{p}$ as a function of ε_r is shown in figure 3.1. It can be seen clearly that the interaction strength increases with ε_r close to 1. However, at around $\varepsilon_\mathrm{r} = 4$ an extreme is reached, and further on $\mathfrak{p}$ levels out. Thus, there is a bound on the interaction strength for this relation. It should be noted that this model is extremely simplistic and is probably only accurate for a limited range of materials.

This simple model can be compared with a model for dry air found in the RASS literature. The perturbation in relative permittivity can then be related to pressure as [52]

$$\varepsilon_1 = \frac{1.13 \cdot 10^{-6} p}{T}$$

where p is the pressure in Pa and T is the temperature in K (which would give the constant a unit of K/Pa). The equations (3.4) and (3.5) can be combined to give the simple model

$$\varepsilon_1 = \frac{\varepsilon_\mathrm{r}^2 \mathfrak{p}}{K} p = \frac{(\varepsilon_\mathrm{r} - 1)(\varepsilon_\mathrm{r} + 2)}{3\rho_0 v^2} p$$
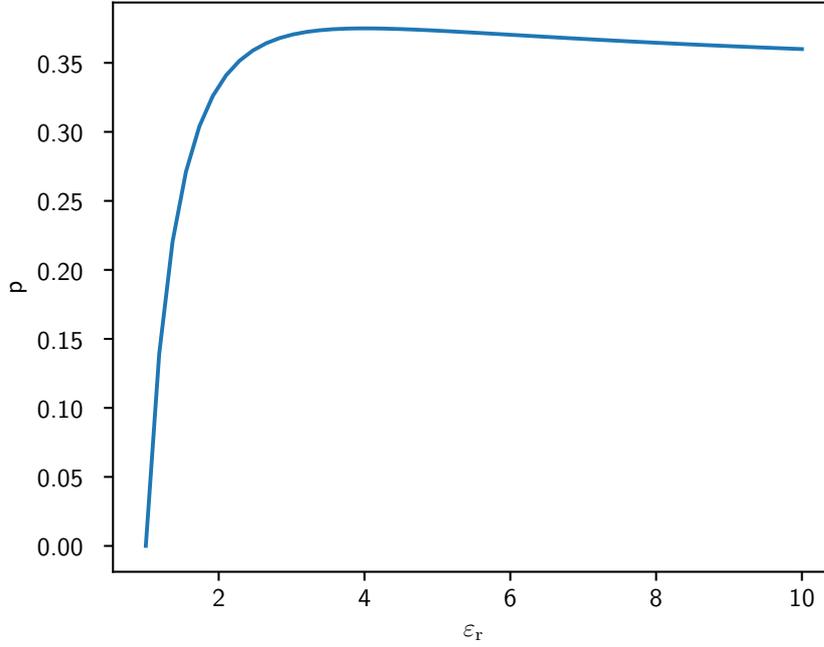
Figure 3.1: Simplified photoelastic constant $\mathfrak{p}$ as a function of ε_{r}.

where $K = \rho_0 v^2$ (which holds for fluids) was used [6]. Dry air at 0 °C (273 K) has the properties $\rho_0 = 1.293$ kg/m^3 and $v = 331.3$ m/s [45]. In addition, the relative permittivity cannot be approximated to 1 for this case, so the value of $\varepsilon_{\mathrm{r}} \approx 1.00059$ is used [53]. The simple model presented here can then be written as

$$\varepsilon_1 \approx 4.2 \cdot 10^{-9} p$$

while the model from [52] at 273 K gives

$$\varepsilon_1 \approx 4.1 \cdot 10^{-9} p$$

Thus, the simple model presented here shows good agreement with another model from the literature in air.

Analytical Modeling

This chapter utilizes the theory of photoelasticity together with electromagnetics to derive a model for the scattering of an electromagnetic wave against a photo-elastic perturbation. First, a general equation is derived from Maxwell's equations, and later this is used in a simple geometry to arrive at a radar equation. What is presented here is fairly condensed, with the full derivations being presented in appendix A.

4.1 Scattering in a perturbed dielectric

Scattering of electromagnetic waves in a dielectric perturbation is now considered in general. A full derivation can be found in appendix A.1, and only the main results are shown here. The starting point is Maxwell's equations for a linear, non-magnetic, source-free, isotropic dielectric. Note that the permittivity is not homogeneous.

$$\nabla \times \boldsymbol{\mathcal{E}} = -\mu_0 \frac{\partial \boldsymbol{\mathcal{H}}}{\partial t}$$

$$\nabla \times \boldsymbol{\mathcal{H}} = \frac{\partial (\varepsilon \boldsymbol{\mathcal{E}})}{\partial t}$$

$$\nabla \cdot (\varepsilon \boldsymbol{\mathcal{E}}) = 0$$

$$\nabla \cdot \boldsymbol{\mathcal{H}} = 0$$

The script letters are used here to indicate a time dependence as

$$\boldsymbol{\mathcal{E}}(\boldsymbol{r}, t) = \boldsymbol{E}(\boldsymbol{r}, t) e^{-i\omega t}$$

$$\boldsymbol{\mathcal{H}}(\boldsymbol{r}, t) = \boldsymbol{H}(\boldsymbol{r}, t) e^{-i\omega t}$$

A dielectric perturbation is defined as

$$\varepsilon = \varepsilon_0 (\varepsilon_{\mathrm{r}} + \varepsilon_1)$$

where ε_0 is the permittivity of free space, ε_{r} is the unperturbed value for relative permittivity in the material and ε_1 is a small perturbation around ε_{r}.

The electric field is split up into an incident field $\boldsymbol{E}_{\mathrm{i}}$ and a scattered field $\boldsymbol{E}_{\mathrm{sc}}$ such that $\boldsymbol{E} = \boldsymbol{E}_{\mathrm{i}} + \boldsymbol{E}_{\mathrm{sc}}$. If the scattered field is considered to be small compared

to the incident field (Born approximation), Maxwell's equations in this perturbed dielectric can be rewritten as (see appendix A.1.1-A.1.2)

$$\nabla^2 \boldsymbol{E}_{\mathrm{sc}} + k^2 \boldsymbol{E}_{\mathrm{sc}} = -k^2 \frac{\varepsilon_1}{\varepsilon_{\mathrm{r}}} \boldsymbol{E}_{\mathrm{i}} - \frac{1}{\varepsilon_{\mathrm{r}}} \nabla(\boldsymbol{E}_{\mathrm{i}} \cdot \nabla \varepsilon_1) - \frac{k^2}{\varepsilon_{\mathrm{r}}} \boldsymbol{E}_{\mathrm{di}}$$

where $k = \omega/c$ is the wavenumber, $c = 1/\sqrt{\mu_0 \varepsilon_0 \varepsilon_{\mathrm{r}}} = c_0/\sqrt{\varepsilon_{\mathrm{r}}}$ is the speed of light in the material and $\boldsymbol{E}_{\mathrm{di}}$ contains terms with time derivatives. An integral form is written as (see appendix A.1.2)

$$
\begin{aligned}
\boldsymbol{E}_{\mathrm{sc}}(\boldsymbol{r}, t) = {}& \frac{1}{4\pi\varepsilon_{\mathrm{r}}} \int_{V_{\mathrm{sc}}} \frac{\mathrm{e}^{\mathrm{i}k|\boldsymbol{r}-\boldsymbol{r'}|}}{|\boldsymbol{r}-\boldsymbol{r'}|} \\
& \cdot \left(k^2 \varepsilon_1(\boldsymbol{r'}, t) \boldsymbol{E}_{\mathrm{i}}(\boldsymbol{r'}, t) + \nabla \left(\boldsymbol{E}_{\mathrm{i}}(\boldsymbol{r'}, t) \cdot \nabla \varepsilon_1(\boldsymbol{r'}, t) \right) + k^2 \boldsymbol{E}_{\mathrm{di}}(\boldsymbol{r'}, t) \right) \mathrm{d}v'
\end{aligned}
\tag{4.1}
$$

where

$$
\begin{aligned}
\boldsymbol{E}_{\mathrm{di}}(\boldsymbol{r'}, t) = {}& \frac{2\mathrm{i}\varepsilon_{\mathrm{r}}}{\omega} \frac{\partial}{\partial t} \left(\boldsymbol{E}_{\mathrm{i}}(\boldsymbol{r'}, t) \right) + \frac{2\mathrm{i}}{\omega} \frac{\partial}{\partial t} \left(\varepsilon_1(\boldsymbol{r'}, t) \boldsymbol{E}_{\mathrm{i}}(\boldsymbol{r'}, t) \right) \\
& - \frac{\varepsilon_{\mathrm{r}}}{\omega^2} \frac{\partial^2}{\partial t^2} \left(\boldsymbol{E}_{\mathrm{i}}(\boldsymbol{r'}, t) \right) - \frac{1}{\omega^2} \frac{\partial^2}{\partial t^2} \left(\varepsilon_1(\boldsymbol{r'}, t) \boldsymbol{E}_{\mathrm{i}}(\boldsymbol{r'}, t) \right)
\end{aligned}
$$

This gives the scattered field due to a small perturbation ε_1 in a single-scattering (Born) approximation.

4.2   Radar equation for simple photoelastic interaction

The scattering integral is now solved for a simple geometry and material model to obtain a radar equation. A full derivation can be found in A.2, while only the main results are shown here. First, the geometry is defined as shown in figure 4.1. The xy-plane is defined as the plane formed by the acoustic and electromagnetic wavevectors (they are assumed to be non-parallel). The scattering volume is a cuboid with dimensions L_x, L_y and L_z. It is centered in the origin of the coordinate system, and both the acoustic and electromagnetic waves are approximated as plane waves close to the origin. Thus, the electromagnetic and dielectric perturbation fields near the origin are defined as

$$\boldsymbol{E}_{\mathrm{i}}(\boldsymbol{r'}, t) = \boldsymbol{E}_{\mathrm{i}}(\boldsymbol{r'}) = \boldsymbol{E}_{\mathrm{i0}} \mathrm{e}^{\mathrm{i}\boldsymbol{k}\cdot\boldsymbol{r'}}$$

$$\varepsilon_1(\boldsymbol{r'}, t) = \frac{\varepsilon_{\mathrm{r}}^2 \mathfrak{p}}{K} p_0 \cos(\boldsymbol{q} \cdot \boldsymbol{r'} - \Omega t)$$

Here, $\boldsymbol{E}_{\mathrm{i0}}$ is the complex field amplitude at the origin ($-\mathrm{i}\omega t$ time-dependence separated) and $\boldsymbol{k}$ is the electromagnetic wavevector. The scalar photoelastic relation from equation (3.4) has been used, where $\mathfrak{p}$ is the photoelastic constant, p_0 is the acoustic pressure amplitude at the origin, K is the bulk modulus, $\boldsymbol{q}$ is the acoustic wavevector and Ω the acoustic frequency.

The electromagnetic polarization is assumed to be in z, $\boldsymbol{E}_{\mathrm{i0}} \parallel \hat{\boldsymbol{z}}$, far-field is assumed and the condition $\Omega \ll \omega$ is assumed to hold. For this problem, equation
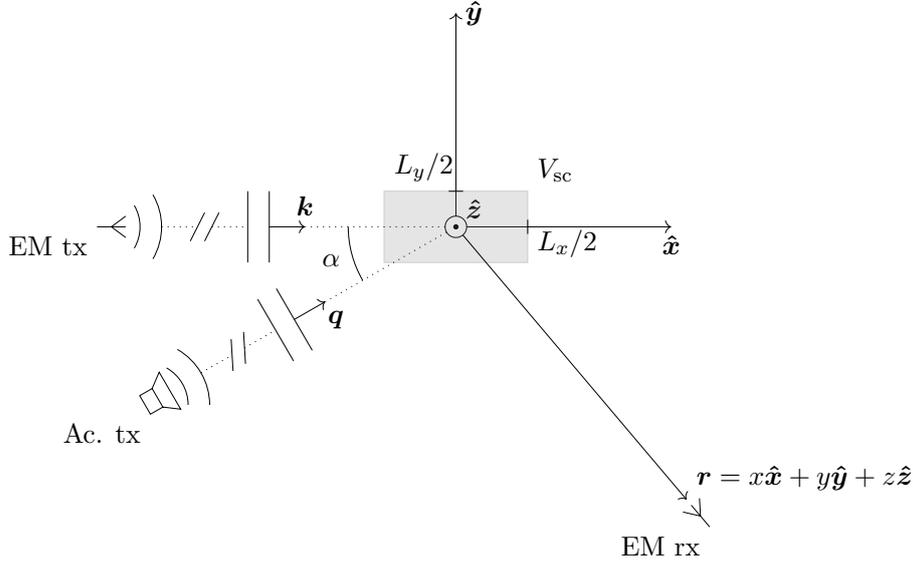
Figure 4.1: Geometry for the scattering problem.

(4.1) is written as (see appendix A.2.1)

$$\boldsymbol{E}_{\mathrm{sc}}(\boldsymbol{r}, t) = \frac{\varepsilon_{\mathrm{r}} k^2 \mathrm{e}^{\mathrm{i}kr} \boldsymbol{E}_{\mathrm{i}0} \mathfrak{p} p_0}{8\pi r K}$$
$$\cdot \left(\mathrm{e}^{-\mathrm{i}\Omega t} \int_{V_{\mathrm{sc}}} \mathrm{e}^{\mathrm{i}(k(\hat{\boldsymbol{k}}-\hat{\boldsymbol{r}})+\boldsymbol{q})\cdot\boldsymbol{r}'} \mathrm{d}v' + \mathrm{e}^{\mathrm{i}\Omega t} \int_{V_{\mathrm{sc}}} \mathrm{e}^{\mathrm{i}(k(\hat{\boldsymbol{k}}-\hat{\boldsymbol{r}})-\boldsymbol{q})\cdot\boldsymbol{r}'} \mathrm{d}v' \right)$$

Given the geometry in figure 4.1, the solution to this integral is written as (see appendix A.2.1)

$$\boldsymbol{E}_{\mathrm{sc}}(\boldsymbol{r}, t) = \boldsymbol{E}_{\mathrm{i}0} \left(E_{\mathrm{A}}^{+}(\boldsymbol{r}, t) + E_{\mathrm{A}}^{-}(\boldsymbol{r}, t) \right)$$

where

$$E_{\mathrm{A}}^{\pm}(\boldsymbol{r}, t) = \frac{\varepsilon_{\mathrm{r}} k^2 \mathrm{e}^{\mathrm{i}kr} \mathfrak{p} p_0}{8\pi r K} L_x L_y L_z e^{\mp \mathrm{i}\Omega t} \Phi^{\pm}(\theta, \phi)$$

and

$$\Phi^{\pm}(\theta, \phi) = \mathrm{sinc}\left(\frac{L_x}{2\pi} \left(k - k \sin\theta\cos\phi \pm q\cos\alpha \right) \right)$$
$$\cdot \mathrm{sinc}\left(\frac{L_y}{2\pi} \left(-k \sin\theta\sin\phi \pm q\sin\alpha \right) \right)$$
$$\cdot \mathrm{sinc}\left(-\frac{L_z}{2\pi} k\cos\theta \right)$$

One important detail to note is that two distinct frequency components arise: one where the frequency is shifted up by Ω (E_{A}^{+}) and one where it is shifted down by Ω (E_{A}^{-}).

To obtain a more practical expression, the equations are now transformed into power. For this, the time-averaged Poynting vector is calculated as (see appendix A.2.2)

$$\left\langle \boldsymbol{S}_{\text{sc}}^{\pm} \right\rangle (\boldsymbol{r}) = \frac{1}{2} \text{Re} \left\{ \boldsymbol{E}_{\text{sc}}^{\pm}(\boldsymbol{r}, t) \times \boldsymbol{H}_{\text{sc}}^{\pm *}(\boldsymbol{r}, t) \right\} = \frac{\hat{\boldsymbol{r}}}{2\eta_0 \eta} |\boldsymbol{E}_{\text{i0}}|^2 |E_{\text{A}}^{\pm}(\boldsymbol{r}, t)|^2$$

where the time-dependence was removed by the absolute value. $|E_{\text{A}}^{\pm}(\boldsymbol{r}, t)|^2$ is given by

$$|E_{\text{A}}^{\pm}(\boldsymbol{r}, t)|^2 = \frac{\varepsilon_{\text{r}}^2 k^4 \mathfrak{p}^2 p_0^2}{64\pi^2 r^2 K^2} L_x^2 L_y^2 L_z^2 \Phi^{\pm}(\theta, \phi)^2$$

Using standard antenna parameters, the incident field can be written as (see appendix A.2.2)

$$|\boldsymbol{E}_{\text{i0}}|^2 = 2\eta_0 \eta \frac{P_{\text{T}} G_{\text{T}}}{4\pi R_{\text{T}}^2}$$

where η_0 is the wave impedance of free space, η is the relative wave impedance in the material, P_{T} is the power accepted by the antenna, G_{T} is the maximum gain of the antenna and R_{T} is the distance from the antenna to the scattering center. This is inserted into the time-average of the power density, giving

$$\left\langle \boldsymbol{S}_{\text{sc}}^{\pm} \right\rangle (\boldsymbol{r}) = \hat{\boldsymbol{r}} \frac{P_{\text{T}} G_{\text{T}}}{4\pi R_{\text{T}}^2} \frac{\varepsilon_{\text{r}}^2 k^4 \mathfrak{p}^2 p_0^2}{64\pi^2 r^2 K^2} L_x^2 L_y^2 L_z^2 \Phi^{\pm}(\theta, \phi)^2$$

Now the effects of the receiving antenna are considered. It is assumed that this antenna is optimally directed towards the scattering center. The received power can then be written as (see appendix A.2.2)

$$P_{\text{R}}^{\pm} = \frac{\lambda_{\text{R}}^2 G_{\text{R}}}{4\pi} \frac{P_{\text{T}} G_{\text{T}}}{4\pi R_{\text{T}}^2} \frac{\varepsilon_{\text{r}}^2 k^4 \mathfrak{p}^2 p_0^2}{64\pi^2 R_{\text{R}}^2 K^2} L_x^2 L_y^2 L_z^2 \Phi^{\pm}(\theta, \phi)^2$$

where G_{R} is the gain of the receiving antenna, λ_{R} the wavelength at the antenna (not necessarily the same as in the material) and R_{R} the distance between the scattering center and the receiver. The receiver is located in the direction (θ, ϕ) as seen from the scattering center. For a more traditional bistatic radar equation [54] this can be written as

$$P_{\text{R}}^{\pm} = \frac{P_{\text{T}} G_{\text{T}} G_{\text{R}} \lambda_{\text{R}}^2 \sigma^{\pm}(\theta, \phi)}{(4\pi)^3 R_{\text{T}}^2 R_{\text{R}}^2}$$

with the radar cross-section given by

$$\sigma^{\pm}(\theta, \phi) = \frac{\varepsilon_{\text{r}}^2 k^4 \mathfrak{p}^2 p_0^2}{16\pi K^2} L_x^2 L_y^2 L_z^2 \Phi^{\pm}(\theta, \phi)^2$$

When actually measuring a signal, signal-to-noise ratio (SNR) is an important quantity. The equation can be rewritten using SNR (see appendix A.2.3) as:

$$SNR_N^{\pm} = \frac{P_{\text{T}} G_{\text{T}} G_{\text{R}} \lambda_{\text{R}}^2 \sigma^{\pm}(\theta, \phi)}{(4\pi)^3 R_{\text{T}}^2 R_{\text{R}}^2 k_{\text{B}} T_0 B F} N \tag{4.2}$$

where k_B is Boltzmann's constant, T_0 is the standard temperature 290 K, B is the receiver bandwidth, F is the noise ratio of the receiver and N is the number of samples recorded. This equation assumes that coherent demodulation and integration is used to boost the SNR.

Inspection of the equations for either scattered power or SNR shows that all angular dependence is contained in the function $\Phi^\pm$. This depends on the observation angles θ, ϕ and the angle between EM and Ac. wavevectors α. Conditions for the angles maximizing $\Phi^\pm$ are derived in appendix A.3 and summarized as

$$\theta = \pi/2 \tag{4.3}$$

$$\cos\alpha = \mp\frac{q}{2k} = \mp\frac{\lambda}{2\Lambda} \tag{4.4}$$

$$\phi = \mp\pi + 2\alpha \tag{4.5}$$

The $\mp$-sign here is related to the $\pm$-sign indicating frequency shift of the scattered wave. These equations correspond directly to the Bragg condition used in acousto-optics (see appendix A.3). This gives the model some validation since the acousto-optic Bragg condition is derived from a slightly different starting point, but for the same basic phenomenon [25].

4.2.1 Refined interaction region

The analytical results presented above are based on a cuboid interaction region. This makes for simple calculations and is fairly straight-forward at a conceptual level. However, it is difficult to find good dimensions L_x, L_y, L_z based on a real-life system using electromagnetic antennas and ultrasonic transducers. For this reason, the interaction region was refined for simple adaptation to real-life parameters. Other idealizations such as plane waves were still kept. The interaction region was now based on abrupt beams where the fields behave as plane waves inside of the beam diameter and are zero outside. Two crossing beams form a parallelogram as shown in figure 4.2. This new interaction region alters the derivation somewhat in that the scattering integral (4.1) is calculated over another region. The resulting scattered field is given by (see appendix A.2.4)

$$\boldsymbol{E}_{\mathrm{sc,p}}(\boldsymbol{r},t) = \boldsymbol{E}_{\mathrm{i0}}\left(E_{\mathrm{A,p}}^+(\boldsymbol{r},t) + E_{\mathrm{A,p}}^-(\boldsymbol{r},t)\right)$$

where

$$E_{\mathrm{A,p}}^\pm(\boldsymbol{r},t) = \frac{\varepsilon_\mathrm{r} k^2 \mathrm{e}^{ikr}\mathfrak{p}p_0}{8\pi r K}\frac{d_\mathrm{a}d_\mathrm{e}L_z}{\sin\alpha}e^{\mp i\Omega t}\Phi_\mathrm{p}^\pm(\theta,\phi)$$

and

$$\Phi_\mathrm{p}^\pm = \mathrm{sinc}\left(\frac{d_\mathrm{a}}{2\pi\sin\alpha}(k - k\sin\theta\cos\phi \pm q\cos\alpha)\right)$$

$$\cdot \mathrm{sinc}\left(\frac{d_\mathrm{e}}{2\pi\tan\alpha}(k - k\sin\theta(\cos\phi + \sin\phi\tan\alpha) \pm q(\cos\alpha + \sin\alpha\tan\alpha))\right)$$

$$\cdot \mathrm{sinc}\left(-\frac{L_z}{2\pi}k\cos\theta\right)$$

Figure 4.2:   Parallelogram interaction region. Electromagnetic beam diameter d_e, acoustic beam diameter d_a, angle between wavevectors α.

This is quite similar to the cuboid result, with the differences being in the interaction volume factor $d_\mathrm{a}d_\mathrm{e}L_z/\sin\alpha$ instead of $L_xL_yL_z$ in E_A and the function for angular dependence $\Phi^{\pm}$. This result is easily transferable to radar equations for power and SNR by using a new radar cross-section, written as

$$\sigma_\mathrm{p}^{\pm}(\theta,\phi) = \frac{\varepsilon_\mathrm{r}^2 k^4 \mathfrak{p}^2 p_0^2}{16\pi K^2} \frac{d_\mathrm{a}^2 d_\mathrm{e}^2 L_z^2}{\sin^2\alpha} \Phi_\mathrm{p}^{\pm}(\theta,\phi)^2 \tag{4.6}$$

It can be shown (see appendix A.3.4) that the same conditions for maximizing Φ hold for this refined interaction region as for the cuboid interaction region, i.e. equations (4.3), (4.4) and (4.5). One thing to keep in mind though, is that the parallelogram geometry has a factor $1/\sin\alpha$ in the interaction region which is not present in the cuboid geometry. The effect of this is that the angle α for maximum scattering can be shifted down in the $(-)$ case and up in the $(+)$ case. The exact shift depends highly on the geometry of the interaction region (see appendix A.3.4).

4.2.2   2D solution

When comparing analytical results to simulation results it is important to use the same assumptions for both. In the analytical derivations, 3D space has been

assumed while simulations are done in 2D. To be able to compare results, a 2D solution to the problem was calculated. Much of the derivations are similar, and only the results are shown here (see appendix A.2.5 for full derivations). The Poynting vector of the scattered field in 2D can be written as (see appendix A.2.5)

$$\left\langle \boldsymbol{S}_{\text{sc,2D}}^{\pm} \right\rangle (\boldsymbol{r}) = \frac{\hat{\boldsymbol{r}}}{2\eta_0\eta}|\boldsymbol{E}_{\text{i0}}|^2|E_{\text{A,2D}}^{\pm}(\boldsymbol{r},t)|^2 \tag{4.7}$$

where $|E_{\text{A,2D}}^{\pm}(\boldsymbol{r},t)|^2$ is given by

$$|E_{\text{A,2D}}^{\pm}(\boldsymbol{r},t)|^2 = \frac{\varepsilon_{\text{r}}^2 k^3 \mathfrak{p}^2 p_0^2}{8\pi r K^2} L_x^2 L_y^2 \Phi_{\text{2D}}^{\pm}(\theta,\phi)^2$$

and

$$\Phi_{\text{2D}}^{\pm}(\theta,\phi) = \operatorname{sinc}\left(\frac{L_x}{2\pi}(k - k\cos\phi \pm q\cos\alpha)\right) \operatorname{sinc}\left(\frac{L_y}{2\pi}(-k\sin\phi \pm q\sin\alpha)\right)$$

As for the 3D solution, the interaction region can be refined using a parallelogram geometry. This leads to the Poynting vector (see appendix A.2.5)

$$\left\langle \boldsymbol{S}_{\text{sc,2D,p}}^{\pm} \right\rangle (\boldsymbol{r}) = \frac{\hat{\boldsymbol{r}}}{2\eta_0\eta}|\boldsymbol{E}_{\text{i0}}|^2|E_{\text{A,2D,p}}^{\pm}(\boldsymbol{r},t)|^2 \tag{4.8}$$

where $|E_{\text{A,2D,p}}^{\pm}(\boldsymbol{r},t)|^2$ is given by

$$|E_{\text{A,2D,p}}^{\pm}(\boldsymbol{r},t)|^2 = \frac{\varepsilon_{\text{r}}^2 k^3 \mathfrak{p}^2 p_0^2}{8\pi r K^2} \frac{d_{\text{a}}^2 d_{\text{e}}^2}{\sin^2\alpha} \Phi_{\text{2D}}^{\pm}(\theta,\phi)^2$$

and

$$\Phi_{\text{2D,p}}^{\pm}(\theta,\phi) = \operatorname{sinc}\left(\frac{d_{\text{a}}}{2\pi\sin\alpha}(k - k\cos\phi \pm q\cos\alpha)\right)$$
$$\cdot\operatorname{sinc}\left(\frac{d_{\text{e}}}{2\pi\tan\alpha}(k - k(\cos\phi + \sin\phi\tan\alpha) \pm q(\cos\alpha + \sin\alpha\tan\alpha))\right)$$

These results are useful when comparing with simulation results since 2D geometries are much easier to simulate than 3D geometries.

Numerical Simulation

This chapter describes the numerical simulations used to verify analytical models and understand the problem better. Some general characteristics for all simulations are described first, with specifics for the individual studies presented later.

5.1 General Information

The problem was simulated in COMSOL Multiphysics for verification and further investigation of more complex scenarios than the one modeled analytically. The two physics interfaces used were the "Pressure Acoustics, Frequency Domain" from the basic COMSOL Multiphysics and "Electromagnetic Waves, Frequency Domain" from the RF Module. Models were built in 2D for computational speed. One simulation required 1 acoustic and 2 electromagnetic frequency domain simulations to be run, and parameter sweeps would multiply the number required. It was decided that 3D simulations would be too time consuming with little gain when compared with 2D.

The pressure acoustics model was used even though propagation in a solid medium was to be modeled. This was done under an assumption of pure p-wave propagation, which can be modeled using acoustic pressure with a different wave speed as shown in section 3.2.2. However, in these simulations the wave speed was calculated using the acoustic wave speed $v = \sqrt{K/\rho_0}$ which is only correct for p-waves in materials with negligible shear modulus [6]. The reason for this was that wave speed and density entered the COMSOL physics model at multiple places such as the boundary conditions which made it more difficult to determine exactly how to change the wave speed without affecting other parameters.

For all simulations the acoustic frequency was set to 450 kHz, which was used in acoustic frequency domain simulations. From this value and material properties, the acoustic wavelength Λ was determined. Using the desired angle α between beams and equation (4.4), the electromagnetic wavelength λ was calculated. From λ and material properties the electromagnetic frequency was calculated, which was used in electromagnetic frequency domain simulations. The electromagnetic frequency was approximately 61.29 GHz, where it was matched to the angles $\alpha = 40°$ (negative frequency shift) or $\alpha = 140°$ (positive frequency shift).

Since frequency domain simulations were used, individual simulation studies could only use one frequency at at time. The acoustic simulation used 450 kHz

while the electromagnetic simulations used 61.29 GHz (approximately). One effect of this was that when the relative permittivity change ε_1 was entered in the electromagnetic simulation, it was as a snapshot of the propagating wave. This was due to the very nature of frequency domain simulations where explicit time-dependence is separated from the equations. Without time-dependence, a result showing frequency shifts explicitly was not possible. For these kinds of results, a time-domain simulation with simultaneous calculation of acoustic and electromagnetic fields would be necessary.

5.1.1   Geometry and boundary conditions

The basic geometry is shown in figure 5.1 for the acoustic and electromagnetic simulations. The only difference in geometry between the two is the Perfectly Matched Layer (PML) which is used in the electromagnetic simulation but not the acoustic simulation. Additionally, the boundary conditions are different for the two simulations which is also shown. One boundary of special interest is that marked with measurement boundary in the figure. This is where the physics domain ends, and the fields were measured at this boundary for post-processing. The radius of the measurement boundary was 30Λ everywhere except for the apertures which were chords of this circle.

The PML was used to emulate an open boundary at the measurement boundary for the electromagnetic problem. It was a cylindrical type with center in the center of the geometry and a width of 2λ. It used polynomial coordinate stretching with a typical wavelength taken from the electromagnetic physics interface. The PML scaling factor and PML scaling curvature parameter were both set to 1. At the exterior boundary, a Perfect Electric Conductor (PEC) boundary condition was used.

The PML function was not available for the basic pressure acoustics interface used here. However, the Cylindrical Wave Radiation boundary condition was available and was used for the same purpose as a PML.

5.1.2   Tapering of apertures

To reduce sidelobe levels, both the electromagnetic and acoustic apertures had amplitude tapers applied to them. This had the effect of lowering the electric field or acoustic acceleration near the edges of apertures. The specific taper used was a Gaussian taper, which multiplies values at the aperture with a Gaussian function given by

$$\mathrm{e}^{-(Ay')^2}$$

where A affects the width of the taper and y' is a coordinate along the aperture with 0 in the center. Since the model was based on a circle and all apertures were modeled as straight lines on the edge of the circle, y' can be found by rotation of the original coordinate y by the angle ϕ. This transformation is given by

$$\begin{bmatrix} x' \\ y' \end{bmatrix} = \begin{bmatrix} \cos\phi & \sin\phi \\ -\sin\phi & \cos\phi \end{bmatrix} \begin{bmatrix} x \\ y \end{bmatrix}$$
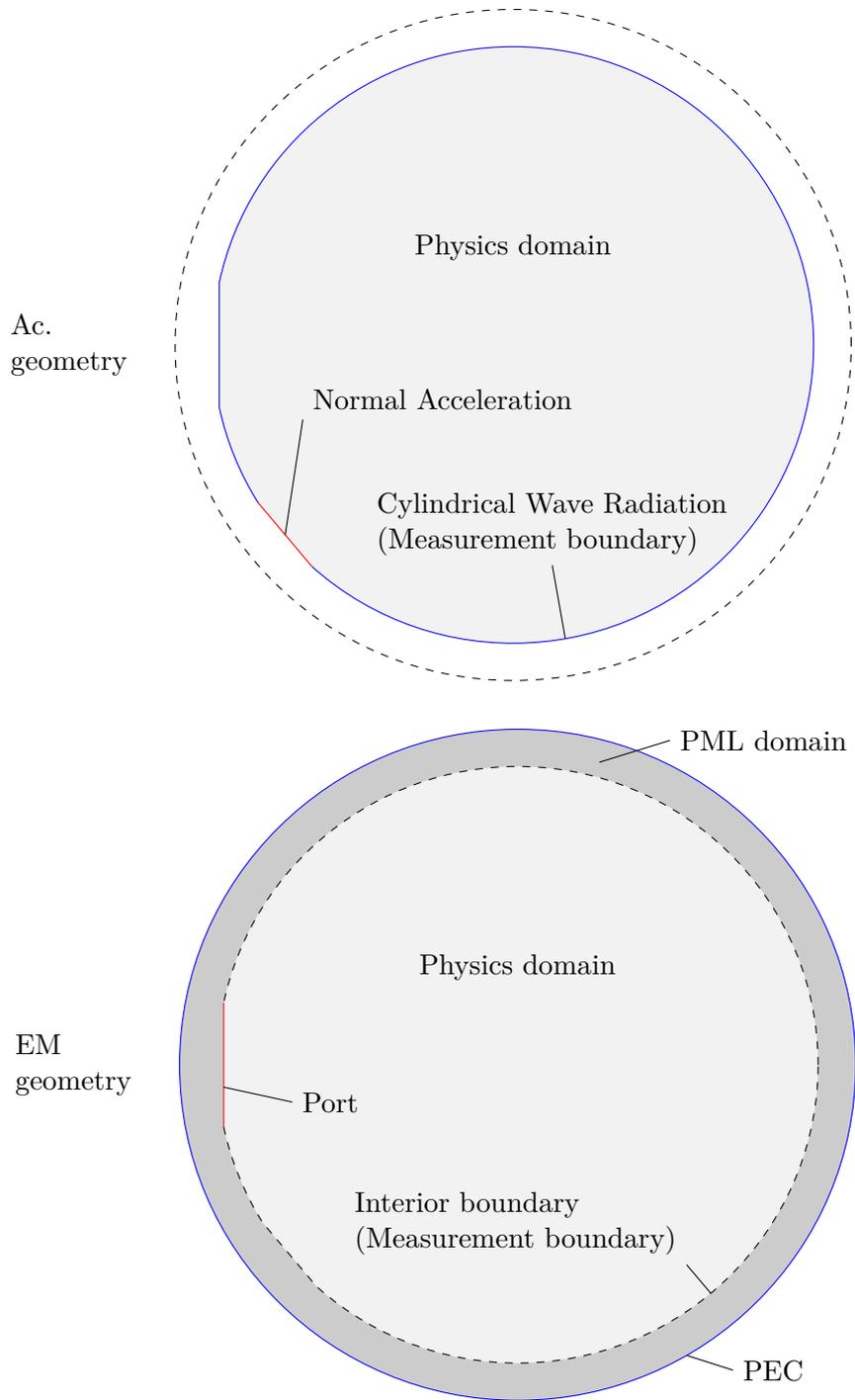
Figure 5.1: Simulation geometry with boundary conditions for Ac. and EM simulations.

which gives the equation for y'

$$y' = -x\sin\phi + y\cos\phi$$

The geometry is the same as previously shown in figure 4.1. As such, $\phi = \pi$ for EM and $\phi = \pi + \alpha$ for Ac. For the coefficient A, it was found that $A = 4/D$ gave a good taper for an aperture width D (the value of the taper function was close to zero at the edge of the aperture).

5.1.3   Modeling of Electromagnetic Aperture

An electromagnetic aperture was designed to produce a fairly low beam width while not taking up too much space on the boundary. The model used a "Port" boundary condition on a boundary segment with length $D = 8\lambda$. The port options "User Defined" and wave excitation were turned on. The port input power was set to 15 dBm. Due to it being located on an interior boundary, the slit condition was activated with a domain-backed slit. For the port mode, the electric field was set as the input quantity with a tapered field in z defined as

$$E_{0z} = e^{-(4y'/D)^2}$$

where y' is the coordinate $-y$ (since the electromagnetic aperture is fixed at $\phi = \pi$). The propagation constant was set to the wavenumber in the material using "emw.k".

5.1.4   Modeling of Acoustic Aperture

The qualities of beam width and space usage for the electromagnetic aperture were also taken into consideration in the design of the acoustic aperture. The model used a "Normal Acceleration" boundary condition on a boundary segment with length $D = 8\Lambda$. The acceleration was set to "Inward acceleration". The value of the acceleration amplitude was calculated from a displacement amplitude u_{p} using $a_0 = \Omega^2 u_{\mathrm{p}}$ (obtained by differentiating a plane wave by time twice). The displacement amplitude was set to 5 nm. The acoustic intensity obtained in COMSOL at this displacement amplitude was well within the levels of actual transducers [55]. The acceleration was tapered as

$$a_{\mathrm{n}} = a_0 e^{-(4(x\sin\alpha - y\cos\alpha)/D)^2}$$

where x and y are coordinates and α the angle between wavevectors.

5.1.5   Photoelasticity model

To model photoelasticity in COMSOL, equation (3.4) was used with the photo-elastic constant defined by equation (3.5). This was implemented using variables depending on the acoustic pressure. When an acoustic pressure field was available to COMSOL (i.e. after a finished acoustic simulation) the ε_1 field was calculated. This could then be added to ε_{r} of the material for use in electromagnetic simulations.

5.1.6 Material

The material model used was based on a foam core for sandwiched composite structures. The reason for this was that foam material is fairly homogeneous and isotropic compared to honeycombs. The specific core selected was Divinycell HT251 from Diab Group, which is an aerospace core with applications described as "Primary structures, radomes, control surfaces and interior components" [56]. The relevant material properties were density (ρ_0), bulk modulus (K) and relative permittivity (ε_r). These were $\rho_0 = 250$ kg/m^3, $K = 400$ MPa (nominal) and $\varepsilon_r = 1.29$ [56]. In COMSOL, the required properties were density, speed of sound, relative permittivity, relative permeability and electrical conductivity. The speed of sound was calculated using $v = \sqrt{K/\rho_0}$, the relative permeability was set to 1 and the conductivity to 0. The assumption was that the material was perfectly non-conducting and non-magnetic. The relative permittivity was able to be perturbed by acoustic pressure using the variables from the photoelasticity model.

5.1.7 Mesh

Two meshes were used in simulations: one for the acoustic simulation and one for the electromagnetic simulation. The reason for this was primarily the difference in wavelength.

The acoustic mesh was defined on both the physics domain and PML domain even though only the physics domain was simulated in this case. A free triangular mesh was used with element size between $\Lambda/10$ and $\Lambda/10 \cdot 3 \cdot 10^{-2}$ in the physics domain, and "Fine" in the PML domain. Before running the free triangular meshing, the mesh was defined on the measurement boundary.

The electromagnetic mesh used a free triangular mesh in the physics domain and a mapped mesh in the PML domain. The element size in the physics domain was between $\lambda/10$ and $\lambda/10 \cdot 3 \cdot 10^{-2}$. Before running the free triangular meshing, the mesh was defined on the measurement boundary.

5.1.8 Simulation studies

Before starting simulations, the frequencies, material and geometry were defined. The geometry was in many parts defined as a function of the frequencies and material properties in order to obtain reasonably sized domains and apertures placed according to the Bragg condition.

For the actual simulations, the work flow is illustrated in figure 5.2. First, an acoustic frequency domain study was run using the acoustic frequency and mesh. The result from this was a complex pressure field. Real part convention was used when relating this complex field to the actual pressure.

To transform the pressure to relative permittivity, a variable was used in the material model to define the relative permittivity. This variable took the real part of the pressure field as its input, and used equations (3.3) and (3.4) to calculate a corresponding field for ε_1.

An electromagnetic frequency domain study was now run using the electromagnetic frequency and mesh. The acoustic study was used for calculating initial

values for variables not solved for. This was necessary for the pressure field to be available in both studies. Since the photoelastic effect is usually very small, the scattered field was not possible to distinguish with the incident field present. To be able to isolate the scattered field, two simulations were run: one where the relative permittivity of the material was unperturbed and one where it was perturbed by ε_1. The difference between fields resulting from these simulations were identified as the scattered fields.

Due to limitations in the post-processing capabilities of COMSOL, the E_z, H_x and H_y fields at the boundary were exported together with x and y coordinates after the electromagnetic simulation was finished. This was done both for the simulation with and without perturbation.
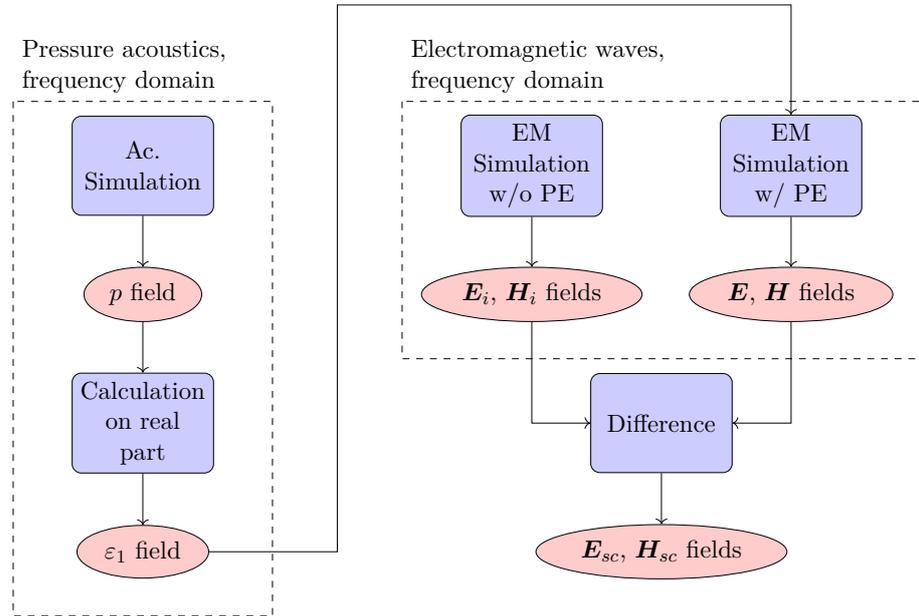

Figure 5.2: Simulation flow chart

5.1.9   Post-processing

The simulation results were further processed in SciPy for better visualization of the results than what was possible in COMSOL. The E_z, H_x and H_y fields (both with and without photoelastic perturbation) on the domain boundary were exported from COMSOL and loaded in SciPy. The differences between the fields were calculated to obtain the scattered fields. The time-averaged Poynting vector (for scattered fields) was then calculated as

$$\langle S_{\text{sc},x} \rangle = -\frac{1}{2}\text{Re}\{E_{\text{sc},z}H_{\text{sc},y}^*\}$$

$$\langle S_{\text{sc},y} \rangle = \frac{1}{2}\text{Re}\{E_{\text{sc},z}H_{\text{sc},x}^*\}$$

Due to it being easier to visualize, the magnitude of the time-averaged Poynting vector was also calculated. Using the x and y coordinates, the observation angle ϕ_{obs} for each point was calculated and the data was sorted according to this. To calculate the total scattered power, the normal component of the time-averaged Poynting vector at the measurement boundary was calculated. This was done using

$$\hat{\boldsymbol{n}} \cdot \langle \boldsymbol{S} \rangle \approx \langle S_{\text{sc},x} \rangle \cos(\phi_{\text{obs}}) + \langle S_{\text{sc},y} \rangle \sin(\phi_{\text{obs}})$$

where $\hat{\boldsymbol{n}}$ is the normal vector to the measurement boundary. This is an approximate relation since the normal vector $\hat{\boldsymbol{n}} = \hat{\boldsymbol{x}} \cos \phi + \hat{\boldsymbol{y}} \sin \phi$ holds for a circular boundary. Due to the apertures, the measurement boundary is not perfectly circular, but it is still fairly close. The normal component of the Poynting vector was then integrated over the full measurement boundary using the trapezoidal method, with distance between data points calculated from the coordinates.

For plotting of the time-averaged Poynting vector magnitude, the propagation angle ϕ_{prop} was calculated for each data point. The two angles ϕ_{obs} and ϕ_{prop} are shown in figure 5.3 together with the geometry of the problem. From this figure it can be seen that the observation angle depends highly on the measurement point while the propagation angle is a property of the scattered field. For this reason, the propagation angle was used in plots for the angle ϕ.
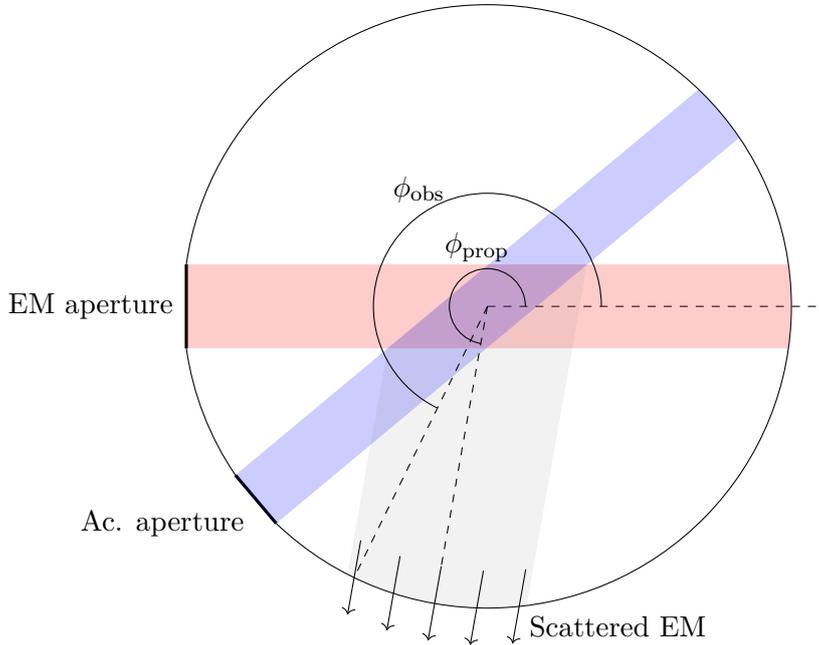

Figure 5.3: Propagation and observation angle near the edge of the scattered beam.

5.2   Specific Studies

This section contains details specific to the different studies run in COMSOL.

5.2.1   Sweep of angle α

To compare with the results from section 4.2 the frequencies of the acoustic and electromagnetic waves were matched to a Bragg angle of 40° while the angle α between the wavevectors was swept between $\pm 5°$ of the optimal angle. This was done both for (+) and (−) scattering by sweeping around either $\alpha = 40°$ or $\alpha = 140°$, as these angles are the ones given by equation (4.4) as angles for maximum scattering.

The maximum Poynting vector magnitude was calculated for each α and plotted against this angle. This was done to find the angle α giving maximum scattering. For comparison, the 2D versions of Poynting vector were also plotted for both cuboid and parallelogram geometries using equation (4.7) and (4.8). The dimensions were selected such that d_a was the acoustic aperture width, d_e the electrical aperture width and $L_x = d_e$, $L_y = d_a$. These dimensions were selected since they were easy to relate to the model, but had some drawbacks since the interaction regions were not that well reproduced. The equations (4.7) and (4.8) also require values for $\boldsymbol{E}_{i0}$ and p_0. These were selected as the peak field values from the COMSOL simulations. The effect of this was obviously that the analytical comparisons became dependent on some part of the simulations. These peak field values would not be correct amplitudes for use in the equations since the waves in simulations were tapered. Due to this, the Poynting vector was multiplied by a correction factor to ensure that the plane waves in analytical solutions would have the same total power as the tapered beams where the peak amplitudes were obtained.

To obtain the correction factor, it was assumed that the total power in a simulated beam P_{beam} would be related to the taper function as

$$P_{\text{beam}} = S_{\text{beam}} \int_{-\infty}^{\infty} \left(e^{-(4y'/D)^2} \right)^2 \mathrm{d}y'$$

$$= S_{\text{beam}} \int_{-\infty}^{\infty} e^{-(4\sqrt{2}y'/D)^2} \mathrm{d}y' = S_{\text{beam}} D \sqrt{\frac{\pi}{32}}$$

where S_{beam} is a power density amplitude and a standard Gaussian integral solution was used. The taper function was assumed to be zero outside of the region $-D/2 < y' < D/2$ so that an infinite integral could be used. Since the taper function was defined to have this property, it was not an issue. The goal of the correction factor was to ensure that the total power of a plane wave inside a beam diameter D was equal to the total power of the simulated beam. For this plane wave, the total power is simply a power density amplitude S_{plane} multiplied with the beam diameter. For equal power it should then hold that

$$S_{\text{plane}} D = S_{\text{beam}} D \sqrt{\frac{\pi}{32}}$$

If D is canceled out, the correction factor when going from a beam amplitude to a plane wave amplitude is $\sqrt{\pi/32}$. Since this was done for both the acoustic

and electromagnetic fields, a total correction factor of $\pi/32$ was applied to the analytical 2D Poynting vector.

To compare the simulated values for total scattered power with the analytical ones, the normal component of the analytical Poynting vector at the measurement boundary was calculated. The measurement boundary was approximated by a circle with the radius 30Λ, which was also the value for r. Due to the circular boundary and the vectors in equations (4.7) and (4.8) being directed in $\hat{\boldsymbol{r}}$, the normal component of the Poynting vector was equal to its magnitude. The normal component was then integrated over the full boundary numerically using the trapezoid method.

5.2.2   Conductive Defect

To examine the effect of a defect with electromagnetic contrast but no acoustic contrast, simulations were run with a conductive defect. The geometry of this problem was based on the basic geometry shown in figure 5.1. The addition was a circle in the center of the physics domain representing a defect. This had the diameter equal to the electromagnetic wavelength λ. The material in this region was the same as in the physics domain, but with a nonzero electric conductivity.

To demonstrate the effect of conductivity, the electric conductivity of the defect was swept between 0 and 10 S/m in steps of 1 S/m. The angle α was fixed at 40° with λ matched to Λ and this angle.

5.2.3   Mechanical Defect

To examine the effect of a defect with acoustic contrast but no electromagnetic contrast, simulations were run with a mechanical defect. The mechanical property which was altered was the density since this does not affect the photoelastic relation from equation (3.4) (for a constant bulk modulus). Since the bulk modulus was kept constant, the acoustic wave speed was changed as the density changed. The geometry of this problem was the same as for the conductive defect simulation. The material inside of the defect region was the same as in the physics domain, but with altered density.

To demonstrate the effect of density change, the density was swept between 100 and 400 kg/m^3 in steps of 25 kg/m^3. The angle α was fixed at 40° with λ matched to Λ and this angle.

Results and Discussion

This chapter presents results from the numerical simulations with comparisons to the analytical models. These are discussed and related to the problem of NDT. Discussions for possible experiments in the future are also presented here, with some examples of power estimates related to these. Finally, the work is summarized and conclusions are drawn.

6.1 Numerical Simulation Results

In this section, the results from the numerical simulations described in chapter 5 are shown and described. Comparisons are made with the analytical models from chapter 4. These analytical models were all based on the assumption that $\Omega \ll \omega$, which is the case for the frequencies 450 kHz and 61.29 GHz which were used.

6.1.1 Sweep of angle α

The results from the sweep of the angle between wavevectors α are shown in figures 6.1 - 6.7 for both negative $(-)$ and positive $(+)$ frequency shifts. Figure 6.1 and 6.2 show the incident waves, scattered wave and Poynting vector for the entire domain and for both $(-)$ and $(+)$. These are shown mostly to visualize the interaction qualitatively while the results from post-processing of values at the measurement boundary are more useful for quantitative results.

Figure 6.3 shows that the peak photoelastically scattered Poynting vector magnitude was maximized at an angle $\alpha = 40°$ for $(-)$ scattering (negative frequency shift) and at $\alpha = 140°$ for $(+)$ scattering (positive frequency shift). The analytical comparisons are shown for the cuboid and parallelogram geometries. It can be seen that the peak of the curves is at the same angle α for the simulated values and the cuboid analytical model. Since the wavelengths were selected such that these angles would maximize the scattering (using equation (4.4)), this would be expected. The parallelogram analytical model has its maximum at another angle α, but as discussed in section 4.2.1 there could be a slight change in this angle α. The predicted change was that the angle α of maximum scattering would shift down for $(-)$ scattering and up for $(+)$ scattering, which is what can be seen in figure 6.3.

If the analytical curves for $(+)$ and $(-)$ scattering are compared, the levels of power density are the same. For the simulated values however, the $(+)$ scattering power density levels are lower than those for $(-)$ scattering. This can be explained using the width of the scattered beams. In figure 6.7 it can be seen that the total scattered power is the same for both $(+)$ and $(-)$. A lower power density of the $(+)$ beam would require a wider scattered beam, which can be observed to be the case if the scattered electric fields in figure 6.1 and 6.2 are compared.
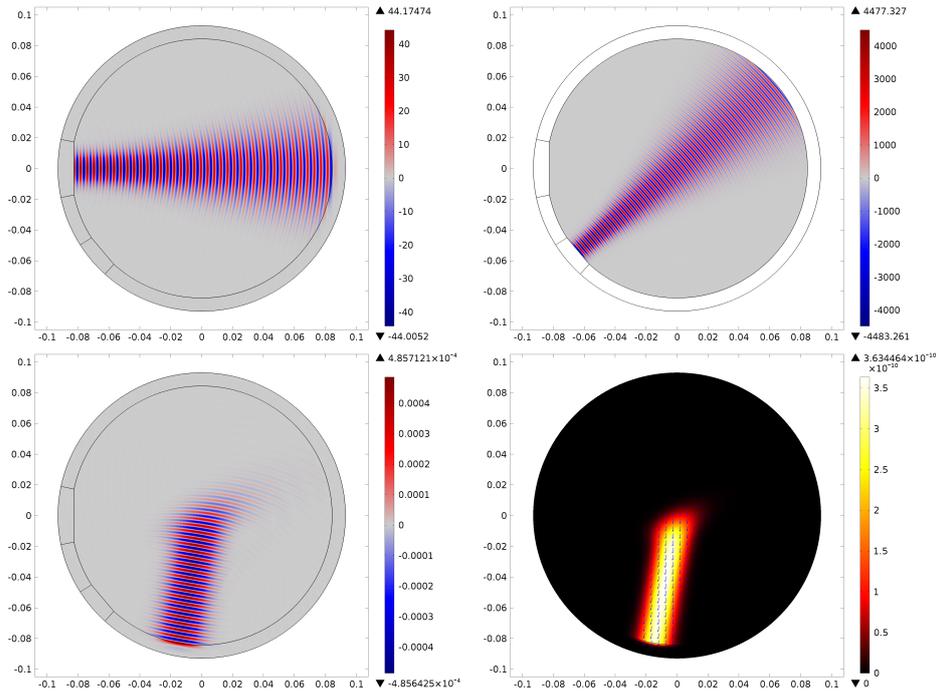

Figure 6.1: Results of $(-)$ scattering angle sweep for entire domain. Top left: incident electric field [V/m]. Top right: incident pressure [Pa]. Bottom left: Photoelastically scattered electric field [V/m]. Bottom right: Photoelastically scattered Poynting vector [W/m^2]

What is interesting is that the α shift for the parallelogram geometry is not seen in the simulation results, even though the parallelogram geometry should be more realistic than the cuboid one. This might be due to the length of the α shift being strongly related to interaction region geometry. As described before, the dimensions of the interaction regions were selected using the aperture widths. Since the actual beam diameters were not constant, the dimensions of the interaction region should be slightly larger. Increasing these dimensions slightly lead to the parallelogram curve having its peak closer to the same α as simulations. If the simulation curve is observed, a slight asymmetry can be seen around the α for the peak (easier to see for $(-)$ than for $(+)$). This might be indication of a very slight shift in α compared with $40°/140°$, but difficult to exactly replicate analytically

with the geometry parameters available in the parallelogram model.
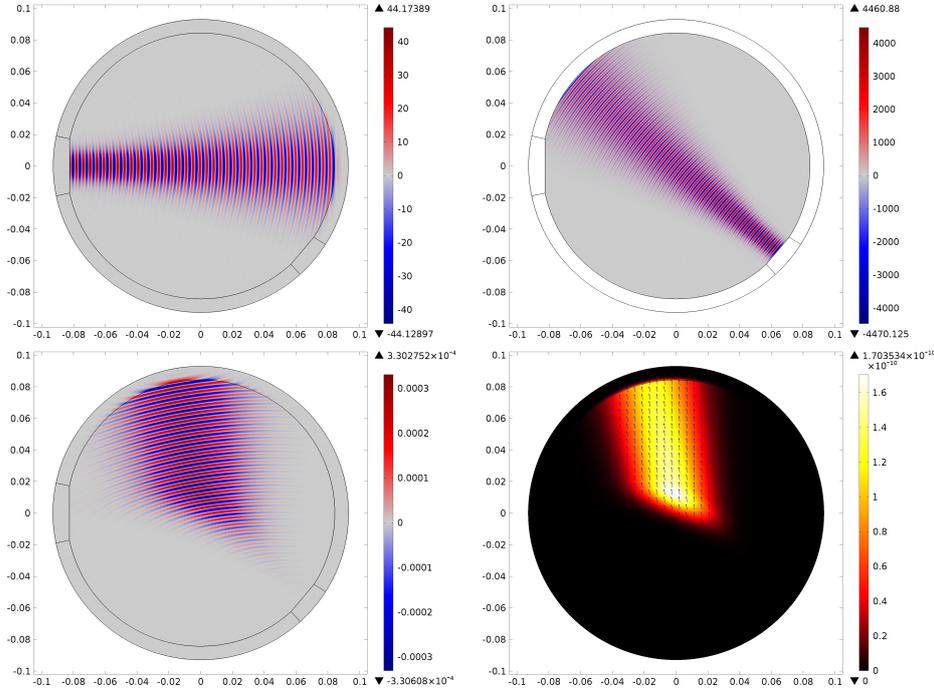
Figure 6.2: Results of $(+)$ scattering angle sweep for entire domain. Top left: incident electric field [V/m]. Top right: incident pressure [Pa]. Bottom left: Photoelastically scattered electric field [V/m]. Bottom right: Photoelastically scattered Poynting vector [W/m^2]

While the angle α of the peak in figure 6.3 shows fair correspondence between analytical and simulated cases, the magnitude of the Poynting vector is quite different. Neither of the analytical geometries lead to a correct shape of the curve or correct value for $|\langle \boldsymbol{S}_{\mathrm{sc}}\rangle|_{\mathrm{max}}$ when compared to the simulation. The reason behind this might be the interaction region not being the correct size. Neither the cuboid or parallelogram geometry takes into account the spreading nature of the simulated beams which affects the interaction region. For better correspondence, the dimensions of the interaction region might be estimated from the COMSOL simulations. However, requiring more data from simulations is not a strength of the analytical model.
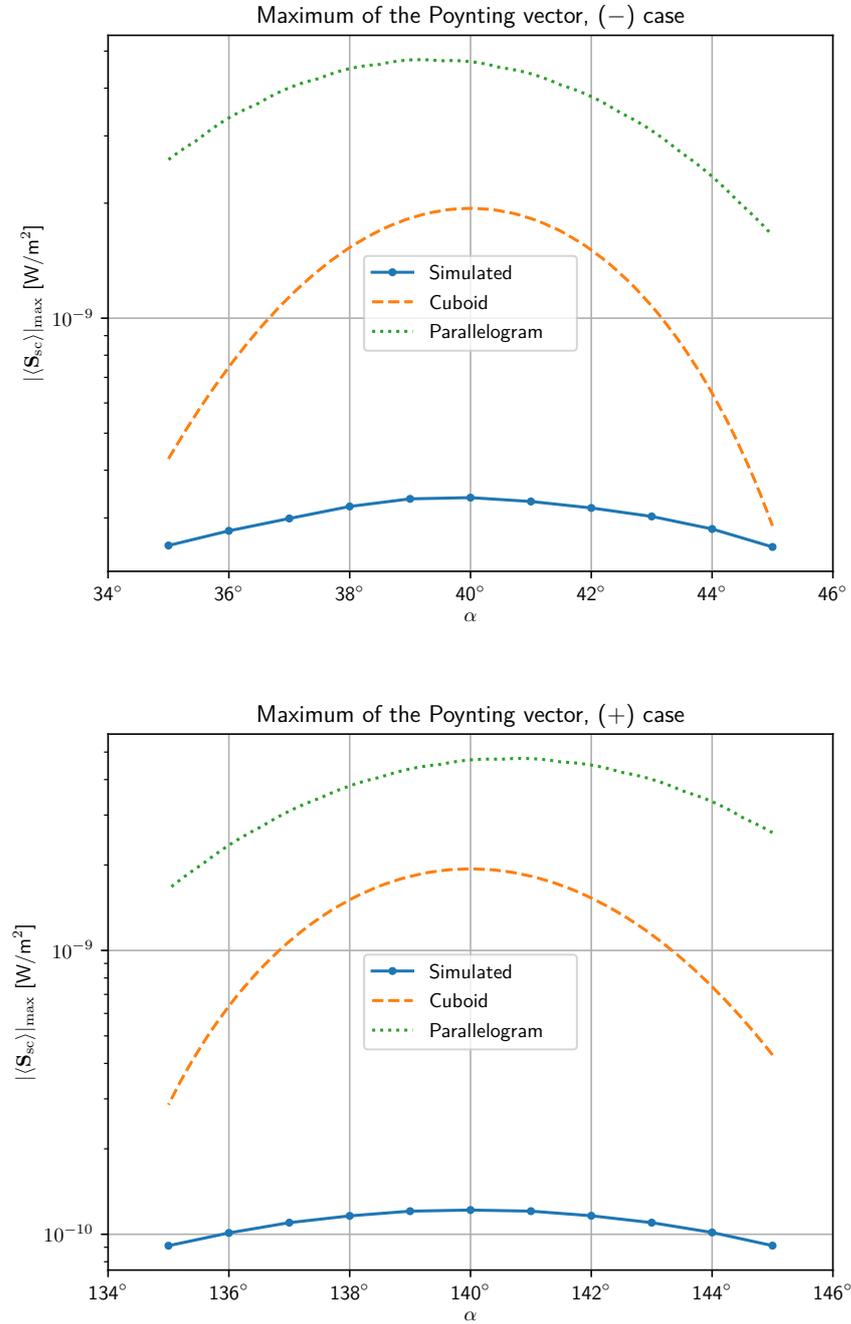
Figure 6.3:   Peak value of Poynting vector magnitude for different angles between wavevectors α. Analytical equivalents plotted for both cuboid and parallelogram geometries. Logarithmic scale.

Another reason for the difference in the shape of the curves in figure 6.3 might be that the analytical model is based entirely on plane waves. This means that a suboptimal angle α should not lead to much interaction. The simulation, on the other hand, uses more realistic wave propagation with cylindrical waves. A cylindrical wave can be decomposed into a sum of plane waves with different propagation direction [25, 57]. This essentially means that the condition in equation (4.4) is satisfied for every angle α for some combination of plane wave components. However, the plane wave components have different amplitudes and the strongest components are the ones with the same propagation direction as the original beams. This causes the Poynting vector magnitude to be smaller for suboptimal α, but still larger than if there had been no Bragg matched components at all.

Nevertheless, the peaks for simulation, cuboid and parallelogram cases in figure 6.3 are at angles α fairly close to each other and analytical values for $|\langle \boldsymbol{S}_{\mathrm{sc}} \rangle|_{\mathrm{max}}$ are at most within two orders of magnitude from simulated values. This is the case even though geometric parameters used in the analytical models could have been selected with more care.

Figure 6.4 shows a linear relationship between the angle α between incident wavevectors and the propagation angle ϕ_{prop}. This can be compared with the analytical result in equation (4.5), which gives a relationship valid at the point of maximum scattering. The propagation angles at $\alpha = 40°$ and $\alpha = 140°$ from the plot (the angles which maximized scattering) are $\phi_{\mathrm{prop}} = 260°$ and $\phi_{\mathrm{prop}} = 100°$ respectively. This is in agreement with the analytical values from equation (4.5). Further from these angles α, the analytical equation is no longer valid (since this is not at the point of maximum scattering). However, as discussed before the simulated beams can be decomposed as a sum of plane waves. This means that equation (4.5) is valid for some pair of plane wave components at every angle α.

Figure 6.5 shows the angular behavior of the Poynting vector magnitude in a simple way. What is clear is that the scattering is quite directive - the Poynting vector magnitude drops sharply for propagation angles deviating from that of the peak value. This could also be observed in figures 6.1 and 6.2 on the full domain.
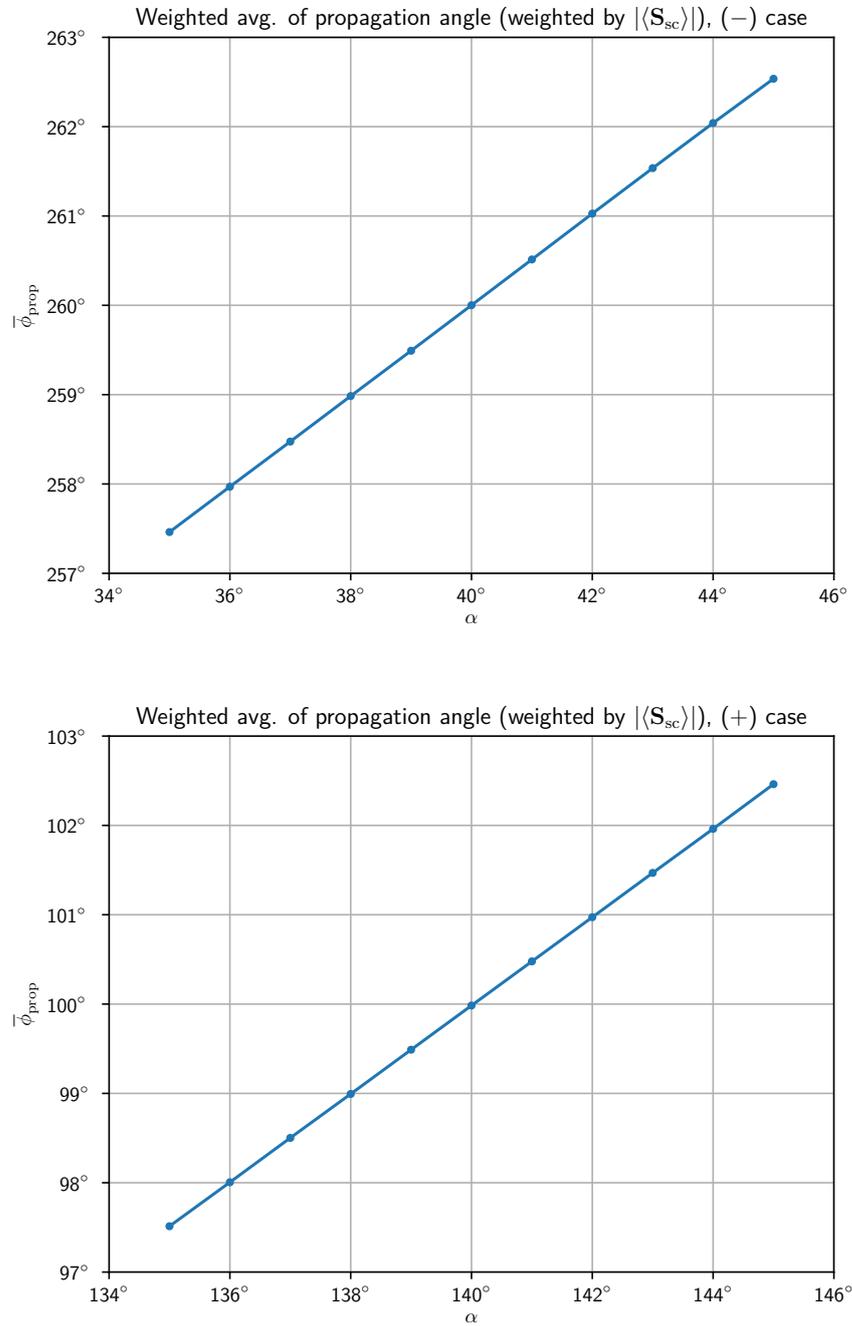
Figure 6.4: Weighted average of the propagation angle ϕ_{prop} as a function of angle between wavevectors α. Weighted by corresponding Poynting vector.

Normalized Poynting vector magnitude $|\langle \mathbf{S}_{\mathrm{sc}} \rangle| \, / \, |\langle \mathbf{S}_{\mathrm{sc}} \rangle|_{\mathrm{max}}$, $(-)$ case
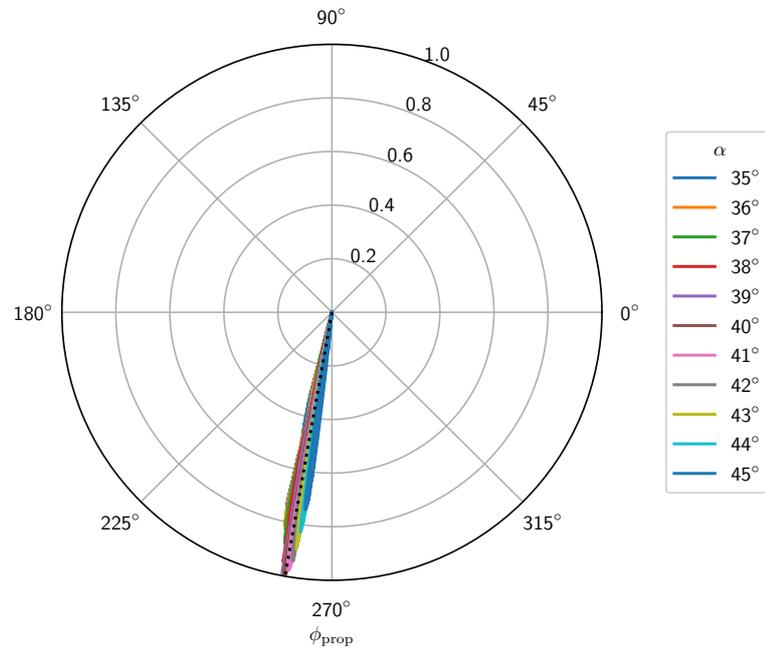
Normalized Poynting vector magnitude $|\langle \mathbf{S}_{\mathrm{sc}} \rangle| \, / \, |\langle \mathbf{S}_{\mathrm{sc}} \rangle|_{\mathrm{max}}$, $(+)$ case
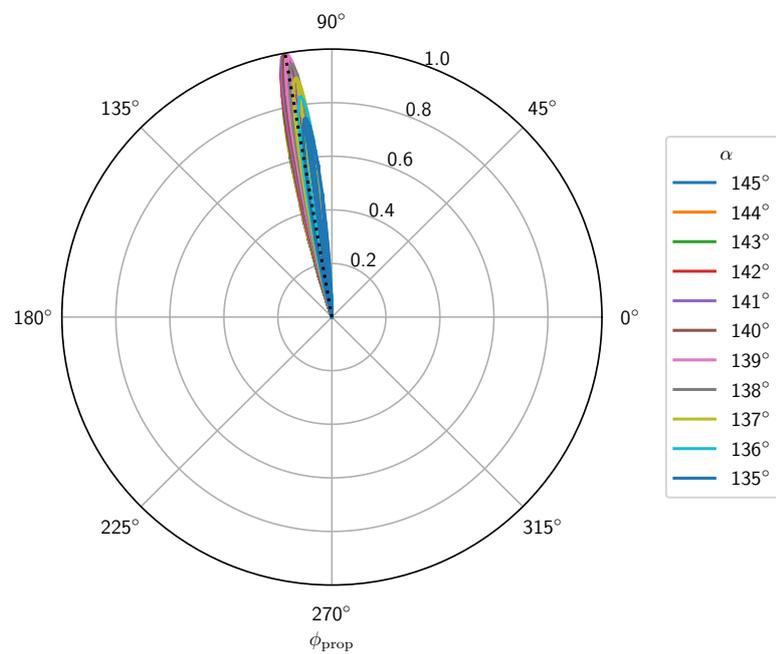
Figure 6.5: Polar plot of the Poynting vector for varying propagation angles ϕ_{prop} and angle between wavevectors α. Dotted line at $\phi_{\mathrm{prop}} = 260°$ $(-)$ or $\phi_{\mathrm{prop}} = 100°$ $(+)$. Normalized by maximum value.

Figure 6.6 shows that the peak photoelastically scattered power was maximized at an angle $\alpha = 40°$ for $(-)$ scattering (negative frequency shift) and at $\alpha = 140°$ for $(+)$ scattering (positive frequency shift). This shows that the angle α which maximizes the peak value of the Poynting vector magnitude also maximizes the total photoelastically scattered power. The analytical cases have their peaks close to these as well, but there is a shift in the angle α for the parallelogram curve. This shift is down in α for the $(-)$ case and up for the $(+)$ case, so it directly follows the shift observed in figure 6.3 and explained in section 4.2.1.

The peaks of the total scattering power for simulation, cuboid and parallelogram cases are well within 10 dB of each other, so in the same order of magnitude. As explained before, the geometry parameters in the analytical models could be selected with more care which might improve analytical results. One clear difference between simulated and analytical curves is that the analytical ones drop much faster than the simulated when moving away from the peak. This can be explained by the difference between plane and cylindrical waves. As explained earlier, cylindrical waves can be decomposed as a sum of plane waves with different propagation directions giving pairs of matched plane wave components at more than one angle α. The higher scattering power away from the peak in the simulated case could then simply be due to scattering of these other pairs of matched components.

Figure 6.7 shows the same simulation results as in figure 6.6, but without the analytical results. This makes it easier to compare $(+)$ and $(-)$ scattering. It can be seen that the $(+)$ and $(-)$ scattering result in very similar total scattered power levels. In absolute power, they are both close to -82.6 dBm . This can be compared with the input power of 15 dBm, which means that the photoelastically scattered power is 97.6 dB lower than the input electromagnetic power in these simulations.
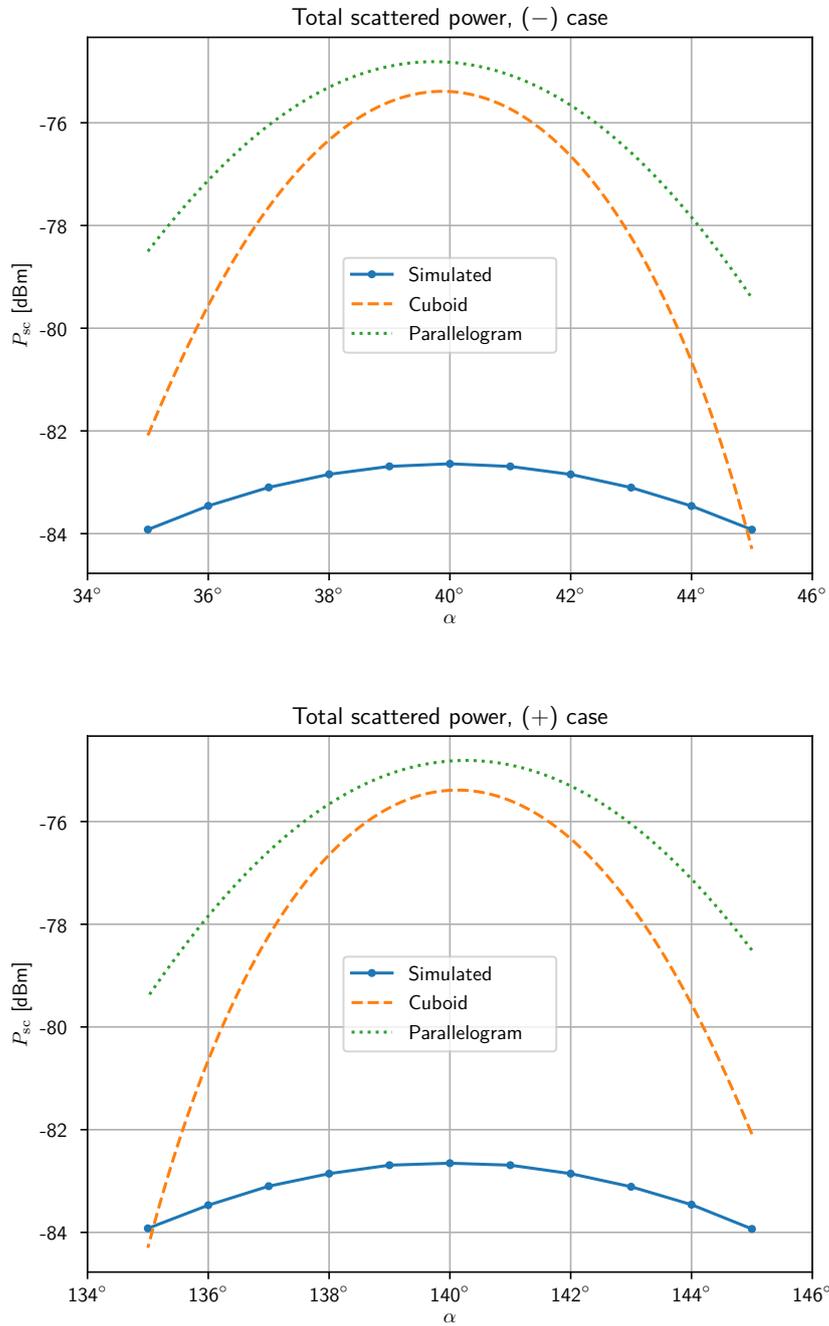
**Figure 6.6:** Total scattered power for different angles between wavevectors α. Analytical equivalents plotted for both cuboid and parallelogram geometries.
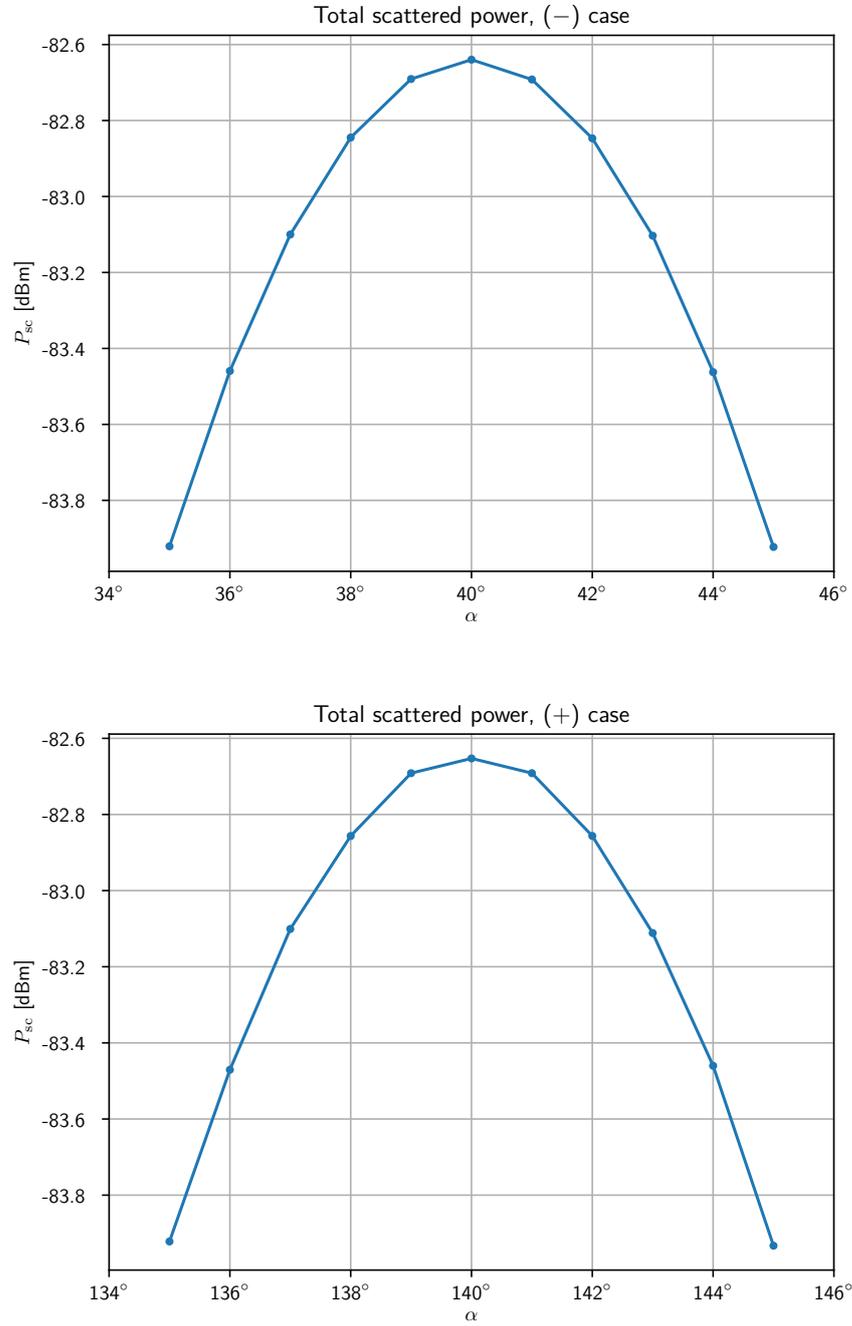
Figure 6.7: Total scattered power for different angles between wavevectors α.

6.1.2   Conductive Defect

The results from the sweep of defect conductivity is shown in figure 6.8 and 6.9. Figure 6.8 shows relevant plots for the entire domain: the incident electric field and Poynting vector. The incident pressure was the same as in figure 6.1. It is clear that the incident electric field is disturbed by the conductive defect, and the propagation direction is heavily affected after the defect.

Figure 6.9 shows the total scattered power (calculated in the same way as in the angle sweep) as a function of conductivity of the defect. It can be seen that the scattered power decreases as the conductivity of the defect increases. As conductivity increases, scattered power decreases. The rate of decrease is larger at small conductivities, and the scattered power level seems to plateau at higher levels.
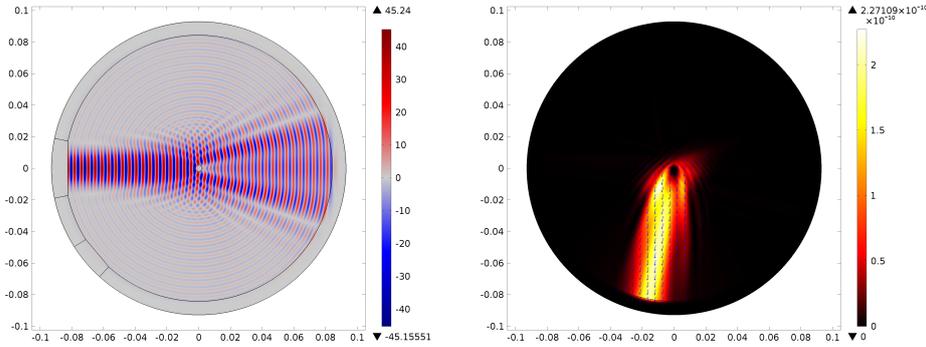
Figure 6.8:   Results of a 10 S/m conductive defect for entire domain. Left: incident electric field [V/m]. Right: Photoelastically scattered Poynting vector [W/m^2]

The reasons behind the decrease in scattered power can be explained by comparing the electric field for a 10 S/m defect in figure 6.8 with the corresponding field for no defect in figure 6.1. The field is affected by conductivity in two ways: first, the field is pushed out of the defect as conductivity increases. Second, the field is also scattered against the defect which causes the electromagnetic beam to drastically change in appearance when compared to a defect-free case. One crucial effect is the altered propagation directions of the beam after the defect. This directly influences the Bragg condition, and then also the photoelastic scattering.

As figure 6.9 shows, there is a plateauing effect in that the decrease in power is not as large at high conductivities as it is at lower conductivities. This can be explained by the electric field being pushed out of the defect region. As the field is pushed out, the defect behaves increasingly as a PEC sphere. As such, the total scattering power also approaches the level obtained when the defect is a PEC sphere, and cannot decrease any further than this.
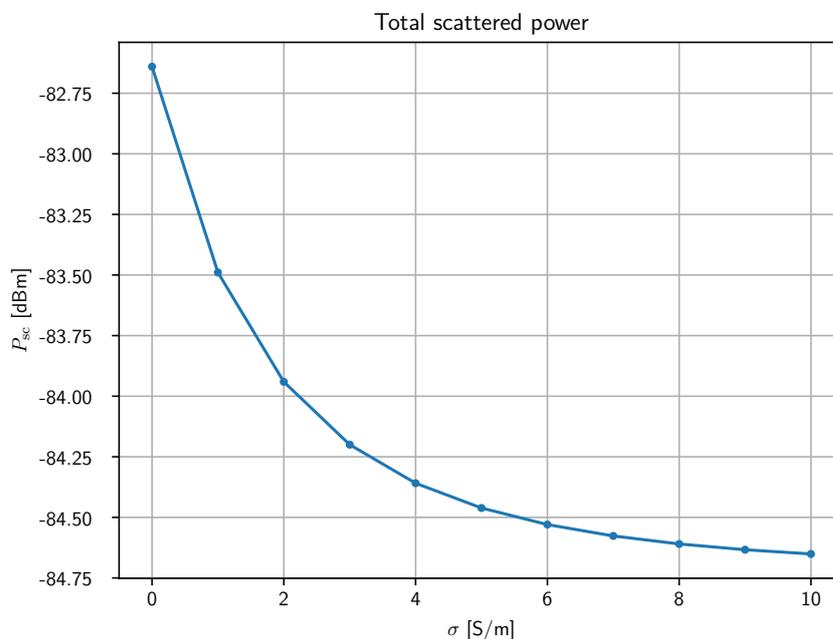
Figure 6.9: Poynting vector magnitude integrated over measurement boundary for different conductivity σ of defect. Normalized by maximum value.

6.1.3 Mechanical Defect

The results of the sweep of defect density is shown in figure 6.10-6.12. Figure 6.10 and 6.11 show relevant plots for the entire domain: the incident pressure and Poynting vector, and for the two densities 100 and 400 kg/m^3. The incident electric field was the same as in figure 6.1. It is clear that the pressure is disturbed by the defect, and the propagation direction is heavily affected after the defect. This is the case for both densities, but the exact wave patterns are different.

Figure 6.12 shows the total scattered power (calculated in the same way as in the angle sweep) as a function of density of the defect. For reference, the rest of the domain had the density $\rho_0 = 250$ kg/m^3. It can be seen that the scattered power is affected by a change in density in the defect area. At defect densities far away from the background density 250 kg/m^3 the effect is a decrease in scattered power.

One interesting detail is that the maximum of the scattered power is not obtained at a defect density of 250 kg/m^3, but instead slightly higher at 275 kg/m^3. This can be understood by observing the pressure from COMSOL in figure 6.11. Here the main lobe of pressure after the defect shows a high pressure right after the defect if compared with the defect-free case in figure 6.1. In this case the effect of the defect is large enough for clear nodal lines to appear, but at densities just
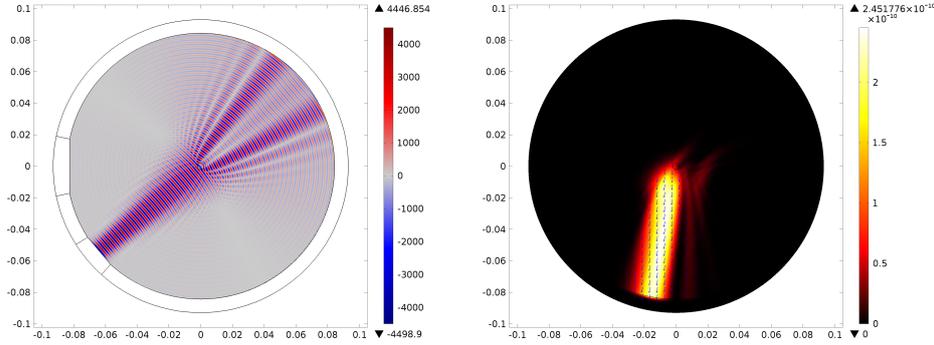
Figure 6.10:   Results of a 100 kg/m^3 defect for entire domain. Left: incident pressure [V/m]. Right: Photoelastically scattered Poynting vector [W/m^2]
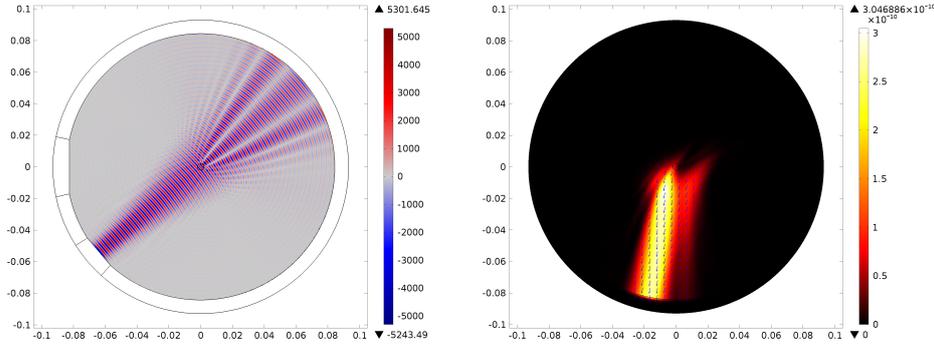

Figure 6.11:   Results of a 400 kg/m^3 defect for entire domain. Left: incident pressure [V/m]. Right: Photoelastically scattered Poynting vector [W/m^2]

slightly higher than the background, the effect is that the acoustic beam is focused after the defect without nodal lines appearing. This can be understood by viewing the defect as an acoustic lens. In geometrical optics, a lens is typically a region with higher refractive index than its surroundings bounded by spherical surfaces [25]. A higher refractive index in optics corresponds to a lower wave speed. In acoustics, the wave speed is defined as $v = \sqrt{K/\rho_0}$, so an increase in density while the bulk modulus is kept constant (as in this study) has the effect of lowering wave speed. The properties of the circular defect with a higher density than the background should then give it some lens properties. A significant difference between typical lenses and the case here is that the lens size is usually much larger than the wavelength, while they are in the same order of magnitude here. This case is very far from geometrical optics, and the physics required to explain focusing is vastly different [58].

The lensing effect increases the scattered power for a small increase in defect density as the beam spread is counteracted. However, for even higher defect densi-
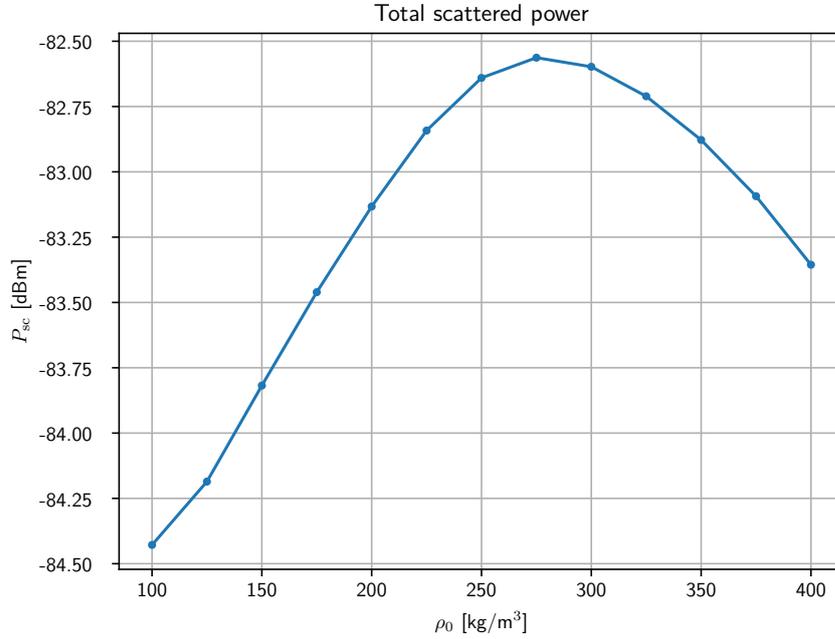
Figure 6.12: Poynting vector magnitude integrated over measurement boundary for different density ρ_0 of defect. Normalized by maximum value.

ties other effects instead cause a decrease in scattered power. A diffraction pattern appears behind the defect where regions of the wave with different propagation direction are separated by nodal lines as seen in figure 6.11.

One thing to note is that the increase in scattered power from this lensing phenomenon is not very large as the power at background density is less than 0.1 dB below the peak power. Additionally, this effect is highly dependent on geometry as the circular shape of the defect causes the increase in power. This effect should probably not be expected in general, but since it can exist for some geometries it is good to be aware of.

6.2 Possibilities for NDT

From the simulations with defects it was clear that defects with both electric and acoustic contrast had an effect on the photoelastic scattering. This indicates that an acousto-electromagnetic system utilizing photoelastic interaction at least has the ability to detect the presence of defects with either of those properties. This ability alone does not tell much about the possible performance of a future system. A good guideline is that an NDT system using both acoustic and electromagnetic waves (e.g. ultrasound and mm-waves) should be at least as good as a system using

only one of the phenomena. An acousto-electromagnetic system would probably be more complicated and expensive than an ultrasonic testing or a mm-wave imaging system, so in order to be useful it would have to offer better performance using some metric.

One possible way an acousto-electromagnetic system might outperform acoustic or electromagnetic systems is due to its ability to detect both electric and acoustic contrast. Directly, it allows for detection of more types of defects than existing systems by themselves. However, the possibility of different types of contrast leading to combined effects might be even more promising. The main mechanism allowing detection using photoelastic interaction was determined to be defects disrupting the incident beams, in turn leading to less advantageous conditions for the interaction. If a defect has both electric and acoustic contrast, the effect would be disruption of both the electromagnetic and acoustic beams. This should lead to a larger effect on the photoelastically scattered field than for just one mode of contrast. Due to this combination effect, it might be possible to detect a region with weak acoustic and electric contrasts with the same performance as a strong single contrast. If this is possible for acoustic and electric contrasts which are weak enough, an acousto-electromagnetic system might outperform a system using only one phenomenon for this type of defects. However, the photoelastic scattering against a combination of contrasts was not simulated in this work.

A possible issue with photoelastic interaction in NDT is related to resolution. One crucial factor affecting the interaction strength is the size of the interaction region. To obtain a high photoelastically scattered power, this region should be as large as possible. On the other hand, the possible resolution of the system should decrease with large interaction regions. One of the advantages of mm-wave imaging is that it provides high resolution, and it would be desirable to keep this for a combined mm-wave/ultrasound system. One interesting detail related to the resolution is that a small defect inside of a large interaction region mostly affects the interaction behind it. The reason for this is that diffraction effects in the shadow of the defect affect the propagation directions of waves, and thus the Bragg condition. The location of a defect inside of the interaction region should thus affect the strength of the photoelastic interaction, where a defect closer to the wave sources in the interaction region results in lower photoelastic scattering. There might be a way of utilizing this for improved resolution, but since no actual NDT system has been proposed in this work it is difficult to draw any conclusions.

In the beginning of chapter 3, an interaction mechanism utilizing localized harmonic motion was described as used in the experimental HMMDI medical imaging method. This was identified as an interesting subject, but not explored further due to time constraints. The possible issues with resolution for photoelastic interaction might not be present for this other type of interaction due to dissimilar underlying mechanisms. In HMMDI the scatterer is not the acoustic wave in itself, but instead a vibrating region inside of a test object. This could be very small, but of course this size might affect the strength of interaction. Nevertheless, the mechanism utilizing localized harmonic motion needs to be investigated for a good picture of the possibilities for acousto-electromagnetic interaction in NDT.

6.3   Future experiments

The next logical step after analytical modeling and numerical simulations is experimental testing to compare with the analytical and numerical results. Two important interaction properties to measure are the Bragg condition for incident/scattering angles (equations (4.3), (4.5) and (4.4)) and the frequency shift of scattered waves. The other important property to measure would be the received scattering power. However, measurement of the Bragg condition and frequency shift should be more robust to variation in the test environment than the received power. Bragg condition and frequency shift measurements could then be important for verifying the analytical and/or simulation results. Specific measurement values for received power might be useful for understanding the order of magnitude of the interaction strength. However, comparison of received power at different angles, frequencies etc. should be more interesting when comparing experiments with analytical and simulation results.

Some parts in the analytical models and numerical simulations can be identified at this stage to be less certain than others. One in particular, the photoelastic model is important to test experimentally since the model itself could not be verified in COMSOL. The coupling between acoustic pressure and relative permittivity was done entirely using equations (3.4) and (3.5), which were admittedly very simplified when compared to the full tensor model. Thorough experimentation would give more insight to how accurate the simple model used here really is, and where its main drawbacks might lie. Some points worth looking into are the assumption of isotropy in the photoelastic tensor, the assumption of $p_{11} = p_{12}$ in the isotropic photoelastic tensor and the model for the photoelastic constant in equation (3.5). All of these have connections to each other, so experiments should be designed with this in mind.

A part which might be lacking in the analytical models and numerical simulations is that of ultrasonic wave propagation. Most of the analytical modeling was based on pure p-wave propagation, which might not be the case in reality. If also a more complicated photoelastic model is required, using a photoelastic tensor instead of the simplified photoelastic constant in equation (3.4), s-waves would affect the interaction in a way not modeled analytically. Numerical simulations were even more simplistic when it came to ultrasonic wave propagation, assuming a negligible shear modulus. The result of this is that the wave speed equation is equal to that in acoustics, which was used to model phenomena in the COMSOL pressure acoustics interface. However, for a non-negligible shear modulus the true p-wave speed is higher than that given by acoustics. This needs to be taken into account when calculating angles and wavelengths for fulfilling the Bragg condition in real materials.

Two proposals for sample materials to use in experiments are air and a composite foam core. Experiments with air as the sample would probably be the simplest to set up using an air-coupled ultrasonic transducer and standard gain horn for micro/mm-waves. The coupling of waves into the sample would be trivial, and the sample would not need any preparation. A room with enough empty space would suffice. Cheap air-coupled transducers are readily available for use as cheap sensors for many consumer applications. These usually operate at 40 kHz, which

would put the wavelength at $\Lambda = 8.5$ mm (for $v = 340$ m/s). The Bragg condition puts the maximum electromagnetic wavelength at $\lambda = 2\Lambda$ (for $\alpha = 0°$), which corresponds to a minimum frequency of 17.6 GHz, so in the microwave range.

To obtain an estimate of the power levels required for this kind of experiment, the analytical model from section 4.2 was used. More specifically, the radar equation for SNR (4.2) was used together with a cross-section for a refined interaction region from equation (4.6). The parameters inserted in these equations were estimated from various sources. For the ultrasonic transducer, a 40 kHz SensorComp 40KPT25 was considered. This has a circular aperture with diameter 25.1 mm, beam angle 23° and a sound pressure level of 110 dB at a range of 30 cm from the transducer [59]. The microwave antennas were assumed to have equal gains of 20 dB at 24 GHz. The beam angle θ was calculated in radians using the gain G as $\theta = 4/G$ [57]. The aperture length D (assuming a square gain horn) was calculated using effective area as $D = \sqrt{G\lambda^2/4\pi}$ [57]. At the frequencies of 40 kHz and 24 GHz in air, the Bragg angle is approximately 41°. The relevant properties of dry air were $\rho_0 = 1.293$ kg/m^3, $v = 331.1$ m/s [45] and $\varepsilon_{\mathrm{r}} = 1.00059$ [53]. The bulk modulus was calculated using $K = \rho_0 v^2$. The range from antenna to the interaction region was assumed to be equal to the reference range 30 cm of the ultrasonic transducer. The beam diameters at this range were calculated by assuming diameters equal to the apertures at first, with a spread given by the beam angles further from the apertures. The receiver was assumed to have a noise figure of $F = 5$ dB with a bandwidth equal to the acoustic frequency at 40 kHz. The bandwidth is necessarily small since it is important to filter out the frequency shifted signal from the original. Using these parameters and the equations listed before, the transmitted electromagnetic power required for a received SNR of 0 dB using one received sample was calculated to be -4.7 dBm. This can be compared to -7 dBm used in mm-wave imaging experiments at the Department of Electrical and Information Technology, Lund University [10]. Looking at the results in figure 6.6, the simulation results had scattered power levels below that of the analytical models. It would therefore be reasonable to expect higher power requirements in experiments than -4.7 dBm. The range between antenna and interaction region might also have to be larger than 30 cm, which would increase the power requirements further. Nevertheless, the calculated -4.7 dBm is not a very high power and was calculated for only one sample at the receiver. With coherent integration using multiple samples there should be enough margin to be able to perform experiments without power being an issue.

Experiments with a composite core as the sample would be more difficult due to the requirements on the ultrasonic side. The low permittivity of the core means that no special coupling would be required for micro/mm-waves. However, coupling of ultrasound into a solid would require a transducer made for this type of coupling. To the knowledge of the author, this requires transducers made for more advanced purposes such as medical imaging or NDT. Aerospace composite cores might be difficult to obtain since they are not consumer products. In simulations, the foam core was from Diab AB's Divinycell HT product range. Divinycell H is another product range which is not aerospace graded, but still has fairly similar properties [60]. The benefit of this is that it is used in leisure marine applications and can be readily found in marine equipment stores, along with many other

similar core materials.

6.4   Summary and Conclusions

To connect back to the introduction of the thesis, the three main questions describing the purpose of the work are restated

1. How does acousto-electromagnetic interaction differ from acousto-optic theory with wavelengths in the same order of magnitude?

2. What properties do acoustic and electromagnetic waves have in homogeneous materials and laminated composites?

3. How can ultrasound improve mm-wave imaging of defects in composites?

The first question is answered well in some respects, since the analytical model derived in this work did not have any conditions on the electromagnetic and acoustic wavelengths. One of the main results from acousto-optics is the Bragg condition. The analytical and simulated results in this work showed that this condition was at the very least a good approximation for the angles and wavevectors giving maximum scattering. The main difference analytically was a shift in the required angle between acoustic and electromagnetic beams for a parallelogram-based geometry. Simulations showed a very slight asymmetry eventually indicative of a shift, though very small. This work also presented radar equations describing total received power and SNR based on standard antenna parameters. These might be more useful than similar equations derived using optical parameters, even if their results only give an order of magnitude estimation. Of course, experiments are necessary to compare with both the analytical and simulated results.

The reason why this first question is only answered well in some respects is that there are other interaction mechanisms which were not as deeply investigated as the photoelastic interaction mechanism. In particular, the localized harmonic motion mechanism was identified as worth investigating but ended up being in the shadow of photoelastic interaction in this work. One reason was the difficulty of modeling acoustic radiation force as well as time constraints.

The second question is only partly answered since laminated composites were not considered to any greater extent. Properties of both types of waves were required in the derivation of analytical models as well as for setting correct parameters for simulations. Properties of acoustic waves were examined in detail since they are highly different in fluids and solids. Unfortunately, simulations could only be run for acoustic waves in fluids, which limited possibilities of the investigations. However, due to the similarity of p-waves and acoustic waves in fluids, part of the problem in a solid could be simulated in a reasonable way.

The third question was discussed previously in this chapter. One main way photoelastic interaction might be useful for improving NDT of composites is by allowing detection of both acoustic and electric contrast. However, it has not been discussed how a mm-wave imaging system might be improved using photoelastic interaction with ultrasound. Models presented in this work were entirely based on two crossing beams, which might be difficult to integrate with mm-wave imaging. A possible issue with photoelastic interaction was discussed as good interaction

strength might be detrimental to resolution in a system. It might also be the case that photoelastic interaction is not the most effective way of combining mm-waves and ultrasound. Further investigation of localized harmonic motion should be undertaken to understand the possibilities better.

Future Work

One issue which became apparent was related to the assumption of plane waves in analytical models. This was discussed as being a possible reason for discrepancies between simulated and analytical values. An idea for improving analytical results is to utilize the fact that all waves can be decomposed into a sum of plane waves with varying propagation directions. Using the same equations as before, it might be possible to use more realistic incident beams by decomposing them into plane waves before using the analytical equations.

More refined simulations would be interesting for future work. Some areas with room for improvement are modeling of the electromagnetic antenna and ultrasonic transducer, interfaces between wave sources and the test object, modeling of laminations around the composite core and modeling of elastodynamics instead of acoustics. Most of these require more information on the physics involved than what was used in this work. For use of COMSOL, most possible refinements in the acoustic area would benefit from the Acoustics Module and Structural Mechanics Module, although it would be possible to enter the required equations and boundary conditions manually with only the basic COMSOL distribution.

This work only considered homogeneous, isotropic materials with very simple defects if any. For better knowledge of possibilities in NDT, the material should be modeled in greater detail. In general, aerospace composites are laminated which adds one piece of complexity to the problem. Laminations might cause reflections of either the electromagnetic or acoustic wave, and for material dimensions on the order of magnitude as the wavelengths these might cause significant effects. Another issue might be anisotropy in core materials such as honeycombs. More information on real defect properties might also be needed to accurately model their influence

The bulk of this work was focused on acousto-electromagnetic interaction based in photoelasticity. This was however only one of interaction mechanisms found in the literature. While some mechanisms were discarded for use in NDT, the localized harmonic motion mechanism was a possible candidate for this application. To fully understand how ultrasound might be used in mm-wave imaging systems, this interaction mechanism needs to be studied more closely.

Lastly, experiments are necessary for comparison with analytical models and simulations. Especially the photoelastic model needs experimental investigation.

Bibliography

[1] P. K. Saha, *Aerospace Manufacturing Processes*, 1st ed. Boca Raton, FL: CRC Press, 2016.

[2] The International Committee for Non-Destructive Testing, "What is NDT?" *The International Committee for Non-Destructive Testing*, 2006. [Online]. Available: http://www.icndt.org/What-is-NDT

[3] C. Garnier, M.-L. Pastor, F. Eyma, and B. Lorrain, "The detection of aeronautical defects in situ on composite structures using non destructive testing," *Composite Structures*, vol. 93, no. 5, pp. 1328 – 1336, 2011.

[4] A. Katunin, K. Dragan, and M. Dziendzikowski, "Damage identification in aircraft composite structures: A case study using various non-destructive testing techniques," *Composite Structures*, vol. 127, pp. 1 – 9, 2015.

[5] S. Gholizadeh, "A review of non-destructive testing methods of composite materials," *Procedia Structural Integrity*, vol. 1, pp. 50 – 57, 2016, XV Portuguese Conference on Fracture, PCF 2016, 10-12 February 2016, Paco de Arcos, Portugal.

[6] L. W. Schmerr, *Fundamentals of Ultrasonic Nondestructive Evaluation*, 2nd ed., ser. Springer Series in Measurement Science and Technology. Springer International Publishing, 2016.

[7] G. Riegert, K. Pfleiderer, H. Gerhard, I. Solodov, and G. Busse, "Modern methods of NDT for inspection of aerospace structures," *ECNDT, Berlin, Germany*, 2006. [Online]. Available: http://www.ndt.net/?id=3560

[8] S. Kharkovsky and R. Zoughi, "Microwave and millimeter wave nondestructive testing and evaluation - overview and recent advances," *IEEE Instrumentation Measurement Magazine*, vol. 10, no. 2, pp. 26–38, April 2007.

[9] G. Dobmann, I. Altpeter, C. Sklarczyk, and R. Pinchuk, "Non-destructive testing with micro- and mm-waves — where we are — where we go," *Welding in the World*, vol. 56, no. 1, pp. 111–120, Jan 2012.

[10] J. Helander, A. Ericsson, M. Gustafsson, T. Martin, D. Sjöberg, and C. Larsson, "Compressive sensing techniques for mm-wave nondestructive testing of composite panels," *IEEE Transactions on Antennas and Propagation*, vol. 65, no. 10, pp. 5523–5531, Oct. 2017.

[11] M. A. Abou-Khousa, A. Ryley, S. Kharkovsky, R. Zoughi, D. Daniels, N. Kreitinger, and G. Steffes, "Comparison of xray, millimeter wave, shearography and throughtransmission ultrasonic methods for inspection of honeycomb composites," *AIP Conference Proceedings*, vol. 894, no. 1, pp. 999–1006, 2007.

[12] M. Fink, "Multiwave imaging and super resolution," *Physics Today*, vol. 63, no. 2, p. 28, Feb. 2010.

[13] M. Fatemi and J. F. Greenleaf, "Ultrasound-stimulated vibro-acoustic spectrography," *Science*, vol. 280, no. 5360, pp. 82–85, 1998.

[14] F. G. Mitri, G. T. Silva, J. F. Greenleaf, and M. Fatemi, "Simultaneous sum-frequency and vibro-acoustography imaging for nondestructive evaluation and testing applications," *Journal of Applied Physics*, vol. 102, no. 11, p. 114911, 2007.

[15] A. M. Buerkle, "Modeling and applications of acoustic and electromagnetic wave interaction," PhD Thesis, University of Michigan, 2007. [Online]. Available: http://www.eecs.umich.edu/radlab/html/NEWDISS/Buerkle.pdf

[16] A. Buerkle and K. Sarabandi, "Non-destructive evaluation of elastic targets using acousto-electromagnetic wave interaction and time reversal focusing," *IEEE Transactions on Antennas and Propagation*, vol. 57, no. 11, pp. 3628–3637, Nov. 2009.

[17] H. Merkel, "Apparatus for determining physical parameters in an object using simultaneous microwave and ultrasound radiation and measurement," SE patentus US 7,040,168 B1, May 9, 2006. [Online]. Available: https://patents.google.com/patent/US7040168B1/en

[18] A. Korpel, "Acousto-optics—a review of fundamentals," *Proceedings of the IEEE*, vol. 69, no. 1, pp. 48–53, Jan 1981.

[19] J. M. Marshall, A. M. Peterson, and A. A. Barnes, "Combined radar-acoustic sounding system," *Applied Optics*, vol. 11, no. 1, pp. 108–112, Jan 1972.

[20] P. T. May, R. G. Strauch, K. P. Moran, and W. L. Ecklund, "Temperature sounding by rass with wind profiler radars: a preliminary study," *IEEE Transactions on Geoscience and Remote Sensing*, vol. 28, no. 1, pp. 19–28, Jan 1990.

[21] D. T. Gjessing, R. Hansen, and J. Saebboe, "Characterisation of wind field with high resolution in time and space by the use of electromagnetic and acoustic waves," *IEE Proceedings - Radar, Sonar and Navigation*, vol. 148, no. 2, pp. 49–55, April 2001.

[22] W. R. Scott and J. S. Martin, "Experimental investigation of the acousto-electromagnetic sensor for locating land mines," *Proc.SPIE*, vol. 3710, pp. 204 – 214, 1999.

[23] C. B. Top, A. K. Tafreshi, and N. G. Gençer, "Microwave sensing of acoustically induced local harmonic motion: Experimental and simulation studies on breast tumor detection," *IEEE Transactions on Microwave Theory and Techniques*, vol. 64, no. 11, pp. 3974–3986, Nov 2016.

[24] D. S. Elson, R. Li, C. Dunsby, R. Eckersley, and M.-X. Tang, "Ultrasound-mediated optical tomography: a review of current methods," *Interface Focus*, vol. 1, no. 4, pp. 632–648, 2011.

[25] B. E. A. Saleh and M. C. Teich, *Acousto-Optics*, 2nd ed., ser. Fundamentals of Photonics. Hoboken, New Jersey: John Wiley & Sons, Inc., 2007, ch. 19, pp. 804–833.

[26] A. Korpel, *Acousto-optics*, 1st ed., ser. Optical engineering, 16. New York: Marcel Dekker Inc, 1988.

[27] A. Tonning, "Scattering of electromagnetic waves by an acoustic disturbance in the atmosphere," *Applied Scientific Research, Section B*, vol. 6, no. 1, pp. 401–421, Dec 1957.

[28] A. S. Gurvich, A. I. Kon, and V. I. Tatarskii, "Scattering of electromagnetic waves on sound in connection with problems of atmospheric sounding (review)," *Radiophysics and Quantum Electronics*, vol. 30, no. 4, pp. 347–366, Apr 1987.

[29] V. I. Tatarskii, *The effects of the turbulent atmosphere on wave propagation*. Jerusalem: Israel Program for Scientific Translations, 1971. [Online]. Available: https://ui.adsabs.harvard.edu/#abs/1971etaw.book.....T

[30] D. E. Lawrence and K. Sarabandi, "Acoustic and electromagnetic wave interaction: analytical formulation for acousto-electromagnetic scattering behavior of a dielectric cylinder," *IEEE Transactions on Antennas and Propagation*, vol. 49, no. 10, pp. 1382–1392, Oct. 2001.

[31] A. Buerkle and K. Sarabandi, "Analysis of acousto-electromagnetic wave interaction using the finite-difference time-domain method," *IEEE Transactions on Antennas and Propagation*, vol. 56, no. 8, pp. 2191–2199, Aug. 2008.

[32] L. Wang, "Acoustic radiation force based ultrasound elasticity imaging for biomedical applications," *Sensors (Basel, Switzerland)*, vol. 18, no. 7, 2018.

[33] C. B. Top and N. G. Gençer, "Harmonic motion microwave doppler imaging: A simulation study using a simple breast model," *IEEE Transactions on Medical Imaging*, vol. 33, no. 2, pp. 290–300, Feb 2014.

[34] A. K. Tafreshi, C. B. Top, and N. G. Gençer, "Two-dimensional multi-frequency imaging of a tumor inclusion in a homogeneous breast phantom using the harmonic motion doppler imaging method," *Physics in Medicine & Biology*, vol. 62, no. 12, p. 4852, 2017.

[35] K. K. Chawla, *Composite Materials: Science and Engineering*, 3rd ed. New York: Springer, 2012.

[36] L. Carlsson and G. Kardomateas, *Structural and Failure Mechanics of Sandwich Composites*, ser. Solid Mechanics and Its Applications. Dordrecht: Springer, 2011.

[37] K. Sarabandi and D. E. Lawrence, "Acoustic and electromagnetic wave interaction: estimation of doppler spectrum from an acoustically vibrated metallic circular cylinder," *IEEE Transactions on Antennas and Propagation*, vol. 51, no. 7, pp. 1499–1507, July 2003.

[38] E. E. Konofagou and K. Hynynen, "Localized harmonic motion imaging: theory, simulations and experiments," *Ultrasound in Medicine & Biology*, vol. 29, no. 10, pp. 1405 – 1413, 2003.

[39] V. C. Chen, F. Li, S. . Ho, and H. Wechsler, "Micro-doppler effect in radar: phenomenon, model, and simulation study," *IEEE Transactions on Aerospace and Electronic Systems*, vol. 42, no. 1, pp. 2–21, Jan 2006.

[40] G. R. Torr, "The acoustic radiation force," *American Journal of Physics*, vol. 52, no. 5, pp. 402–408, 1984.

[41] C. P. Lee and T. G. Wang, "Acoustic radiation pressure," *The Journal of the Acoustical Society of America*, vol. 94, no. 2, pp. 1099–1109, 1993.

[42] T. Hasegawa, T. Kido, T. Iizuka, and C. Matsuoka, "A general theory of Rayleigh and Langevin radiation pressures," *Acoustical Science and Technology*, vol. 21, no. 3, pp. 145–152, 2000.

[43] K. Nightingale, M. S. Soo, R. Nightingale, and G. Trahey, "Acoustic radiation force impulse imaging: in vivo demonstration of clinical feasibility," *Ultrasound in Medicine & Biology*, vol. 28, no. 2, pp. 227 – 235, 2002.

[44] W. Leutz and G. Maret, "Ultrasonic modulation of multiply scattered light," *Physica B: Condensed Matter*, vol. 204, no. 1, pp. 14 – 19, 1995.

[45] T. Rossing, Ed., *Springer Handbook of Acoustics*, 2nd ed. Springer-Verlag, 2014.

[46] A. A. Kaufman and A. L. Levshin, *Acoustic and Elastic Wave Fields in Geophysics, I*, ser. Methods in Geochemistry and Geophysics. Elsevier, 2000. [Online]. Available: https://www.sciencedirect.com/bookseries/methods-in-geochemistry-and-geophysics/vol/32

[47] F. Jacobsen, "A note on instantaneous and time-averaged active and reactive sound intensity," *Journal of Sound and Vibration*, vol. 147, no. 3, pp. 489 – 496, 1991.

[48] A. A. Kaufman and A. L. Levshin, *Acoustic and Elastic Wave Fields in Geophysics, III*, ser. Methods in Geochemistry and Geophysics. Elsevier, 2005. [Online]. Available: https://www.sciencedirect.com/bookseries/methods-in-geochemistry-and-geophysics/vol/39

[49] F. Irgens, *Continuum Mechanics*. Berlin, Heidelberg: Springer, 2008.

[50] A. Bertram and R. Glüge, *Solid Mechanics: Theory, Modeling, and Problems*. Switzerland: Springer, 2015.

[51] D. F. Nelson and M. Lax, "Theory of the photoelastic interaction," *Physical Review B*, vol. 3, pp. 2778–2794, Apr 1971.

[52] V. O. Rapoport, N. A. Mityakov, V. A. Zinichev, and N. I. Belova, "The role of atmospheric temperature gradients and winds for estimating the energy potential of radio-acoustic sounding systems," *Radiophysics and Quantum Electronics*, vol. 40, no. 5, pp. 408–413, May 1997.

[53] L. G. Hector and H. L. Schultz, "The dielectric constant of air at radiofrequencies," *Physics*, vol. 7, no. 4, pp. 133–136, 1936.

[54] M. A. Richards, J. A. Scheer, and W. A. Holm, Eds., *Principles Of Modern Radar*. SciTech Publishing, Inc., 2012, vol. 1: Basic Principles.

[55] S. J. Straub, L. D. Johns, and S. M. Howard, "Variability in effective radiating area at 1 MHz affects ultrasound treatment intensity," *Physical Therapy*, vol. 88, no. 1, pp. 50–57, 2008.

[56] *Divinycell HT*, Diab Group, Laholm, Sweden, Feb. 2016, rev. 13. [Online]. Available: http://www.diabgroup.com/~/media/Files/Products/Core-material-products-English/HT%20February%202016%20rev13%20SI.pdf

[57] S. J. Orfanidis, *Electromagnetic Waves and Antennas*. Rutgers University, 2016. [Online]. Available: http://eceweb1.rutgers.edu/~orfanidi/ewa/

[58] D. A. Fletcher, K. E. Goodson, and G. S. Kino, "Focusing in microlenses close to a wavelength in diameter," *Opt. Lett.*, vol. 26, no. 7, pp. 399–401, Apr 2001.

[59] *K Series 40KPT25 Specifications*, SensComp Inc., Livonia, MI, USA, 2013. [Online]. Available: http://www.senscomp.com/pdfs/K-Series-40KPT25-Ultrasonic-Sensor-Spec.pdf

[60] *Divinycell H*, Diab Group, Laholm, Sweden, Jul. 2018, rev. 18. [Online]. Available: http://www.diabgroup.com/~/media/Files/Products/Core-material-products-English/H%20July%202018%20rev18%20SI.pdf

[61] G. Kristensson, *Spridningsteori med Antenntillämpningar*. Gerhard Kristensson, 2008. [Online]. Available: https://www.eit.lth.se/fileadmin/eit/home/scd.gkr/Books/Spridning.pdf

[62] B. Engquist and H. Zhao, "Approximate separability of the Green's function of the Helmholtz equation in the high frequency limit," *Communications on Pure and Applied Mathematics*, vol. 71, no. 11, pp. 2220–2274, 2018.

[63] D. J. Griffiths, *Introduction to Electrodynamics*, 4th ed. Essex: Pearson Education Limited, 2014.

[64] P. H. Young, *Electronic Communication Techniques*, 5th ed. New Jersey: Pearson Education Inc., 2004.

[65] M. Abramowitz and I. A. Stegun, Eds., *Handbook of Mathematical Functions with Formulas, Graphs, and Mathematical Tables*. National Bureau of Standards, 1964.

Full Derivations

A.1 Derivation of scattering integral for perturbed dielectrics

Here follows a formal derivation of the scattering of electromagnetic waves against a perturbation in relative permittivity. This is useful in photoelastic interaction since an acoustic wave in that case causes a periodic dielectric perturbation. Most of this derivation is based on a similar derivation by Tatarskii which considers scattering from turbulence in air [29].

A.1.1 General equation for electric field in perturbated dielectric

First, Maxwell's equations for a linear, non-magnetic, source-free, isotropic dielectric are presented. Note that the permittivity is not homogeneous.

$$\nabla \times \boldsymbol{\mathcal{E}} = -\mu_0 \frac{\partial \boldsymbol{\mathcal{H}}}{\partial t}$$

$$\nabla \times \boldsymbol{\mathcal{H}} = \frac{\partial(\varepsilon \boldsymbol{\mathcal{E}})}{\partial t}$$

$$\nabla \cdot (\varepsilon \boldsymbol{\mathcal{E}}) = 0$$

$$\nabla \cdot \boldsymbol{\mathcal{H}} = 0$$

The script letters are used here to indicate a time dependence as

$$\boldsymbol{\mathcal{E}}(\boldsymbol{r}, t) = \boldsymbol{E}(\boldsymbol{r}, t) \mathrm{e}^{-\mathrm{i}\omega t}$$

$$\boldsymbol{\mathcal{H}}(\boldsymbol{r}, t) = \boldsymbol{H}(\boldsymbol{r}, t) \mathrm{e}^{-\mathrm{i}\omega t}$$

This is used to remove the $\mathrm{e}^{-i\omega t}$ dependence in the equations and only keep time dependencies associated with other phenomena (such as the dielectric perturbation

here). The new equations are

$$\nabla \times \boldsymbol{E} = \mathrm{i}\omega\mu_0 \boldsymbol{H} - \mu_0 \frac{\partial \boldsymbol{H}}{\partial t} \tag{A.1}$$

$$\nabla \times \boldsymbol{H} = -\mathrm{i}\omega\varepsilon \boldsymbol{E} + \mu_0 \frac{\partial (\varepsilon \boldsymbol{E})}{\partial t} \tag{A.2}$$

$$\nabla \cdot (\varepsilon \boldsymbol{E}) = 0 \tag{A.3}$$

$$\nabla \cdot \boldsymbol{H} = 0 \tag{A.4}$$

Now $\nabla \times$ is applied to $\nabla \times \boldsymbol{E}$ and it is combined with $\nabla \times \boldsymbol{H}$, giving

$$\nabla \times (\nabla \times \boldsymbol{E}) = \omega^2 \mu_0 \varepsilon \boldsymbol{E} + 2\mathrm{i}\omega\mu_0 \frac{\partial (\varepsilon \boldsymbol{E})}{\partial t} - \mu_0 \frac{\partial^2 (\varepsilon \boldsymbol{E})}{\partial t^2}$$

The relation $\nabla \times (\nabla \times \boldsymbol{E}) = -\nabla^2 \boldsymbol{E} + \nabla(\nabla \cdot \boldsymbol{E})$ is now used

$$\nabla^2 \boldsymbol{E} + \omega^2 \mu_0 \varepsilon \boldsymbol{E} = \nabla(\nabla \cdot \boldsymbol{E}) - 2\mathrm{i}\omega\mu_0 \frac{\partial (\varepsilon \boldsymbol{E})}{\partial t} + \mu_0 \frac{\partial^2 (\varepsilon \boldsymbol{E})}{\partial t^2} \tag{A.5}$$

Gauss' law (A.3) is now expanded to $\varepsilon(\nabla \cdot \boldsymbol{E}) + (\nabla\varepsilon) \cdot \boldsymbol{E} = 0$. This can be rewritten as

$$\nabla \cdot \boldsymbol{E} = -\boldsymbol{E} \cdot \frac{\nabla\varepsilon}{\varepsilon} = -\boldsymbol{E} \cdot \nabla(\ln\varepsilon)$$

Inserting this into equation (A.5) gives

$$\nabla^2 \boldsymbol{E} + \omega^2 \mu_0 \varepsilon \boldsymbol{E} = -\nabla(\boldsymbol{E} \cdot \nabla(\ln\varepsilon)) - 2\mathrm{i}\omega\mu_0 \frac{\partial (\varepsilon \boldsymbol{E})}{\partial t} + \mu_0 \frac{\partial^2 (\varepsilon \boldsymbol{E})}{\partial t^2} \tag{A.6}$$

Now, the dielectric perturbation is defined as

$$\varepsilon = \varepsilon_0(\varepsilon_\mathrm{r} + \varepsilon_1) \tag{A.7}$$

where ε_0 is the permittivity of free space, ε_r is the unperturbed value for relative permittivity in the material and ε_1 is a small perturbation around ε_r. For $|\varepsilon_1| \ll \varepsilon_\mathrm{r}$ $\ln\varepsilon$ can be approximated as

$$\ln\varepsilon = \ln(\varepsilon_0\varepsilon_\mathrm{r}) + \ln(1 + \frac{\varepsilon_1}{\varepsilon_\mathrm{r}}) \approx \ln(\varepsilon_0\varepsilon_\mathrm{r}) + \frac{\varepsilon_1}{\varepsilon_\mathrm{r}}$$

Since $\ln(\varepsilon_0\varepsilon_\mathrm{r})$ is constant, the gradient can be written as

$$\nabla(\ln\varepsilon) = \nabla\left(\frac{\varepsilon_1}{\varepsilon_\mathrm{r}}\right) = \frac{1}{\varepsilon_\mathrm{r}}\nabla\varepsilon_1$$

This is now inserted in equation (A.6) together with equation (A.7), giving

$$\nabla^2 \boldsymbol{E} + \omega^2 \mu_0 \varepsilon_0 \varepsilon_\mathrm{r} \boldsymbol{E} = -\omega^2 \mu_0 \varepsilon_0 \varepsilon_1 \boldsymbol{E} - \frac{1}{\varepsilon_\mathrm{r}}\nabla(\boldsymbol{E} \cdot \nabla\varepsilon_1) - 2\mathrm{i}\omega\mu_0 \frac{\partial (\varepsilon \boldsymbol{E})}{\partial t} + \mu_0 \frac{\partial^2 (\varepsilon \boldsymbol{E})}{\partial t^2}$$

Now k is defined as $k = \omega/c$ where c is the speed of light in the material

$$c = \frac{1}{\sqrt{\mu_0\varepsilon_0\varepsilon_\mathrm{r}}} = \frac{c_0}{\sqrt{\varepsilon_\mathrm{r}}}$$

This is now used to obtain

$$\nabla^2 \boldsymbol{E} + k^2 \boldsymbol{E} = -k^2 \frac{\varepsilon_1}{\varepsilon_{\mathrm{r}}} \boldsymbol{E} - \frac{1}{\varepsilon_{\mathrm{r}}} \nabla(\boldsymbol{E} \cdot \nabla \varepsilon_1) - \frac{k^2}{\varepsilon_{\mathrm{r}}} \boldsymbol{E}_{\mathrm{d}}$$

where $\boldsymbol{E}_{\mathrm{d}}$ contains the time derivatives and is written as

$$\begin{aligned}
\boldsymbol{E}_{\mathrm{d}} &= \frac{2\mathrm{i}}{ck\varepsilon_0} \frac{\partial(\varepsilon \boldsymbol{E})}{\partial t} - \frac{1}{c^2 k^2 \varepsilon_0} \frac{\partial^2(\varepsilon \boldsymbol{E})}{\partial t^2} \\
&= \frac{2\mathrm{i}\varepsilon_{\mathrm{r}}}{\omega} \frac{\partial \boldsymbol{E}}{\partial t} + \frac{2\mathrm{i}}{\omega} \frac{\partial(\varepsilon_1 \boldsymbol{E})}{\partial t} - \frac{\varepsilon_{\mathrm{r}}}{\omega^2} \frac{\partial^2 \boldsymbol{E}}{\partial t^2} - \frac{1}{\omega^2} \frac{\partial^2(\varepsilon_1 \boldsymbol{E})}{\partial t^2}
\end{aligned}$$

A.1.2   Born approximation and solution

Now the electric field is split up into an incident field $\boldsymbol{E}_{\mathrm{i}}$ and a scattered field $\boldsymbol{E}_{\mathrm{sc}}$ such that $\boldsymbol{E} = \boldsymbol{E}_{\mathrm{i}} + \boldsymbol{E}_{\mathrm{sc}}$. The scattered field is considered to be small compared to the incident field (Born approximation). The incident field then approximately obeys the source-free equation

$$\nabla^2 \boldsymbol{E}_{\mathrm{i}} + k^2 \boldsymbol{E}_{\mathrm{i}} = 0$$

If this is subtracted from the total equation and $\boldsymbol{E}_{\mathrm{sc}}$ is neglected in the RHS the resulting equation is

$$\nabla^2 \boldsymbol{E}_{\mathrm{sc}} + k^2 \boldsymbol{E}_{\mathrm{sc}} = -k^2 \frac{\varepsilon_1}{\varepsilon_{\mathrm{r}}} \boldsymbol{E}_{\mathrm{i}} - \frac{1}{\varepsilon_{\mathrm{r}}} \nabla(\boldsymbol{E}_{\mathrm{i}} \cdot \nabla \varepsilon_1) - \frac{k^2}{\varepsilon_{\mathrm{r}}} \boldsymbol{E}_{\mathrm{di}}$$

This is an inhomogeneous Helmholtz equation which in three dimensions, and under a Sommerfeld radiation condition, has the solution [61, 62]

$$\begin{aligned}
\boldsymbol{E}_{\mathrm{sc}}(\boldsymbol{r}, t) = {}&\frac{1}{4\pi\varepsilon_{\mathrm{r}}} \int_{V_{\mathrm{sc}}} \frac{\mathrm{e}^{\mathrm{i}k|\boldsymbol{r}-\boldsymbol{r}'|}}{|\boldsymbol{r}-\boldsymbol{r}'|} \\
&\cdot \left(k^2 \varepsilon_1(\boldsymbol{r}', t) \boldsymbol{E}_{\mathrm{i}}(\boldsymbol{r}', t) + \nabla\left(\boldsymbol{E}_{\mathrm{i}}(\boldsymbol{r}', t) \cdot \nabla \varepsilon_1(\boldsymbol{r}', t)\right) + k^2 \boldsymbol{E}_{\mathrm{di}}(\boldsymbol{r}', t) \right) \mathrm{d}v'
\end{aligned}$$

where

$$\begin{aligned}
\boldsymbol{E}_{\mathrm{di}}(\boldsymbol{r}', t) = {}&\frac{2\mathrm{i}\varepsilon_{\mathrm{r}}}{\omega} \frac{\partial}{\partial t}\left(\boldsymbol{E}_{\mathrm{i}}(\boldsymbol{r}', t)\right) + \frac{2\mathrm{i}}{\omega} \frac{\partial}{\partial t}\left(\varepsilon_1(\boldsymbol{r}', t)\boldsymbol{E}_{\mathrm{i}}(\boldsymbol{r}', t)\right) \\
&- \frac{\varepsilon_{\mathrm{r}}}{\omega^2} \frac{\partial^2}{\partial t^2}\left(\boldsymbol{E}_{\mathrm{i}}(\boldsymbol{r}', t)\right) - \frac{1}{\omega^2} \frac{\partial^2}{\partial t^2}\left(\varepsilon_1(\boldsymbol{r}', t)\boldsymbol{E}_{\mathrm{i}}(\boldsymbol{r}', t)\right)
\end{aligned}$$

This equation provides the scattered electric field when using the Born approximation.

A.2   Derivation of radar equation for simple photoelasticity

The scattering integral derived in appendix A.1.2 is now solved for a simple geometry and material model to obtain a radar equation.
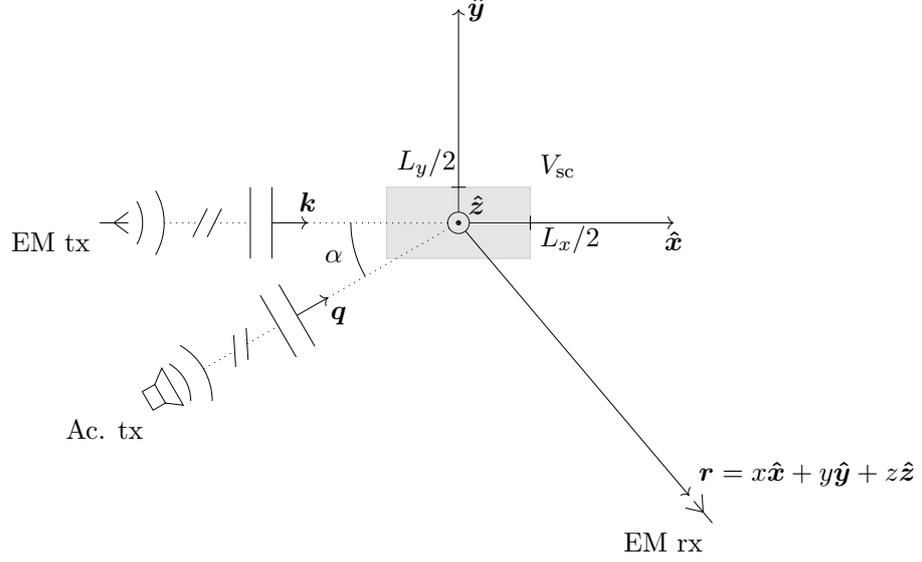
Figure A.1: Geometry for the scattering problem.

A.2.1 Geometry and solution of scattering integral

First, the geometry is defined as shown in figure A.1. The xy-plane is defined
as the plane formed by the acoustic and electromagnetic wavevectors (they are
assumed to be non-parallel). The scattering volume is centered in the origin of the
coordinate system, and both the acoustic and electromagnetic waves are approxi-
mated as plane waves close to the origin. Thus, the electromagnetic and dielectric
perturbation fields near the origin are defined as

$$\boldsymbol{E}_\text{i}(\boldsymbol{r}',t) = \boldsymbol{E}_\text{i}(\boldsymbol{r}') = \boldsymbol{E}_\text{i0}\mathrm{e}^{\mathrm{i}\boldsymbol{k}\cdot\boldsymbol{r}'} \tag{A.8}$$

$$\varepsilon_1(\boldsymbol{r}',t) = \frac{\varepsilon_\text{r}^2\mathfrak{p}}{K}p_0\cos(\boldsymbol{q}\cdot\boldsymbol{r}' - \Omega t) \tag{A.9}$$

Here, $\boldsymbol{E}_\text{i0}$ is the complex field amplitude at the origin ($-\mathrm{i}\omega t$ time-dependence sep-
arated) and $\boldsymbol{k}$ is the electromagnetic wavevector. The scalar photoelastic relation
from equation (3.4) has been used, where $\mathfrak{p}$ is the photoelastic constant, p_0 is the
acoustic pressure amplitude at the origin, K is the bulk modulus, $\boldsymbol{q}$ is the acoustic
wavevector and Ω the acoustic frequency.

For simplicity, the electromagnetic polarization is assumed to be in z, $\boldsymbol{E}_\text{i0} \parallel \hat{\boldsymbol{z}}$.
This is also in part done to avoid polarization changes in the scattered field [26].
Due to this $\nabla(\boldsymbol{E}_\text{i} \cdot \nabla\varepsilon_1) = \boldsymbol{0}$ which simplifies the scattering integral to

$$\boldsymbol{E}_\text{sc}(\boldsymbol{r},t) = \frac{k^2}{4\pi\varepsilon_\text{r}} \int_{V_\text{sc}} \frac{\mathrm{e}^{\mathrm{i}k|\boldsymbol{r}-\boldsymbol{r}'|}}{|\boldsymbol{r}-\boldsymbol{r}'|} \left(\varepsilon_1(\boldsymbol{r}',t)\boldsymbol{E}_\text{i}(\boldsymbol{r}',t) + \boldsymbol{E}_\text{di}(\boldsymbol{r}',t)\right)\mathrm{d}v'$$

Since the incident electric field is time-independent, the term $\boldsymbol{E}_\text{di}$ can be simplified
to

$$\boldsymbol{E}_{di}(\boldsymbol{r}',t) = \frac{2\mathrm{i}\boldsymbol{E}_\text{i}(\boldsymbol{r}')}{\omega}\frac{\partial}{\partial t}\left(\varepsilon_1(\boldsymbol{r}',t)\right) - \frac{\boldsymbol{E}_\text{i}(\boldsymbol{r}')}{\omega^2}\frac{\partial^2}{\partial t^2}\left(\varepsilon_1(\boldsymbol{r}',t)\right)$$

Insertion of equation (A.8) and (A.9) gives

$$\boldsymbol{E}_{\text{sc}}(\boldsymbol{r}, t) = \frac{k^2}{4\pi\varepsilon_{\text{r}}} \int_{V_{\text{sc}}} \frac{\text{e}^{\text{i}k|\boldsymbol{r}-\boldsymbol{r}'|}}{|\boldsymbol{r} - \boldsymbol{r}'|} \boldsymbol{E}_{\text{i0}} \text{e}^{\text{i}\boldsymbol{k}\cdot\boldsymbol{r}'} \frac{\varepsilon_{\text{r}}^2 \mathfrak{p}}{K} p_0 f(\boldsymbol{r}', t) \text{d}v'$$

where

$$f(\boldsymbol{r}', t) = \cos(\boldsymbol{q} \cdot \boldsymbol{r}' - \Omega t) + \frac{2\text{i}\Omega}{\omega} \sin(\boldsymbol{q} \cdot \boldsymbol{r}' - \Omega t) + \frac{\Omega^2}{\omega^2} \cos(\boldsymbol{q} \cdot \boldsymbol{r}' - \Omega t)$$

Assuming far-field gives an approximation for the Green's function as [61]

$$\frac{\text{e}^{\text{i}k|\boldsymbol{r}-\boldsymbol{r}'|}}{|\boldsymbol{r} - \boldsymbol{r}'|} \approx \frac{\text{e}^{\text{i}kr}}{r} \text{e}^{-\text{i}k\hat{\boldsymbol{r}}\cdot\boldsymbol{r}'}$$

where $r = |\boldsymbol{r}|$ and $\hat{\boldsymbol{r}} = \boldsymbol{r}/r$. The scattering integral is now written as

$$\boldsymbol{E}_{\text{sc}}(\boldsymbol{r}, t) = \frac{\varepsilon_{\text{r}} k^2 \text{e}^{\text{i}kr} \boldsymbol{E}_{\text{i0}} \mathfrak{p} p_0}{4\pi r K} \int_{V_{\text{sc}}} \text{e}^{\text{i}k(\hat{\boldsymbol{k}}-\hat{\boldsymbol{r}})\cdot\boldsymbol{r}'} f(\boldsymbol{r}', t) \text{d}v'$$

The function $f(\boldsymbol{r}', t)$ can now be rewritten as complex exponentials giving

$$\begin{aligned}
f(\boldsymbol{r}', t) &= \frac{1}{2} \left(\text{e}^{\text{i}(\boldsymbol{q}\cdot\boldsymbol{r}'-\Omega t)} + \text{e}^{-\text{i}(\boldsymbol{q}\cdot\boldsymbol{r}'-\Omega t)} \right) + \frac{\Omega}{\omega} \left(\text{e}^{\text{i}(\boldsymbol{q}\cdot\boldsymbol{r}'-\Omega t)} - \text{e}^{-\text{i}(\boldsymbol{q}\cdot\boldsymbol{r}'-\Omega t)} \right) \\
&\quad + \frac{\Omega^2}{2\omega^2} \left(\text{e}^{\text{i}(\boldsymbol{q}\cdot\boldsymbol{r}'-\Omega t)} + \text{e}^{-\text{i}(\boldsymbol{q}\cdot\boldsymbol{r}'-\Omega t)} \right) \\
&= \text{e}^{\text{i}(\boldsymbol{q}\cdot\boldsymbol{r}'-\Omega t)} \frac{\omega^2 + 2\omega\Omega + \Omega^2}{2\omega^2} + \text{e}^{-\text{i}(\boldsymbol{q}\cdot\boldsymbol{r}'-\Omega t)} \frac{\omega^2 - 2\omega\Omega + \Omega^2}{2\omega^2} \\
&= \frac{1}{2} \left((1 + \Omega/\omega)^2 \, \text{e}^{\text{i}(\boldsymbol{q}\cdot\boldsymbol{r}'-\Omega t)} + (1 - \Omega/\omega)^2 \, \text{e}^{-\text{i}(\boldsymbol{q}\cdot\boldsymbol{r}'-\Omega t)} \right)
\end{aligned}$$

If it is assumed that $\Omega \ll \omega$, the scattered field can be written as

$$\begin{aligned}
\boldsymbol{E}_{\text{sc}}(\boldsymbol{r}, t) = {} & \frac{\varepsilon_{\text{r}} k^2 \text{e}^{\text{i}kr} \boldsymbol{E}_{\text{i0}} \mathfrak{p} p_0}{8\pi r K} \\
& \cdot \left(\text{e}^{-\text{i}\Omega t} \int_{V_{\text{sc}}} \text{e}^{\text{i}(k(\hat{\boldsymbol{k}}-\hat{\boldsymbol{r}})+\boldsymbol{q})\cdot\boldsymbol{r}'} \text{d}v' + \text{e}^{\text{i}\Omega t} \int_{V_{\text{sc}}} \text{e}^{\text{i}(k(\hat{\boldsymbol{k}}-\hat{\boldsymbol{r}})-\boldsymbol{q})\cdot\boldsymbol{r}'} \text{d}v' \right)
\end{aligned}$$

The two integrals are of the same form, $\int \text{e}^{\text{i}\boldsymbol{A}\cdot\boldsymbol{r}'} \text{d}v'$, where $\boldsymbol{A}$ is independent of $\boldsymbol{r}'$. This is solved in general below for the cuboid volume defined by $-L_m/2 \leq m \leq L_m/2$, $m = x, y, z$.

$$\begin{aligned}
\int_{V_{\text{sc}}} \text{e}^{\text{i}\boldsymbol{A}\cdot\boldsymbol{r}'} \text{d}v' &= \int_{V_{\text{sc}}} \text{e}^{\text{i}\boldsymbol{A}\cdot\hat{\boldsymbol{x}}x'} \text{e}^{\text{i}\boldsymbol{A}\cdot\hat{\boldsymbol{y}}y'} \text{e}^{\text{i}\boldsymbol{A}\cdot\hat{\boldsymbol{z}}z'} \text{d}v' \\
&= \prod_{m=x,y,z} \frac{1}{\text{i}\boldsymbol{A}\cdot\hat{\boldsymbol{m}}} \left(\text{e}^{\text{i}\boldsymbol{A}\cdot\hat{\boldsymbol{m}}L_m/2} - \text{e}^{-\text{i}\boldsymbol{A}\cdot\hat{\boldsymbol{m}}L_m/2} \right) \\
&= \prod_{m=x,y,z} \frac{2}{\boldsymbol{A}\cdot\hat{\boldsymbol{m}}} \sin\left(\boldsymbol{A}\cdot\hat{\boldsymbol{m}}\frac{L_m}{2} \right) = \prod_{m=x,y,z} L_m \text{sinc}\left(\frac{\boldsymbol{A}\cdot\hat{\boldsymbol{m}}L_m}{2\pi} \right)
\end{aligned}$$

where $\operatorname{sinc}(x) = \sin(\pi x)/(\pi x)$. To apply this result to $\boldsymbol{A} = k(\hat{\boldsymbol{k}} - \hat{\boldsymbol{r}}) \pm \boldsymbol{q}$ this is first simplified using the geometry defined earlier.

$$k(\hat{\boldsymbol{k}} - \hat{\boldsymbol{r}}) \pm \boldsymbol{q} = k\hat{\boldsymbol{x}} - k(\hat{\boldsymbol{x}}x + \hat{\boldsymbol{y}}y + \hat{\boldsymbol{z}}z)/r \pm q(\hat{\boldsymbol{x}}\cos\alpha + \hat{\boldsymbol{y}}\sin\alpha)$$

where r is not written out fully. $\boldsymbol{A} \cdot \hat{\boldsymbol{m}}$ are now calculated for the three coordinate axes as

$$\begin{aligned}
\boldsymbol{A} \cdot \hat{\boldsymbol{x}} &= k - kx/r \pm q\cos\alpha = k - k\sin\theta\cos\phi \pm q\cos\alpha \\
\boldsymbol{A} \cdot \hat{\boldsymbol{y}} &= -ky/r \pm q\sin\alpha = -k\sin\theta\sin\phi \pm q\sin\alpha \\
\boldsymbol{A} \cdot \hat{\boldsymbol{z}} &= -kz/r = -k\cos\theta
\end{aligned} \tag{A.10}$$

where a conversion to spherical coordinates was made. Insertion into the integral solution gives:

$$\begin{aligned}
\int_{V_{\mathrm{sc}}} &\mathrm{e}^{\mathrm{i}(k(\hat{\boldsymbol{k}} - \hat{\boldsymbol{r}}) \pm \boldsymbol{q}) \cdot \boldsymbol{r}'} \mathrm{d}v' \\
&= L_x \operatorname{sinc}\left(\frac{L_x}{2\pi}(k - k\sin\theta\cos\phi \pm q\cos\alpha) \right) \\
&\quad \cdot L_y \operatorname{sinc}\left(\frac{L_y}{2\pi}(-k\sin\theta\sin\phi \pm q\sin\alpha) \right) \cdot L_z \operatorname{sinc}\left(-\frac{L_z}{2\pi}k\cos\theta \right) \\
&= L_x L_y L_z \Phi^{\pm}(\theta, \phi)
\end{aligned} \tag{A.11}$$

where all angular dependence has been gathered in the function $\Phi^{\pm}(\theta, \phi)$. This result is now inserted into the scattered field, giving

$$\begin{aligned}
\boldsymbol{E}_{\mathrm{sc}}(\boldsymbol{r}, t) &= \frac{\varepsilon_{\mathrm{r}} k^2 \mathrm{e}^{\mathrm{i}kr} \boldsymbol{E}_{\mathrm{i}0} \mathfrak{p} p_0}{8\pi r K} L_x L_y L_z \left(\mathrm{e}^{-\mathrm{i}\Omega t} \Phi^+(\theta, \phi) + \mathrm{e}^{\mathrm{i}\Omega t} \Phi^-(\theta, \phi) \right) \\
&= \boldsymbol{E}_{\mathrm{i}0} E_{\mathrm{A}}(\boldsymbol{r}, t)
\end{aligned}$$

By inspecting $E_{\mathrm{A}}(\boldsymbol{r}, t)$ it is clear that two frequency-shifted components arise. Since the implied time-dependence is $\mathrm{e}^{-\mathrm{i}\omega t}$, the factors $e^{\mp\mathrm{i}\Omega t}$ give a frequency shift of $\pm\Omega$. The scattered field is written using two distinct components as

$$\boldsymbol{E}_{\mathrm{sc}}(\boldsymbol{r}, t) = \boldsymbol{E}_{\mathrm{sc}}^+(\boldsymbol{r}, t) + \boldsymbol{E}_{\mathrm{sc}}^-(\boldsymbol{r}, t) = \boldsymbol{E}_{\mathrm{i}0}\left(E_{\mathrm{A}}^+(\boldsymbol{r}, t) + E_{\mathrm{A}}^-(\boldsymbol{r}, t) \right)$$

where

$$E_{\mathrm{A}}^{\pm}(\boldsymbol{r}, t) = \frac{\varepsilon_{\mathrm{r}} k^2 \mathrm{e}^{\mathrm{i}kr} \mathfrak{p} p_0}{8\pi r K} L_x L_y L_z e^{\mp\mathrm{i}\Omega t} \Phi^{\pm}(\theta, \phi)$$

is a unitless function giving the dependence on range r and direction (θ, ϕ).

A.2.2 Solution in terms of power

This treatment has primarily been focused at the electric field. To obtain a more practical expression, this is now transformed into power. The power is calculated for the individual frequency shifted components, since they are distinct and single-frequency. The time average for one frequency component of the Poynting vector

is [61]

$$\left\langle \boldsymbol{S}_{\text{sc}}^{\pm} \right\rangle (\boldsymbol{r}) = \frac{1}{2} \text{Re} \left\{ \left(\boldsymbol{E}_{\text{sc}}^{\pm}(\boldsymbol{r},t) \text{e}^{-i\omega t} \right) \times \left(\boldsymbol{H}_{\text{sc}}^{\pm}(\boldsymbol{r},t) \text{e}^{-i\omega t} \right)^* \right\}$$
$$= \frac{1}{2} \text{Re} \left\{ \boldsymbol{E}_{\text{sc}}^{\pm}(\boldsymbol{r},t) \times \boldsymbol{H}_{\text{sc}}^{\pm}(\boldsymbol{r},t)^* \right\}$$

where the time-dependence of the incident electromagnetic wave was re-introduced. The magnetic field $\boldsymbol{H}_{\text{sc}}^{\pm}(\boldsymbol{r},t)$ is given by [61]

$$\boldsymbol{H}_{\text{sc}}^{\pm}(\boldsymbol{r},t) \approx \frac{1}{\text{i}k\eta_0\eta} \nabla \times \boldsymbol{E}_{\text{sc}}^{\pm}(\boldsymbol{r},t)$$

where η_0 is the wave impedance of free space and $\eta_0\eta$ the wave impedance in the material. An approximation has been made for k, where this is assumed to have the same value as before scattering. Since there is a frequency shift this is known to not be the case, but given a small acoustic frequency compared to the electromagnetic frequency, the error is small. The curl of $\boldsymbol{E}_{\text{sc}}^{\pm}(\boldsymbol{r},t)$ is now written as

$$\nabla \times \boldsymbol{E}_{\text{sc}}^{\pm}(\boldsymbol{r},t) = \nabla \times \left(\boldsymbol{E}_{\text{i0}} E_{\text{A}}^{\pm}(\boldsymbol{r},t) \right) = \nabla E_{\text{A}}^{\pm}(\boldsymbol{r},t) \times \boldsymbol{E}_{\text{i0}}$$

In spherical coordinates the gradient is written as [63]

$$\nabla f = \frac{\partial f}{\partial r} \hat{\boldsymbol{r}} + \frac{1}{r} \frac{\partial f}{\partial \theta} \hat{\boldsymbol{\theta}} + \frac{1}{r \sin \theta} \frac{\partial f}{\partial \phi} \hat{\boldsymbol{\phi}}$$

$E_{\text{A}}^{\pm}(\boldsymbol{r},t)$ contains a factor $1/r$, so the two last terms in the gradient will be $\sim 1/r^2$ and are neglected. The gradient is now written as

$$\nabla E_{\text{A}}^{\pm}(\boldsymbol{r},t) \approx \frac{\partial E_{\text{A}}}{\partial r} \hat{\boldsymbol{r}}$$
$$= \left(\frac{\text{i}k\text{e}^{\text{i}kr}}{r} - \frac{\text{e}^{\text{i}kr}}{r^2} \right) \frac{\varepsilon_{\text{r}} k^2 \mathfrak{p} p_0}{8\pi K} L_x L_y L_z \text{e}^{\mp\text{i}\Omega t} \Phi^{\pm}(\theta,\phi) \hat{\boldsymbol{r}}$$
$$\approx \text{i}k E_{\text{A}}^{\pm}(\boldsymbol{r},t) \hat{\boldsymbol{r}}$$

where the $1/r^2$ term was neglected. These results are inserted into the expression for the magnetic field, giving

$$\boldsymbol{H}_{\text{sc}}^{\pm}(\boldsymbol{r},t) = \frac{1}{\text{i}k\eta_0\eta} \left(\text{i}k E_{\text{A}}^{\pm}(\boldsymbol{r},t) \hat{\boldsymbol{r}} \times \boldsymbol{E}_{\text{i0}} \right) = \frac{E_{\text{A}}^{\pm}(\boldsymbol{r},t)}{\eta_0\eta} \hat{\boldsymbol{r}} \times \boldsymbol{E}_{\text{i0}}$$

Now, the cross product with the electric field is calculated as

$$\boldsymbol{E}_{\text{sc}}^{\pm}(\boldsymbol{r},t) \times \boldsymbol{H}_{\text{sc}}^{\pm}(\boldsymbol{r},t)^* = E_{\text{A}}^{\pm}(\boldsymbol{r},t) \boldsymbol{E}_{\text{i0}} \times \left(\frac{E_{\text{A}}^{\pm}(\boldsymbol{r},t)}{\eta_0\eta} \hat{\boldsymbol{r}} \times \boldsymbol{E}_{\text{i0}} \right)^*$$
$$= \frac{|E_{\text{A}}^{\pm}(\boldsymbol{r},t)|^2}{\eta_0\eta} \left(\hat{\boldsymbol{r}}(\boldsymbol{E}_{\text{i0}} \cdot \boldsymbol{E}_{\text{i0}}^*) - \boldsymbol{E}_{\text{i0}}^*(\boldsymbol{E}_{\text{i0}} \cdot \hat{\boldsymbol{r}}) \right)$$

If the wave propagates in $\hat{\boldsymbol{r}}$, $\boldsymbol{E}_{\text{sc}} \cdot \hat{\boldsymbol{r}} = 0$ and since $\boldsymbol{E}_{\text{sc}} \parallel \boldsymbol{E}_{\text{i0}}$ the cross product is simplified to

$$\boldsymbol{E}_{\text{sc}}^{\pm}(\boldsymbol{r},t) \times \boldsymbol{H}_{\text{sc}}^{\pm}(\boldsymbol{r},t)^* = \frac{\hat{\boldsymbol{r}}}{\eta_0\eta} |\boldsymbol{E}_{\text{i0}}|^2 |E_{\text{A}}^{\pm}(\boldsymbol{r},t)|^2$$

The time-averaged Poynting vector is now calculated as

$$\left\langle \boldsymbol{S}_{\text{sc}}^{\pm} \right\rangle (\boldsymbol{r}) = \frac{1}{2} \text{Re} \left\{ \boldsymbol{E}_{\text{sc}}^{\pm}(\boldsymbol{r},t) \times \boldsymbol{H}_{\text{sc}}^{\pm}(\boldsymbol{r},t)^{*} \right\} = \frac{\hat{\boldsymbol{r}}}{2\eta_0\eta} |\boldsymbol{E}_{\text{i0}}|^2 |E_{\text{A}}^{\pm}(\boldsymbol{r},t)|^2$$

where the time-dependence was removed by the absolute value. $|E_{\text{A}}^{\pm}(\boldsymbol{r},t)|^2$ is given by

$$|E_{\text{A}}^{\pm}(\boldsymbol{r},t)|^2 = \frac{\varepsilon_{\text{r}}^2 k^4 \mathfrak{p}^2 p_0^2}{64\pi^2 r^2 K^2} L_x^2 L_y^2 L_z^2 \Phi^{\pm}(\theta,\phi)^2$$

To find an expression for $|\boldsymbol{E}_{\text{i0}}|^2$, the field from the transmitter antenna is written as (adapted from [57])

$$\boldsymbol{E}_{\text{T}}(\boldsymbol{r}) = \mathrm{i}k\eta_0\eta \frac{\mathrm{e}^{\mathrm{i}kr}}{4\pi r} \boldsymbol{F}_{\perp}(\hat{\boldsymbol{r}})$$

where $\boldsymbol{F}_{\perp}$ is the far-field amplitude. Now the coordinate system is not the same as earlier in the derivation! Here it is a spherical coordinate system with origin at the transmitting antenna. This corresponds to a translation in $-\hat{\boldsymbol{x}}$ of the original coordinate system. Let R_{T} be the distance between the two coordinate systems, or equivalently the distance from the transmitter to the scattering center. The direction to the scattering center in this new system is denoted $\hat{\boldsymbol{r}}_{sc} = \boldsymbol{r}_{sc}/R_{\text{T}}$. Assuming that the orientations of the transmitter and scattering coordinate systems are the same, $|\boldsymbol{E}_{\text{i0}}|^2$ can be written in the transmitter system as [57]

$$|\boldsymbol{E}_{\text{i0}}|^2 = |\boldsymbol{E}_{\text{T}}(\boldsymbol{r}_{sc})|^2 = \left| \mathrm{i}k\eta_0\eta \frac{\mathrm{e}^{\mathrm{i}kR_{\text{T}}}}{4\pi R_{\text{T}}} \boldsymbol{F}_{\perp}(\hat{\boldsymbol{r}}_{sc}) \right|^2 = \frac{k^2\eta_0^2\eta^2}{16\pi^2 R_{\text{T}}^2} |\boldsymbol{F}_{\perp}(\hat{\boldsymbol{r}}_{sc})|^2 = 2\eta_0\eta \mathcal{P}(\hat{\boldsymbol{r}}_{sc})$$

If the maximum gain G_{T} of the antenna is in the direction $\hat{r}_{sc}$, it holds that [57]

$$\mathcal{P}(\hat{\boldsymbol{r}}_{sc}) = \frac{P_{\text{T}} G_{\text{T}}}{4\pi R_{\text{T}}^2}$$

where P_{T} is the power accepted by the antenna. This is used to write

$$|\boldsymbol{E}_{\text{i0}}|^2 = 2\eta_0\eta \frac{P_{\text{T}} G_{\text{T}}}{4\pi R_{\text{T}}^2}$$

Now this is inserted into the time-average of the power density

$$\left\langle \boldsymbol{S}_{\text{sc}}^{\pm} \right\rangle (\boldsymbol{r}) = \hat{\boldsymbol{r}} \frac{P_{\text{T}} G_{\text{T}}}{4\pi R_{\text{T}}^2} \frac{\varepsilon_{\text{r}}^2 k^4 \mathfrak{p}^2 p_0^2}{64\pi^2 r^2 K^2} L_x^2 L_y^2 L_z^2 \Phi^{\pm}(\theta,\phi)^2$$

Now the effects of the receiving antenna are considered. It is assumed that this antenna is optimally directed towards the scattering center. The received power is then

$$P_{\text{R}}^{\pm} = \left| \left\langle \boldsymbol{S}_{\text{sc}}^{\pm} \right\rangle (R_{\text{R}},\theta,\phi) \right| A_{\text{e}}$$

where R_{R} is the distance between the scattering center and the receiver, and the receiver is located in the direction (θ,ϕ) as seen from the scattering center [57]. A_{e} is the effective area of the antenna, which can be rewritten as

$$A_{\text{e}} = \frac{\lambda_{\text{R}}^2 G_{\text{R}}}{4\pi}$$

where G_R is the gain of the receiving antenna [57]. λ_R should be the wavelength at the antenna here, which is not necessarily the same as in the material. Combining this with earlier results gives a received power of

$$P_R^\pm = \frac{\lambda_R^2 G_R}{4\pi} \frac{P_T G_T}{4\pi R_T^2} \frac{\varepsilon_r^2 k^4 \mathfrak{p}^2 p_0^2}{64\pi^2 R_R^2 K^2} L_x^2 L_y^2 L_z^2 \Phi^\pm(\theta,\phi)^2$$

For a more traditional bistatic radar equation [54] this can be written as

$$P_R^\pm = \frac{P_T G_T G_R \lambda_R^2 \sigma^\pm(\theta,\phi)}{(4\pi)^3 R_T^2 R_R^2}$$

with the radar cross-section given by

$$\sigma^\pm(\theta,\phi) = \frac{\varepsilon_r^2 k^4 \mathfrak{p}^2 p_0^2}{16\pi K^2} L_x^2 L_y^2 L_z^2 \Phi^\pm(\theta,\phi)^2$$

A.2.3 Signal-to-noise ratio and coherent integration

An important quantity besides received power is signal-to-noise ratio (SNR). For this, the average noise power is described as [64]

$$P_n = k_B T B$$

where k_B is Boltzmann's constant, T is the temperature and B is the utilized receiver bandwidth. The noise power picked up by the antenna is calculated using the standard temperature $T_0 = 290$ K. The SNR directly at the antenna can thus be written as

$$SNR_{ant}^\pm \frac{P_T G_T G_R \lambda_R^2 \sigma^\pm(\theta,\phi)}{(4\pi)^3 R_T^2 R_R^2 k_B T_0 B}$$

After the antenna is the RF front-end which usually contains a bandpass filter, low-noise amplifier (LNA), and mixer. Here the received signal is amplified so that it can be further processed. The amplification affects both the signal and noise, but the electronic components add more noise which causes the SNR to deteriorate. To quantify this, the concept of noise ratio and noise figure is used. The noise ratio is defined as [64]

$$F = \frac{SNR_i}{SNR_o}$$

where the SNR's are in linear units, i denotes input and o denotes output. It is more common to use the noise figure, which is simply the noise ratio expressed in dB units, $NF = 10 \log_{10}(F)$. After the RF front-end the signal is often strong enough to not be affected by further noise, so it is usually sufficient to use a noise ratio/figure for that part of the receiver. The SNR after the receiver can now be written using the noise ratio as

$$SNR^\pm = \frac{P_T G_T G_R \lambda_R^2 \sigma^\pm(\theta,\phi)}{(4\pi)^3 R_T^2 R_R^2 k_B T_0 B \cdot F}$$

One more effect is added to this, and that is signal integration in the signal processing following the receiver. Noise can often be modeled as a random process, and if multiple samples are added together the noise can be averaged out. If coherent demodulation is used, N samples added together will cause the SNR to improve by a factor N [54]. The SNR can then be written as

$$SNR_N^\pm = \frac{P_T G_T G_R \lambda_R^2 \sigma^\pm(\theta, \phi)}{(4\pi)^3 R_T^2 R_R^2 k_B T_0 BF} N$$

which is our final form of the SNR estimate.

A.2.4   Refined interaction region

The derivation in A.2.1 is based on plane waves and a very simple geometry. A problem with the geometry used is that there is no easy way to obtain the parameters L_x, L_y and L_z from common parameters of the acoustic and electromagnetic beams. To address this, a slightly different interaction geometry based on beams is introduced as shown in figure A.2. Here the beam diameters d_e and d_a have been introduced for the electromagnetic and acoustic plane waves. For simplicity, it is assumed that the beam edges are infinitely sharp, i.e. inside the wave behaves as a plane wave and outside it is zero. This way the previous derivation can be used with the exception of the interaction region. Since plane waves are still used the model is not based on real beams. However, for real beams it is still easy to obtain widths at the overlap area and then the interaction region should be fairly close using this model.

The integration limits corresponding to this parallelogram can be written as

$$x_0 - x_1 < x < x_0 + x_1$$
$$-d_e/2 < y < d_e/2$$
$$-L_z/2 < z < L_z/2$$

where

$$x_0 = \frac{y}{\tan \alpha}$$
$$x_1 = \frac{d_a}{2 \sin \alpha}$$

The solution to the integral for a general function on the form $\mathrm{e}^{\mathrm{i}\boldsymbol{A}\cdot\boldsymbol{r}}$ is now written as

$$\begin{aligned}
I &= \int_{V_{sc}} \mathrm{e}^{\mathrm{i}\boldsymbol{A}\cdot\boldsymbol{r}'} \mathrm{d}v' \\
&= \int_{-L_z/2}^{L_z/2} \mathrm{e}^{\mathrm{i}\boldsymbol{A}\cdot\hat{\boldsymbol{z}}z'} \mathrm{d}z' \int_{-d_e/2}^{d_e/2} \left(\mathrm{e}^{\mathrm{i}\boldsymbol{A}\cdot\hat{\boldsymbol{y}}y'} \int_{x_0-x_1}^{x_0+x_1} \mathrm{e}^{\mathrm{i}\boldsymbol{A}\cdot\hat{\boldsymbol{x}}x'} \mathrm{d}x' \right) \mathrm{d}y' \\
&= \int_{-L_z/2}^{L_z/2} \mathrm{e}^{\mathrm{i}\boldsymbol{A}\cdot\hat{\boldsymbol{z}}z'} \mathrm{d}z' \cdot I_2
\end{aligned}$$
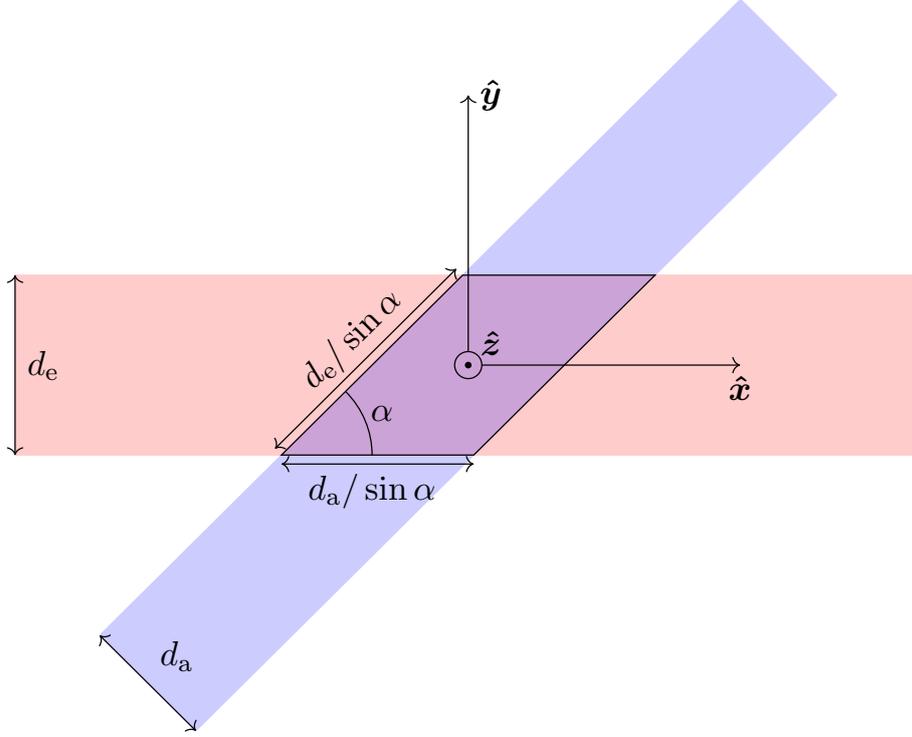
Figure A.2: Parallelogram interaction region

using the solution to the integral from A.2.1, this integral can be written as

$$I = L_z \text{sinc}\left(\frac{\boldsymbol{A} \cdot \hat{\boldsymbol{z}} L_z}{2\pi}\right) \cdot I_2$$

The integral I_2 can be solved as

$$
\begin{aligned}
I_2 &= \int_{-d_e/2}^{d_e/2} e^{i\boldsymbol{A}\cdot\hat{\boldsymbol{y}}y'} \cdot \frac{1}{i\boldsymbol{A}\cdot\hat{\boldsymbol{x}}}\left(e^{i\boldsymbol{A}\cdot\hat{\boldsymbol{x}}(x_0+x_1)} - e^{i\boldsymbol{A}\cdot\hat{\boldsymbol{x}}(x_0-x_1)}\right)\mathrm{d}y' \\
&= \int_{-d_e/2}^{d_e/2} e^{i\boldsymbol{A}\cdot\hat{\boldsymbol{y}}y'} \cdot e^{i\boldsymbol{A}\cdot\hat{\boldsymbol{x}}x_0}\frac{2}{\boldsymbol{A}\cdot\hat{\boldsymbol{x}}}\sin(\boldsymbol{A}\cdot\hat{\boldsymbol{x}}x_1)\mathrm{d}y' \\
&= \int_{-d_e/2}^{d_e/2} e^{i\boldsymbol{A}\cdot(\hat{\boldsymbol{y}}y'+\hat{\boldsymbol{x}}x_0)} \cdot 2x_1\text{sinc}\left(\frac{\boldsymbol{A}\cdot\hat{\boldsymbol{x}}x_1}{\pi}\right)\mathrm{d}y' \\
&= \frac{d_a}{\sin\alpha}\text{sinc}\left(\frac{\boldsymbol{A}\cdot\hat{\boldsymbol{x}}d_a}{2\pi\sin\alpha}\right)\int_{-d_e/2}^{d_e/2} e^{i\boldsymbol{A}\cdot(\hat{\boldsymbol{y}}+\hat{\boldsymbol{x}}/\tan\alpha)y'}\mathrm{d}y' \\
&= \frac{d_a}{\sin\alpha}\text{sinc}\left(\frac{\boldsymbol{A}\cdot\hat{\boldsymbol{x}}d_a}{2\pi\sin\alpha}\right) \cdot I_3
\end{aligned}
$$

The integral I_3 can be solved analogously to the solution from A.2 as

$$I_3 = d_\text{e}\text{sinc}\left(\frac{\boldsymbol{A}\cdot(\hat{\boldsymbol{y}}+\hat{\boldsymbol{x}}/\tan\alpha)d_\text{e}}{2\pi}\right)$$

Now the complete solution to I is written as

$$\begin{aligned}I =&\frac{d_\text{a}}{\sin\alpha}\text{sinc}\left(\frac{\boldsymbol{A}\cdot\hat{\boldsymbol{x}}d_\text{a}}{2\pi\sin\alpha}\right)\cdot d_\text{e}\text{sinc}\left(\frac{\boldsymbol{A}\cdot(\hat{\boldsymbol{y}}+\hat{\boldsymbol{x}}/\tan\alpha)d_\text{e}}{2\pi}\right)\\&\cdot L_z\text{sinc}\left(\frac{\boldsymbol{A}\cdot\hat{\boldsymbol{z}}L_z}{2\pi}\right)\end{aligned}$$

If the specific function of interest to the scattering problem is inserted, and spherical coordinates are used as in equation (A.10) the solution is

$$\begin{aligned}\int_{V_\text{sc}}&\text{e}^{\text{i}(k(\hat{\boldsymbol{k}}-\hat{\boldsymbol{r}})\pm\boldsymbol{q})\cdot\boldsymbol{r}'}\text{d}v'\\=&\frac{d_\text{a}d_\text{e}L_z}{\sin\alpha}\text{sinc}\left(\frac{d_\text{a}}{2\pi\sin\alpha}(k-k\sin\theta\cos\phi\pm q\cos\alpha)\right)\\&\cdot\text{sinc}\left(\frac{d_\text{e}}{2\pi\tan\alpha}(k-k\sin\theta(\cos\phi+\sin\phi\tan\alpha)\pm q(\cos\alpha+\sin\alpha\tan\alpha))\right)\\&\cdot\text{sinc}\left(-\frac{L_z}{2\pi}k\cos\theta\right)\\=&\frac{d_\text{a}d_\text{e}L_z}{\sin\alpha}\Phi_\text{p}^\pm(\theta,\phi)\end{aligned}$$

where the function $\Phi_\text{p}^\pm(\theta,\phi)$ was introduced similarly to $\Phi^\pm(\theta,\phi)$ in equation (A.11). In contrast to the derivation in A.2, $\Phi_\text{p}^\pm(\theta,\phi)$ does not contain all angular dependence since there is still a factor $1/\sin\alpha$ not included. This is due to that factor being directly related to the interaction volume. If the area of the parallelogram is calculated and multiplied by the width in z, the result is

$$\frac{d_\text{a}d_\text{e}L_z}{\sin\alpha}$$

This means that the solution of the integral is the interaction volume multiplied by $\Phi_\text{p}^\pm(\theta,\phi)$. This is the same result as in equation (A.11).

For the major results of the derivations in section A.2, the interaction region is easily changed from cuboid to beam-based. The geometry only matters in the calculation of the integral, so the only necessary changes are from there. This means that the interaction volume needs to be changed from $L_xL_yL_z$ to $d_\text{a}d_\text{e}L_z/\sin\alpha$ and the function $\Phi^\pm$ changed to $\Phi_\text{p}^\pm$. With this in mind, the results from section A.2.1-A.2.3 are rewritten using these changes. First, the scattered power is written as

$$\boldsymbol{E}_\text{sc,p}(\boldsymbol{r},t)=\boldsymbol{E}_\text{i0}\left(E_\text{A,p}^+(\boldsymbol{r},t)+E_\text{A,p}^-(\boldsymbol{r},t)\right)$$

where

$$E_\text{A,p}^\pm(\boldsymbol{r},t)=\frac{\varepsilon_\text{r}k^2\text{e}^{\text{i}kr}\mathfrak{p}p_0}{8\pi rK}\frac{d_\text{a}d_\text{e}L_z}{\sin\alpha}e^{\mp\text{i}\Omega t}\Phi_\text{p}^\pm(\theta,\phi)$$

The radar equations are unchanged if a new radar cross-section is used, written as

$$\sigma_{\mathrm{p}}^{\pm}(\theta, \phi) = \frac{\varepsilon_{\mathrm{r}}^2 k^4 \mathfrak{p}^2 p_0^2}{16\pi K^2} \frac{d_{\mathrm{a}}^2 d_{\mathrm{e}}^2 L_z^2}{\sin^2 \alpha} \Phi_{\mathrm{p}}^{\pm}(\theta, \phi)^2$$

As stated before, these equations are quite similar to those from the cuboid geometry.

A.2.5   2D derivations

The derivations leading to the radar equation in appendix A.1 and A.2.1-A.2.2 are based on the assumption of three dimensional space. While this is reasonable for modeling reality, simulations are often done in two dimensions for computational speed and simplicity. If the analytical model is to be compared with 2D simulation results, a 2D analytical model is necessary. The first thing to identify in order to achieve this goal is where the first assumption of 3D space is done. This is in the solution of the inhomogeneous Helmholtz equation, so that is where this 2D derivation must start. The equation is written as (see appendix A.1.2)

$$\nabla^2 \boldsymbol{E}_{\mathrm{sc}} + k^2 \boldsymbol{E}_{\mathrm{sc}} = -k^2 \frac{\varepsilon_1}{\varepsilon_{\mathrm{r}}} \boldsymbol{E}_{\mathrm{i}} - \frac{1}{\varepsilon_{\mathrm{r}}} \nabla(\boldsymbol{E}_{\mathrm{i}} \cdot \nabla \varepsilon_1) - \frac{k^2}{\varepsilon_{\mathrm{r}}} \boldsymbol{E}_{\mathrm{di}}$$

This has a similar solution in 2D as in 3D, but with a different Green's function. The solution to this in two dimensions, and under a Sommerfeld radiation condition is instead [61, 62]

$$\begin{aligned}
\boldsymbol{E}_{\mathrm{sc,2D}}(\boldsymbol{r}, t) = &\frac{1}{\varepsilon_{\mathrm{r}}} \int_{S_{\mathrm{sc}}} \frac{\mathrm{i}}{4} H_0^{(1)}(k|\boldsymbol{r} - \boldsymbol{r}'|) \\
&\cdot \left(k^2 \varepsilon_1(\boldsymbol{r}', t) \boldsymbol{E}_{\mathrm{i}}(\boldsymbol{r}', t) + \nabla\left(\boldsymbol{E}_{\mathrm{i}}(\boldsymbol{r}', t) \cdot \nabla \varepsilon_1(\boldsymbol{r}', t)\right) + k^2 \boldsymbol{E}_{\mathrm{di}}(\boldsymbol{r}', t) \right) \mathrm{d}s'
\end{aligned}$$

where $H_0^{(1)}$ is a Hankel function and

$$\begin{aligned}
\boldsymbol{E}_{\mathrm{di}}(\boldsymbol{r}', t) = &\frac{2\mathrm{i}\varepsilon_{\mathrm{r}}}{\omega} \frac{\partial}{\partial t}\left(\boldsymbol{E}_{\mathrm{i}}(\boldsymbol{r}', t)\right) + \frac{2\mathrm{i}}{\omega} \frac{\partial}{\partial t}\left(\varepsilon_1(\boldsymbol{r}', t) \boldsymbol{E}_{\mathrm{i}}(\boldsymbol{r}', t)\right) \\
&- \frac{\varepsilon_{\mathrm{r}}}{\omega^2} \frac{\partial^2}{\partial t^2}\left(\boldsymbol{E}_{\mathrm{i}}(\boldsymbol{r}', t)\right) - \frac{1}{\omega^2} \frac{\partial^2}{\partial t^2}\left(\varepsilon_1(\boldsymbol{r}', t) \boldsymbol{E}_{\mathrm{i}}(\boldsymbol{r}', t)\right)
\end{aligned}$$

The same geometry as in A.2.1 can now be used to calculate the scattered field (see figure A.1). The change is that the interaction region is now limited to the xy-plane, as are coordinates for the observation point. The incident fields are defined as in equations (A.8) and (A.9), but with the coordinates $\boldsymbol{r}'$ being 2D, i.e. $\boldsymbol{r}' = x'\hat{\boldsymbol{x}} + y'\hat{\boldsymbol{y}}$. The polarization of the incident electric field, however, is still in z regardless of the 2D geometry otherwise used. This can be done since it is not dependent on the coordinate z, only the unit vector $\hat{\boldsymbol{z}}$. Insertion of the incident fields now gives

$$\boldsymbol{E}_{\mathrm{sc,2D}}(\boldsymbol{r}, t) = \frac{k^2}{\varepsilon_{\mathrm{r}}} \int_{S_{\mathrm{sc}}} \frac{\mathrm{i}}{4} H_0^{(1)}(k|\boldsymbol{r} - \boldsymbol{r}'|) \boldsymbol{E}_{\mathrm{i}0} \mathrm{e}^{\mathrm{i}\boldsymbol{k}\cdot\boldsymbol{r}'} \frac{\varepsilon_{\mathrm{r}}^2 \mathfrak{p}}{K} p_0 f(\boldsymbol{r}', t) \mathrm{d}s'$$

where

$$f(\boldsymbol{r}', t) = \cos(\boldsymbol{q} \cdot \boldsymbol{r}' - \Omega t) + \frac{2\mathrm{i}\Omega}{\omega} \sin(\boldsymbol{q} \cdot \boldsymbol{r}' - \Omega t) + \frac{\Omega^2}{\omega^2} \cos(\boldsymbol{q} \cdot \boldsymbol{r}' - \Omega t)$$

Assumption of far-field can be used to approximate the Hankel function. This is done by adapting the method for the 3D Green's function in [61] while using the approximation from (9.2.3), p.364 in [65].

$$\frac{\mathrm{i}}{4} H_0^{(1)}(k|\boldsymbol{r} - \boldsymbol{r}'|) \approx \frac{\mathrm{e}^{\mathrm{i}(kr+\pi/4)}}{\sqrt{8\pi kr}} \mathrm{e}^{-\mathrm{i}k\hat{\boldsymbol{r}}\cdot\boldsymbol{r}'}$$

which is inserted in the integral, giving

$$\boldsymbol{E}_{\mathrm{sc,2D}}(\boldsymbol{r}, t) = \frac{\varepsilon_{\mathrm{r}} k^2 \mathrm{e}^{\mathrm{i}(kr+\pi/4)} \boldsymbol{E}_{\mathrm{i0}} \mathfrak{p} p_0}{K\sqrt{8\pi kr}} \int_{S_{\mathrm{sc}}} \mathrm{e}^{\mathrm{i}k(\hat{\boldsymbol{k}}-\hat{\boldsymbol{r}})\cdot\boldsymbol{r}'} f(\boldsymbol{r}', t) \mathrm{d}s'$$

Inspection of this equation shows that it is the same integral as the one solved in section A.2.1, but in 2D instead of 3D. All other differences are in the factor in front of the integral. If it is assumed that $\Omega \ll \omega$, the scattered field can be written as

$$\boldsymbol{E}_{\mathrm{sc,2D}}(\boldsymbol{r}, t) = \boldsymbol{E}_{\mathrm{i0}} \left(E_{\mathrm{A,2D}}^+(\boldsymbol{r}, t) + E_{\mathrm{A,2D}}^-(\boldsymbol{r}, t) \right)$$

where

$$E_{\mathrm{A,2D}}^{\pm}(\boldsymbol{r}, t) = \frac{\varepsilon_{\mathrm{r}} k^2 \mathrm{e}^{\mathrm{i}(kr+\pi/4)} \mathfrak{p} p_0}{K\sqrt{8\pi kr}} L_x L_y \mathrm{e}^{\mp\mathrm{i}\Omega t} \Phi_{\mathrm{2D}}^{\pm}(\theta, \phi)$$

and

$$\Phi_{\mathrm{2D}}^{\pm}(\theta, \phi) = \mathrm{sinc}\left(\frac{L_x}{2\pi}(k - k\cos\phi \pm q\cos\alpha) \right) \mathrm{sinc}\left(\frac{L_y}{2\pi}(-k\sin\phi \pm q\sin\alpha) \right)$$

Since the integral was calculated in 2D instead of 3D this time, the L_z factor was removed as well as one of the sinc functions in Φ. The argument of the sinc functions was also slightly altered since $\sin\theta = 1$ in the xy-plane. Calculation of the Poynting vector is unaffected by the change from 3D to 2D, with an exception being the change in $E_A^{\pm}$. The time-average of the Poynting vector is then written as

$$\left\langle \boldsymbol{S}_{\mathrm{sc,2D}}^{\pm} \right\rangle (\boldsymbol{r}) = \frac{\hat{\boldsymbol{r}}}{2\eta_0\eta} |\boldsymbol{E}_{\mathrm{i0}}|^2 |E_{\mathrm{A,2D}}^{\pm}(\boldsymbol{r}, t)|^2$$

where the time-dependence was removed by the absolute value. $|E_{\mathrm{A,2D}}^{\pm}(\boldsymbol{r}, t)|^2$ is given by

$$|E_{\mathrm{A,2D}}^{\pm}(\boldsymbol{r}, t)|^2 = \frac{\varepsilon_{\mathrm{r}}^2 k^3 \mathfrak{p}^2 p_0^2}{8\pi r K^2} L_x^2 L_y^2 \Phi_{\mathrm{2D}}^{\pm}(\theta, \phi)^2$$

The parallelogram geometry introduced in section A.2.4 can be used in 2D to refine the interaction region. As discussed in section A.2.4, using this geometry only affects the interaction region factors and the Φ function. The scattered field using this interaction region is then written as

$$\boldsymbol{E}_{\mathrm{sc,2D,p}}(\boldsymbol{r}, t) = \boldsymbol{E}_{\mathrm{i0}} \left(E_{\mathrm{A,2D,p}}^+(\boldsymbol{r}, t) + E_{\mathrm{A,2D,p}}^-(\boldsymbol{r}, t) \right)$$

where
$$E^\pm_{\mathrm{A,2D,p}}(\boldsymbol{r}, t) = \frac{\varepsilon_{\mathrm{r}} k^2 \mathrm{e}^{\mathrm{i}(kr + \pi/4)} \mathfrak{p} p_0}{K\sqrt{8\pi kr}} \frac{d_{\mathrm{a}} d_{\mathrm{e}}}{\sin\alpha} e^{\mp\mathrm{i}\Omega t} \Phi^\pm_{\mathrm{2D,p}}(\theta, \phi)$$

and
$$\Phi^\pm_{\mathrm{2D,p}}(\theta, \phi) = \mathrm{sinc}\left(\frac{d_{\mathrm{a}}}{2\pi\sin\alpha}(k - k\cos\phi \pm q\cos\alpha)\right)$$
$$\cdot\mathrm{sinc}\left(\frac{d_{\mathrm{e}}}{2\pi\tan\alpha}(k - k(\cos\phi + \sin\phi\tan\alpha) \pm q(\cos\alpha + \sin\alpha\tan\alpha))\right)$$

The Poynting vector is also written as
$$\left\langle \boldsymbol{S}^\pm_{\mathrm{sc,2D,p}}\right\rangle(\boldsymbol{r}) = \frac{\hat{\boldsymbol{r}}}{2\eta_0\eta}|\boldsymbol{E}_{\mathrm{i0}}|^2 |E^\pm_{\mathrm{A,2D,p}}(\boldsymbol{r}, t)|^2$$

where the time-dependence was removed by the absolute value. $|E^\pm_{\mathrm{A,2D,p}}(\boldsymbol{r}, t)|^2$ is given by
$$|E^\pm_{\mathrm{A,2D,p}}(\boldsymbol{r}, t)|^2 = \frac{\varepsilon_{\mathrm{r}}^2 k^3 \mathfrak{p}^2 p_0^2}{8\pi r K^2} \frac{d_{\mathrm{a}}^2 d_{\mathrm{e}}^2}{\sin^2\alpha} \Phi^\pm_{\mathrm{2D}}(\theta, \phi)^2$$

The equations above are used for comparison with 2D simulations.

A.3   Geometry for maximum scattering

Let us begin with the Φ angular dependence function:
$$\Phi^\pm(\theta, \phi) = \mathrm{sinc}\left(\frac{L_x}{2\pi}\left(k - k\sin\theta\cos\phi \pm q\cos\alpha\right)\right)$$
$$\cdot\mathrm{sinc}\left(\frac{L_y}{2\pi}\left(-k\sin\theta\sin\phi \pm q\sin\alpha\right)\right)$$
$$\cdot\mathrm{sinc}\left(-\frac{L_z}{2\pi}k\cos\theta\right)$$

The maximum of this function must be where all sinc-functions are maximum. For a sinc the maximum is given when the argument is equal to 0, which simplifies the process. Firstly, consider the third sinc:
$$\mathrm{sinc}\left(-\frac{L_z}{2\pi}k\cos\theta\right)$$

The argument of this is obviously zero when $\cos\theta = 0$, which for $0 \leq \theta \leq \pi$ is when $\theta = \pi/2$. This fixes the maximum to the plane formed by the incident electromagnetic and acoustic wavevectors. What it means is that the scattering occurs primarily in one single interaction plane, which simplifies analysis. Now the arguments of the two other sinc functions are set to zero with the value for θ being set to $\pi/2$:

$$k - k\cos\phi \pm q\cos\alpha = 0 \tag{A.12}$$
$$-k\sin\phi \pm q\sin\alpha = 0 \tag{A.13}$$

This relates the propagation direction ϕ of the scattered wave to the angle α and the wavenumbers k and q.

A.3.1   Condition for α

The system (A.12),(A.13) is now used to find the angle between wavevectors giving a maximum. To avoid confusion, the positive and negative versions of the system are considered separately.

$(+)$ case

Begin with equation (A.12):

$$\cos\alpha = \frac{k}{q}\left(\cos\phi - 1\right) = \frac{k}{q}\left(\pm\sqrt{1 - \sin^2\phi} - 1\right)$$

Now equation (A.13) is inserted in the above as

$$\cos\alpha = \frac{k}{q}\left(\pm\sqrt{1 - \frac{q^2}{k^2}\sin^2\alpha} - 1\right)$$

This is rewritten as

$$\pm\sqrt{k^2 - q^2\sin^2\alpha} = q\cos\alpha + k$$

Squaring the equation implies

$$k^2 - q^2\sin^2\alpha = q^2\cos^2\alpha + 2kq\cos\alpha + k^2$$

After some simplification, the following equation is obtained:

$$\cos\alpha = -\frac{q}{2k} \tag{A.14}$$

Since q and k are non-negative it is clear that $\pi/2 \le \alpha \le \pi$.

$(-)$ case

This case is the same as the $(+)$ case, but with some sign changes. Begin with equation (A.12):

$$\cos\alpha = \frac{k}{q}\left(1 - \cos\phi\right) = \frac{k}{q}\left(1 \pm \sqrt{1 - \sin^2\phi}\right)$$

Now equation (A.13) is inserted in the above as

$$\cos\alpha = \frac{k}{q}\left(1 \pm \sqrt{1 - \frac{q^2}{k^2}\sin^2\alpha}\right)$$

This is rewritten as

$$\pm\sqrt{k^2 - q^2\sin^2\alpha} = q\cos\alpha - k$$

Squaring the equation implies

$$k^2 - q^2\sin^2\alpha = q^2\cos^2\alpha - 2kq\cos\alpha + k^2$$

After some simplification, the following equation is obtained:

$$\cos\alpha = \frac{q}{2k} \tag{A.15}$$

Since q and k are non-negative it is clear that $0 \le \alpha \le \pi/2$.

A.3.2   Condition for ϕ

If either of equations (A.14) or (A.15) is inserted in the system (A.12), (A.13) the following is obtained:

$$\cos\phi = 1 - 2\cos^2\alpha = -\cos 2\alpha$$
$$\sin\phi = -2\sin\alpha\cos\alpha = -\sin 2\alpha$$

These can be written as

$$\phi = \begin{cases} \arccos(-\cos 2\alpha) + 2\pi n & = \pi - 2\alpha + 2\pi n \\ 2\pi - \arccos(-\cos 2\alpha) + 2\pi n & = \pi + 2\alpha + 2\pi n \end{cases}$$

$$\phi = \begin{cases} \arcsin(-\sin 2\alpha) + 2\pi n & = -2\alpha + 2\pi n \\ \pi - \arcsin(-\sin 2\alpha) + 2\pi n & = \pi + 2\alpha + 2\pi n \end{cases}$$

Where n is an integer. From these equations it is clear that $\phi = \pi + 2\alpha + 2\pi n$ is the only valid solution. If ϕ is constrained by $0 \leq \phi \leq 2\pi$ and α is constrained by $\pi/2 < \alpha < \pi$ (+) or $0 < \alpha < \pi/2$ (−), ϕ can be written as

$$\phi = -\pi + 2\alpha \ (+ \text{ case})$$
$$\phi = \pi + 2\alpha \ (- \text{ case})$$

These two equations give the propagation direction of the scattered wave for (+) or (−) scattering.

A.3.3   Summary

The equations for both the (+) and (−) case are very similar, and can be written in a simple way using $\pm$ signs. The conditions define the geometry which gives the maximum scattering through the angle α between EM and acoustic incident waves and the angles θ and ϕ for the receiver direction. They are summarized below:

$$\theta = \pi/2 \tag{A.16}$$
$$\cos\alpha = \mp\frac{q}{2k} = \mp\frac{\lambda}{2\Lambda} \tag{A.17}$$
$$\phi = \mp\pi + 2\alpha \tag{A.18}$$

In acousto-optics the interaction occurs in a single plane, which is what (A.16) describes. There is also a Bragg condition defining the angle between an acoustic and optic wave which is required for maximum reflection. This is presented in [25] as

$$\sin\theta_B = \frac{\lambda}{2\Lambda}$$

The relationship between the angles in acousto-optics and those used in this model are shown in figure A.3 with $\phi_i = \phi_r = \theta_B$ [25]. From the figure it is clear that $\alpha = \pi/2 \pm \theta_B$. In this model (A.17) is used to obtain the optimal angle between

electromagnetic and acoustic waves, and the transformation between α and θ_B can be inserted as

$$\cos\alpha = \cos(\pi/2 \pm \theta_B) = \mp\sin\theta_B$$

The RHS of (A.17) is $\mp\lambda/2\Lambda$. This should be equal to the RHS above, which directly gives the Bragg condition.

In acousto-optics it is assumed that the reflection angle equals the incidence angle. This is not directly stated here, but can be obtained by changing from the angles α, ϕ to the incidence angle ϕ_i and reflection angle ϕ_r shown in figure A.3. It is clear from the figure that

$$\phi_i = \pm(\alpha - \pi/2)$$

$$\phi_r = \begin{cases} \phi - \phi_i & (+ \text{ case}) \\ 2\pi - \phi - \phi_i & (- \text{ case}) \end{cases}$$

Now the condition for ϕ_i and (A.18) are inserted in the condition for ϕ_r, giving

$$\phi_r = \begin{cases} -\pi + 2\alpha - (\alpha - \pi/2) = \alpha - \pi/2 = \phi_i & (+ \text{ case}) \\ 2\pi - (\pi + 2\alpha) + (\alpha - \pi/2) = \pi/2 - \alpha = \phi_i & (- \text{ case}) \end{cases}$$

and thus, the equation for α is also in agreement with acousto-optics. So, from simple variable substitutions the same results as in acousto-optics are obtained. This gives the model some validation since it is in agreement with an already established theory.


(a) $+$ case   **(b)** $-$ case
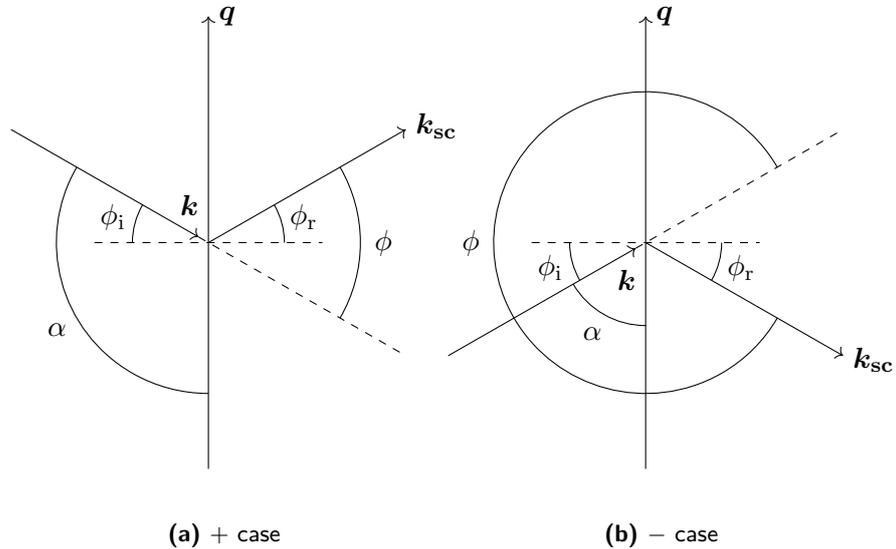
Figure A.3: Comparison of angles used in this model and angles of incidence and reflection. Both for the $+$ and $-$ cases.

A.3.4 Refined interaction region

For the refined interaction region described in section A.2.4 the derivation for
finding a maximum scattering geometry is different than above. However, a first
hypothesis would be that the resulting condition would be the same. To test this,
the angles described by equations (A.16), (A.17), (A.18) are inserted in $\Phi_{\mathrm{p}}^{\pm}(\theta, \phi)$
from section A.2.4. The function can be written as

$$
\begin{aligned}
\Phi_{\mathrm{p}}^{\pm}(\theta, \phi) = {} & \mathrm{sinc}\left(\frac{d_{\mathrm{a}}}{2\pi \sin \alpha}(k - k \sin \theta \cos \phi \pm q \cos \alpha) \right) \\
& \cdot \mathrm{sinc}\left(\frac{d_{\mathrm{e}}}{2\pi \tan \alpha}(k - k \sin \theta(\cos \phi + \sin \phi \tan \alpha) \pm q(\cos \alpha + \sin \alpha \tan \alpha)) \right) \\
& \cdot \mathrm{sinc}\left(-\frac{L_z}{2\pi}k \cos \theta \right)
\end{aligned}
$$

As for the function used in derivations for the cuboid geometry, the maximum
value of this function is 1. This happens only when the arguments of all sinc's are
0. Due to this fact, the problem is simplified by only considering the parts of the
arguments required to be zero, namely

$$
\left\{
\begin{array}{lr}
k - k \sin \theta \cos \phi \pm q \cos \alpha & \text{(A.19)} \\
k - k \sin \theta(\cos \phi + \sin \phi \tan \alpha) \pm q(\cos \alpha + \sin \alpha \tan \alpha) & \text{(A.20)} \\
-\dfrac{L_z}{2\pi}k \cos \theta & \text{(A.21)}
\end{array}
\right.
$$

Now the equations (A.16), (A.17), (A.18) are inserted. In the derivations the
following relations are well used

$$
\begin{aligned}
\cos(\mp \pi + 2\alpha) &= \sin^2 \alpha - \cos^2 \alpha \\
\sin(\mp \pi + 2\alpha) &= -2 \sin \alpha \cos \alpha \\
q &= \mp 2k \cos \alpha
\end{aligned}
$$

Argument (A.19) is now written as

$$
\begin{aligned}
k - k \sin(\pi/2) \cos(\mp \pi + 2\alpha) \pm q \cos \alpha &= k \left(1 - (\sin^2 \alpha - \cos^2 \alpha) \pm (\mp 2 \cos^2 \alpha) \right) \\
&= k \left(1 - \sin^2 \alpha - \cos^2 \alpha \right) = 0
\end{aligned}
$$

Since it is equal to zero, the first sinc is maximized. Now argument (A.20) is
written as

$$
\begin{aligned}
k - k \sin(\pi/2)&(\cos(\mp \pi + 2\alpha) + \sin(\mp \pi + 2\alpha) \tan \alpha) \pm q(\cos \alpha + \sin \alpha \tan \alpha \\
&= k \left(1 - (\sin^2 \alpha - \cos^2 \alpha - 2 \sin \alpha \cos \alpha \tan \alpha) \pm (\mp 2 \cos \alpha)(\cos \alpha + \sin \alpha \tan \alpha) \right) \\
&= k \left(1 - \sin^2 \alpha + \cos^2 \alpha + 2 \sin^2 \alpha - 2 \cos^2 \alpha - 2 \sin^2 \alpha \right) \\
&= k \left(1 - \sin^2 \alpha - \cos^2 \alpha \right) = 0
\end{aligned}
$$

Since it is equal to zero, the second sinc is maximized. Finally, argument (A.21)
is written as

$$
-\frac{L_z}{2\pi}k \cos \pi/2 = 0
$$

Since it is equal to zero, the third sinc is also maximized. Thus, all sinc functions are maximized which maximizes $\Phi_{\mathrm{p}}^{\pm}$. This shows that the same condition (equations (A.16), (A.17), (A.18)) maximizes the Φ function for both the simple cuboid geometry and the refined geometry based on beams.

One difference is that there is a factor $1/\sin\alpha$ in the parallelogram interaction region while the cuboid interaction region is constant. This should affect the angle α giving maximum scattering in the parallelogram case. To find a maximum of this and not just the function Φ would require other derivations than those done for maximizing three sinc functions. Since this was not done, this factor should be kept in mind when discussing Bragg matching. One thing which can be noted though is how the factor might change the peak scattering qualitatively. The square of the factor $1/\sin^2\alpha$ is what matters for the scattered power. This has a minimum at $\alpha = \pi/2$ and increases as α tends towards 0 or π. What this means for the total scattering is that the decrease in scattering when moving away from the α given by equation (A.17) can be slightly counteracted. In the $(-)$ case, $0 < \alpha < \pi/2$, so $1/\sin^2\alpha$ is larger at smaller angles than the one given by equation (A.17). Due to this, the maximum scattering can be shifted to a smaller angle α. Similarly, in the $(+)$ case, $\pi/2 < \alpha < \pi$, so $1/\sin^2\alpha$ is larger at larger angles than from equation (A.17). Maximum scattering can then be shifted to a larger α. The size of the shift in α depends on how fast Φ decreases when the angle α tends away from that in equation (A.17). The function Φ is comprised of sinc functions, and the main factor determining this is the width of the main lobe of the sinc's. This is determined from the argument of the functions, which in turn depend on the geometry of the problem. Once again, the derivation is not done but it is noted that the exact geometry can have an effect on how large the shift in α is when compared to the Bragg maximum from equation (A.17).

LUND
UNIVERSITY